Towards Optical Simulation of Topological Phenomena with Ring Resonators

by

Bharat Kuchhal

A thesis
presented to the University of Waterloo
in fulfillment of the
thesis requirement for the degree of
Master of Science
in
Physics (Quantum Information)

Waterloo, Ontario, Canada, 2025

© Bharat Kuchhal 2025

Author's Declaration

I hereby declare that I am the sole author of this thesis. This is a true copy of the thesis, including any required final revisions, as accepted by my examiners.

I understand that my thesis may be made electronically available to the public.

Abstract

In recent years, there has been a growing interest in synthetic dimensions. Unlike physical dimensions where one is restricted with three possible dimensions, one can tailor a lattice system with several higher order dimensions even with a lower-order physical system. In this thesis, we will explore, both theoretically and experimentally, how equidistant frequency modes in a resonator—specifically a ring resonator—can be used as a synthetic dimension. In this respect, we will first explore basics of resonators by reviewing a Fabry-Perot resonator and developing a coupled-mode theory to understand its transmission and reflection spectrum. We will then expand and develop a coupled-mode theory for the case of a ring resonator, and explore experimental results for a basic fiber-beam splitter based ring resonator. Next, we will modify the ring resonator with a few off the shelf fiber optic components like a Dense Division Wavelength Multiplexing filter, a fiber electro-optic modulator, and an optical amplifier, and see how they transform the transmission characteristics. Lastly, we will modulate the ring resonator at the same frequency as the free-spectral range of the resonator to couple the modes to observe a band structure in the reciprocal space, much like atoms in a periodic solid-state crystal coupled via Coulomb interactions lead to energy bands in the conjugate momentum space. For this purpose, we will develop a coupled-mode theory for a ring resonator modulated by a phase modulator, look at some theoretical results for symmetric and asymmetric band structures, and observe some experimental results for the symmetric case. Thus, we highlight the potential of fiber-ring resonators as versatile platforms for optical simulation of topological systems. Further, the ability to replicate higher-dimensional phenomena using frequency modes opens new pathways for investigating exotic physical behaviors, such as non-Hermitian systems and synthetic magnetic fields, in compact and experimentally accessible setups.

Acknowledgements

I would like to begin by expressing my deepest gratitude to my supervisors, Professor Christopher Wilson and Professor Kevin Resch, for offering me the wonderful opportunity to work on an optical simulation platform—an area I had long aspired to explore. In selecting a research project, students often face a choice between experimental or theoretical work; I was fortunate to be entrusted with a project that combined both. This opportunity, requiring both a broad perspective and deep expertise, was possible only through the guidance of Prof. Wilson and Prof. Resch.

I am equally grateful to my group members. Working with two research groups, each with distinct areas of expertise, greatly enriched my learning experience. I would like to especially thank Jamal and Zheng, who were not only colleagues and friends but also mentors. Jamal guided me through experimental work, while Zheng introduced me to coding and its applications to theory. I am also thankful to Andrew Cameron, whose encouragement to exercise provided a welcome outlet during challenging moments in the lab. Special thanks are due to all members of the Engineered Quantum Systems Laboratory—Cindy, Ben, Andy, Dima, Ibrahim, Guang, Mohd. Soltani, and Amir—and the Quantum Optics and Quantum Information group—Tristan, Kaleb, and Jonah—for their insightful discussions and for creating a supportive and enjoyable research environment. I would also like to thank Dr. Avik Dutt (University of Maryland) and Dr. Alen Senanian (Cornell University) for their helpful suggestions.

Beyond the university, I am deeply appreciative of the friendships that sustained me. I am grateful to Barry, Stewart, Andrew Hopper, Nikhil, Daryl, Andre, and Frank, from whom I have gained invaluable life lessons. I remain forever indebted to my family for their unwavering care and support, especially since I moved abroad in 2018. I also extend my thanks to my friends from India and the United States—Debadri, Lin, Rudrev, Ishaa, Varun, Chanpreet, and Rahul—for their continued encouragement. Finally, I am especially grateful to my close friend Vijay, whose steadfast support was instrumental during the writing of this thesis.

Dedication

To my family.

Table of Contents

Author's Declaration ii

Abstract iii

Acknowledgements iv

Dedication v

List of Figures viii

1 Introduction 1

1.1 Overview . . . 2

1.2 Fabry-Perot Resonators . . . 4

1.2.1 Resonator Modes . . . 4

1.2.2 Cavity Transmission and Reflectance . . . 6

1.3 Coupled-Mode theory . . . 10

2 All Fiber-Optic Ring Resonators 19

2.1 Overview . . . 19

2.2 Theory . . . 20

2.2.1 All-Pass Ring Resonator . . . 20

2.2.2 Add-drop Ring Resonator . . . 26

2.3 Experimental Results 28
2.3.1 Cavity Resonance 28
2.3.2 Drift Calculation 31
2.4 Modified Ring Resonator 34

3 Optical Simulation with a Fiber-Ring Resonator **38**
3.1 Overview 38
3.2 Band Structure Measurements 39
3.2.1 Theory 40
3.2.2 Experimental Results 62
3.3 Future Work 68

4 Conclusions **70**

References **73**

List of Figures

1.1 A Fabry-Perot cavity with 2 mirrors M_1 and M_2 with reflectances r_1 and r_2 and transmittances t_1 and t_2, respectively. The mirrors are a length L apart and contain a medium of refractive index n. E_0, E_R, and E_T are the electric fields of the incident, reflected, and transmitted electromagnetic waves. . . 5

1.2 Steady-State Transmission spectrum for a Fabry-Perot Cavity for $\mathcal{R} = 0.1, 0.4, 0.7$ and 1.0 7

1.3 Steady-State Reflection spectrum for a Fabry-Perot Cavity for $\mathcal{R} = 0.1, 0.4, 0.7$ and 1.0 8

1.4 A diagram depicting a cavity connected to n waveguides. The cavity modes have time-dependent amplitudes $a_m(t)$ and the waveguide modes with fields going into and out of the cavity are depicted as s_n^+ and s_n^-, respectively. . . 11

1.5 In the language of CMT, the Fabry-Perot cavity (containing a medium with refractive index n) can be analyzed as a single-mode cavity with mode amplitude $a(t)$ connected to two waveguide ports with ingoing field amplitudes s_1^+ and s_2^+ and outgoing field amplitudes s_1^- and s_2^-. The fields leak into and out of the cavity via the two waveguides with lifetimes τ_1 and τ_2. . . . 14

1.6 Steady-State Transmission $T(\omega)$ and Reflection $R(\omega)$ spectrum for a Fabry-Perot Cavity with cavity-waveguide external quality factors $Q_1 = Q_2 = 1000$ showing a resonance when the cavity detuning $\Delta\omega = \omega_0$. Note, for these simulations we normalized T and R by ω_0. 17

2.1 (a) All-Pass Ring Resonator; (b) Add-Drop Ring Resonator; BS: Beam-Splitter, R: Radius of Ring 21

2.2 (a) Transmission Spectrum $T_t(\varphi)$ and (b) Phases $\Phi(\varphi)$ for an all-pass ring resonator with $\alpha = 0.95$, and Finesse values 10, 20, 30, 40, 50, and 60 . . . 23

2.3 Transmission characteristics via through port (T_t) and drop port (T_d) for an add-drop ring resonator with $\alpha = 0.95$, and 2 cases—$r_1 = r_2 = 0.95$ and $r_1 = r_2 = 0.995$. 28

2.4 A single ring resonance for an add-drop ring made with just 99:1 beam-splitters. 30

2.5 Thermal Drift for rising edge of the ramp with slopes 0.00111 ($0.6V_{\text{pp}}$), 0.00153 ($0.8V_{\text{pp}}$), and 0.00351 ($1.0V_{\text{pp}}$), and drifts 1.11 MHz/s, 1.53 MHz/s, 3.51 MHz/s, respectively. 32

2.6 Thermal Drift for falling edge of the ramp with slopes 0.00118 ($0.6V_{\text{pp}}$), 0.00159 ($0.8V_{\text{pp}}$), and 0.00358 ($1.0V_{\text{pp}}$), and drifts 1.18 MHz/s, 1.59 MHz/s, 3.58 MHz/s, respectively. 33

2.7 A single ring resonance for an add-drop ring made with just 99:1 beam-splitters and a DWDM filter. 34

2.8 A single (a) noisy ring resonance and (b) averaged ring resonance for an add-drop ring made with just 99:1 beam-splitters, a DWDM filter, and an electro-optic modulator. 35

2.9 (a) Multiple ring resonances with the complete ring. The red curve is the ramp and the blue curve are the ring resonances under the falling edge of the ramp. The resonances were observed in High Resolution Acquisition Mode on the oscilloscope, and they are drifted from each other at frequencies $\nu_1 = 19.39$ MHz, $\nu_2 = 19.46$ MHz, $\nu_3 = 17.43$ MHz, and $\nu_4 = 16.99$ MHz. (b) The drifted ring resonances follow a quadratic dependence. 37

3.1 (a) A ring resonator dynamically modulated by an electro-optic modulator. (b) Different modes of the resonator coupled to each other. V_{EOM}: Modulation voltage, ω_c: Fundamental cavity mode, ω_0: Free spectral range, J: Nearest neighbor coupling constant 40

3.2 A simple ring resonator with an electro-optic modulator of width $2w$. . . . 41

3.3 (a) Band structure resulting from a $V_0 = 10$V modulation, (b) Expected scope trace representing a 1D photonic density of states. To obtain the scope trace, we can integrate (or sum) over every eigenvalue $\Delta\omega$ in the band structure trace in (a). Note, this simulation was performed in collaboration with Dr. Zheng Shi. 54

3.4 (a) Band structure resulting from a $V_0 = 10$V modulation when sliced off at a $\nu_{\text{FSR}} = 17.1$ MHz (b) Expected scope trace. Note, this simulation was performed in collaboration with Dr. Zheng Shi. 55

3.5 (a) Band structure resulting from a $V_0 = 10$V modulation when sliced off at a $\nu_{\text{FSR}} = 17.62$ MHz (b) Expected scope trace. Note, this simulation was performed in collaboration with Dr. Zheng Shi. 56

3.6 (a) Band structure for a $V_0 = 13$V modulation (b) Expected scope trace. Note, this simulation was performed in collaboration with Dr. Zheng Shi. . 58

3.7 (a) Band structure for $V_1 = 0$V, $V_2 = 10$V, $n = 2$, $\sigma = 0$; (b) Expected scope trace. Note, this simulation was performed in collaboration with Dr. Zheng Shi. 59

3.8 (a) Band structure for $V_1 = 10$V, $V_2 = 8$V, $n = 2$, $\sigma = \pi/2$; (b) Expected scope trace. Note, this simulation was performed in collaboration with Dr. Zheng Shi. 60

3.9 (a) Band structure for $V_1 = 10$V, $V_2 = 30$V, $n = 3$, $\sigma = 0$; (b) Expected scope trace. Note, this simulation was performed in collaboration with Dr. Zheng Shi. 61

3.10 Experimental setup for a modified ring resonator to determine the band structure in a synthetic dimension 63

3.11 Experimental Setup: 1. Rio Orion 1542 nm laser, 2. Tektronix AFG1062 – 2 channel, 3. Thorlabs 2x2 99:1 couplers, 4. Thorlabs 5 GHz InGaAs PDs, 5. Thorlabs paddle polarization controller, 6. Thorlabs 26 dB gain Booster Optical Amplifier + Temperature Controller, 7. Fiberdyne 100 GHz, 1550 nm DWDM filter, 8. Optilab 10 GHz, 1550 nm electro-optic phase modulator, 9. Keysight 8 GHz, 20 GSa/s oscilloscope, 10. SRS DC – 350 MHz amplifier 64

3.12 (a) Scope Trace, (b) Averaged scope trace indicating regions R_1, R_2, and R_3, (c) Regions R_1, R_2, and R_3 in (b) have been magnified to show a single peak, doublets, and no peaks as a result of phase modulation. 65

3.13 Band Structure obtained by changing the 1D averaged scope trace in Figure 3.12(b) to a 2D plot. 67

3.14 Resulting band structures when the one-dimensional scope trace in Figure 3.12(b) is converted to a two-dimensional image plots using different free-spectral ranges (a) $\nu_{\text{FSR}} = 17.1$ MHz (b) $\nu_{\text{FSR}} = 17.7$ MHz 68

Chapter 1

Introduction

Resonators/Cavities have found a wide variety of applications in quantum computation and information in the past century. One of the most important inventions of the 20^{th} century was the laser, a powerful coherent source of light. The most commonly used laser today resembles a simple Fabry-Perot optical resonator with a gain medium between two partially reflecting and partially transmitting mirrors kept at a fixed distance from each other[1]. After exciting the cavity from one of the mirrors, light bounces back and forth between the mirrors such that it gets amplified by the gain medium between consecutive reflections. The output of this device is then seen via the second mirror as a small amount of light leaks out. Given the fixed separation of the mirrors, the resonator can output a highly coherent signal with a very narrow linewidth.

Very recently, cavities have found wide applications in quantum computing. One of the earlier experiments on Cavity Quantum Electrodynamics (Cavity QED) performed by S. Haroche and J.M. Raimond involved coupling Rydberg atoms to a millimeter-wave Fabry-Perot cavity with inter-mirror separation of $\sim$ 1cm [2]. The idea of cavity QED was extended to circuit QED where superconducting qubits can be coupled to microwave superconducting coplanar waveguide resonators[3]. The superconducting qubit is an artificial atom which can either be a charge or flux or a phase qubit. Quantum Dots coupled to defects in photonic crystal cavities serve as another prominent example where artificial atoms have been coupled to resonators for applications in quantum information[4]. Other examples include incorporating a mechanical SiN membrane at the node or anti-node of SiO_2/Ta_2O_5 multilayer Fabry-Perot cavity[5], development of a spoke-anchored toroidal optomechanical microresonator where optical whispering gallery modes were coupled to mechanical breathing modes[6], and SiN based nanomechanical oscillators coupled to optical modes of toroidal silica microcavities to study quantum optomechanics[7], quantum

sensing and metrology by transferring quantum states between optical cavities and mechanical oscillations.

Resonators can also be used to develop quantum simulators. Quantum simulators consist of building blocks (like qubits) which follow quantum mechanical laws that can mimic an intractable quantum system by tailoring the interactions between individual building blocks[8]. As an example, a system of three ion traps have been used to simulate a frustrated Ising spin model[9][10]. Another example involves developing a Bose-Hubbard lattice of superconducting circuits to simulate a Mott insulator[11] and simulating dissipative phase transitions in a system consisting of a superconducting qubit coupled to 72 microwave cavities[12].

A subset of quantum simulation is optical (or photonic) simulation where photons are used to simulate physical phenomena by mediating interactions between them[13]. In recent years, ring resonators modulated by phase modulators have been used to study energy band structures in momentum space by coupling consecutive frequency modes[14]. They have also been used to study the energy bands of synthetic Hall ladders by combining the frequency modes with clockwise and counter-clockwise modes of doubly connected rings. The clockwise and counter-clockwise modes mimic a pseudo-spin degree of freedom[15]. Another application includes simultaneously amplitude and phase modulating the ring to implement non-Hermitian lattice Hamiltonians and study nontrivial energy band windings[16]. In this endeavor, we focused on developing a ring resonator platform to study certain topological phenomena in synthetic frequency dimensions and attempted to replicate results from *Nat Commun* **10**, 3122 (2019) [14].

1.1 Overview

In this thesis, we will explore specifically a ring resonator and study both theoretically and experimentally how it can be used to explore topological phenomena in synthetic dimensions. To do so, we will first look at the basics of resonators in Chapter 1 by exploring the Fabry-Perot cavity in detail. A Fabry-Perot resonator serves as a basis for resonators used everywhere in microwave and optical engineering, spectroscopy, telecommunications, and, as we discussed earlier, the invention of the laser and possible applications in quantum information. Specifically, we will first look at the transmission and reflection characteristics of a Fabry-Perot cavity and observe how we see transmission maximas (or reflection minimas) whenever we excite a resonator with a source which can be frequency detuned about its central wavelength. We will then derive the same transmission and reflection

spectrum using a powerful tool called coupled-mode theory. A Fabry-Perot cavity can often be viewed as a single cavity connected to two waveguides for either excitation or cavity readout. But coupled-mode theory generalizes this notion to multiple cavities with multiple modes connected to multiple waveguides. The power of coupled-mode theory relies on the fact that the equations of motion governing the cavity and waveguide modes are basic algebraic and first-order differential equations which can easily be solved. For this and later purpose, coupled-mode theory will be derived in its full generality with Fabry-Perot cavity serving as a basic example.

In Chapter 2, we will then extend our analysis to the case of a ring-resonator. Specifically, we will first look at some basic beam-splitter relations for an all-pass ring-resonator, develop a coupled-mode theory for it, and extend the results for a more general add-drop ring resonator. Once we theoretically derive the transmission and reflection characteristics of an add-drop ring resonator, we will then look at some experimental results for a fiber-optic ring resonator. We will first explore how to develop a simple fiber-optic ring and look at the transmission through its drop port. We will then modify the ring and add basic components like a Dense-Wavelength Division Multiplexing filter and an Electro-Optic Phase Modulator, and study how the addition of every component changes the transmission spectrum. We will also see why adding a Booster Optical Amplifier is necessary.

In Chapter 3, we will study how a fiber-optic ring resonator modulated by an electro-optic modulator can be used to simulate a band structure in time by exciting the RF port with a sinusoid of the same frequency as the free-spectral range to couple the neighboring modes of the resonator. More specifically, we will provide a sinusoid modulation of the form $V_{\text{EOM}}(t) = V_0 \cos \omega_0 t$ in an attempt to replicate results from *Nat Commun* **10**, 3122 (2019) [14]. We will first theoretically develop a coupled-mode theory for a ring-resonator containing a phase modulator, transform the equations of motion and recognize that if we modulate the cavity at a frequency equal to the free-spectral range of the resonator (ω_0), we end up coupling the modes of the cavity, and this leads to a sinusoidal band structure in time as we detune the cavity. The cavity detuning turns out to be energy eigenvalues of the Floquet Hamiltonian. We will also theoretically see that we can get asymmetric bands by modulating the cavity with $V_{\text{EOM}}(t) = V_1 \cos \omega_0 t + V_2 \cos(n\omega_0 t + \sigma)$. We will then end our discussion by looking at some of the experimental results for the former case where we excite the cavity with a single sinusoid, and formulate a method to observe a single band structure with some signal analysis techniques.

1.2 Fabry-Perot Resonators

1.2.1 Resonator Modes

We start our analysis with the study of Fabry-Perot resonators. A simple Fabry-Perot cavity consists of two partially reflecting, partially transmitting planar mirrors facing each other[1][17]. Partial transmittance allows light to enter and leave the cavity, partial reflectance allows light to be contained inside. This setup is akin to a string fixed at both ends. When such a string is driven from one end, the string vibrates strongly–known as resonance–at certain discrete normal mode frequencies exhibiting a standing-wave pattern. If the string has a length L, the normal mode wavelengths λ can be found using

$$2L = m\lambda, \quad \forall\ m \in \mathbb{N} \tag{1.1}$$

Further, if the velocity of the wave on the string is v, the normal mode frequencies will be related to the wavelengths as

$$f = v/\lambda \tag{1.2}$$

Thus, the string can oscillate at normal mode frequencies

$$\begin{aligned} f_1 &= v/2L, \\ f_2 &= v/L, \\ f_3 &= 3v/2L, \cdots \end{aligned} \tag{1.3}$$

In a similar fashion, one can analyze a Fabry-Perot cavity excited on one end by a laser. We start our analysis by considering two lossless plane mirrors facing each other with partial reflectances r_1 and r_2, and partial transmittances t_1 and t_2 as shown in Figure 1.1[1][17]. These coefficients follow Fresnel's law, i.e., $|r_i|^2 + |t_i|^2 = 1$ for $i = 1, 2$. To understand the resonator modes in detail, we first consider the transverse component of the electric field of a monochromatic wave of angular frequency ω with the form

$$\vec{E}(\vec{r}, t) = Re[\vec{E}(\vec{r})e^{i\omega t}] \tag{1.4}$$

Since we are considering time-harmonic fields, we will implicitly presume the $e^{i\omega t}$ dependence from now on and only consider the more important spatial dependence for our purposes. The complex amplitude of the transverse component $E(\vec{r})$ is a solution of the Helmholtz equation $\nabla^2 E + k^2 E = 0$. Here $k = \omega/v$ is the wavenumber and v is the speed

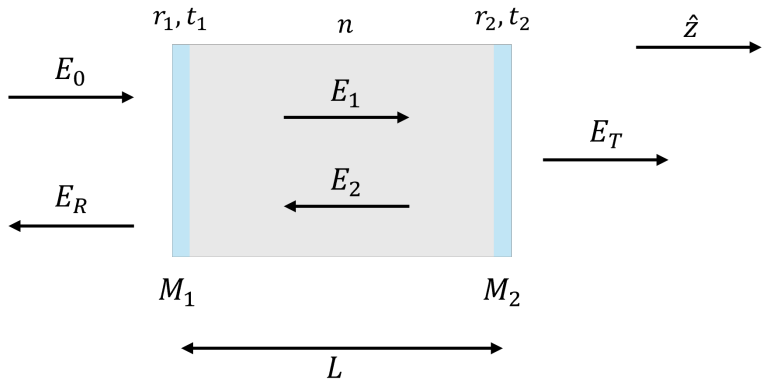


Figure 1.1: A Fabry-Perot cavity with 2 mirrors M_1 and M_2 with reflectances r_1 and r_2 and transmittances t_1 and t_2, respectively. The mirrors are a length L apart and contain a medium of refractive index n. E_0, E_R, and E_T are the electric fields of the incident, reflected, and transmitted electromagnetic waves.

of light in the medium within the planar mirrors. Further, if c is the speed of light in vacuum, $v = c/n_g$, where n_g is the group refractive index of the medium. The standing wave solution to the Helmholtz equation is

$$\vec{E}(\vec{r}) = \hat{z} E_0 \sin kz \tag{1.5}$$

Here, E_0 is a constant. At the boundaries $z = 0$ and $z = L$, we expect the transverse component to vanish leading to discrete resonator modes satisfying $k_m = m\pi/n_g L$, $\forall$ $m \in \mathbb{N}$ which is same as Eq.(1.1) with wavenumbers $k_m = 2\pi n_g/\lambda_m$. Further, since all the k_m's are potential solutions to the Helmholtz equation, the complete solution will be the superposition

$$\vec{E}(\vec{r}) = \hat{z} \sum_m E_m \sin k_m z, \tag{1.6}$$

where E_m's are constants. Notice, for $m = 0$, $E_0 \sin k_0 z = 0$ as $k_0 = 0$. Thus, $m = 0$ represents a resonator mode with zero energy. Further, we only consider $m > 0$ since negative values of m do not constitute independent resonator modes as $\sin k_{-m} z = -\sin k_m z$.

Just as in Eq. (1.2), we can now define resonator mode frequencies as

$$\nu_m = \frac{c k_m}{2\pi} = m \frac{v}{2L}, \quad \forall\ m \in \mathbb{N} \tag{1.7}$$

We now notice a peculiar feature. If we take the difference of consecutive resonator modes as in

$$\nu_{FSR} = (m+1)\frac{v}{2L} - m\frac{v}{2L} = \frac{v}{2L} \tag{1.8}$$

we realize the resonator modes are equally spaced by a constant value $\nu_{FSR} = v/2L$. This constant value is called the Free-Spectral Range (FSR) and is an important feature of any resonator. Note, the FSR is only dependent on the physical dimensions and refractive index of the medium.

1.2.2 Cavity Transmission and Reflectance

Notice in Eq. (1.5), the plane wave propagates with a phase $\varphi = kz$. This is crucial. We start, as in Figure 1.1, with a plane wave with amplitude E_0 and frequency ω incident on a partially transmitting mirror. Mirror M_1 will partially reflect and partially transmit this incident wave based on basic beam-splitter relations

$$E_R = -r_1 E_0 + i t_1 E_2 \tag{1.9a}$$

$$\text{and} \quad E_1 = i t_1 E_0 - r_1 E_2 \tag{1.9b}$$

Here r_1 and t_1 are (real) amplitude reflection and transmission coefficients of mirror M_1 satisfying $r_1^2 + t_1^2 = 1$ such that $r_1, t_1 < 1$. Further, mirror M_2 is kept at a distance L from M_1. Thus, the transmitted wave it_1E_0 will travel a distance L before being reflected and transmitted by M_2 picking up a phase $e^{-i\varphi/2}$ where $\varphi(\omega) = k(2L) = 2L(\omega n/c)$, and n is the refractive index of the medium inside the resonator. We will also assume that the field inside the resonator attenuates by a factor α between consecutive reflections. Mirror M_2 will now reflect a portion $-r_2(it_1)\alpha e^{-i\varphi/2}E_0$ of the the field back into the cavity. It will now travel back to M_1 picking up another phase $e^{-i\varphi/2}$ and getting attenuated again by α in the process. M_1 will again reflect a portion $(-r_1)\alpha e^{-i\varphi/2}(-r_2)(it_1)\alpha e^{-i\varphi/2}E_0 = r_1 r_2 \alpha^2 e^{-i\varphi} i t_1 E_0$ back into the cavity. The wave inside the cavity will go an infinite number of such cycles and each cycle multiplies the amplitude of the field by $r_1 r_2 \alpha^2 e^{-i\varphi}$. Thus, the total field inside the cavity will be

$$\begin{aligned} E_1 &= it_1E_0 + r_1r_2\alpha^2 e^{-i\varphi} i t_1 E_0 + (r_1r_2\alpha^2 e^{-i\varphi})^2 i t_1 E_0 + ... \\ &= it_1E_0[1 + r_1r_2\alpha^2 e^{-i\varphi} + (r_1r_2\alpha^2 e^{-i\varphi})^2 + ...] \\ &= \frac{it_1}{1 - r_1r_2\alpha^2 e^{-i\varphi}} E_0 \end{aligned} \tag{1.10}$$

where we have used the fact that $r_1, r_2, \alpha < 1$ to calculate the infinite sum. Substituting Eq. (1.10) in Eq. (1.9b) now gives us

$$E_2 = -\frac{it_1 r_2 \alpha^2 e^{-i\varphi}}{1 - r_1 r_2 \alpha^2 e^{-i\varphi}} E_0 \tag{1.11}$$

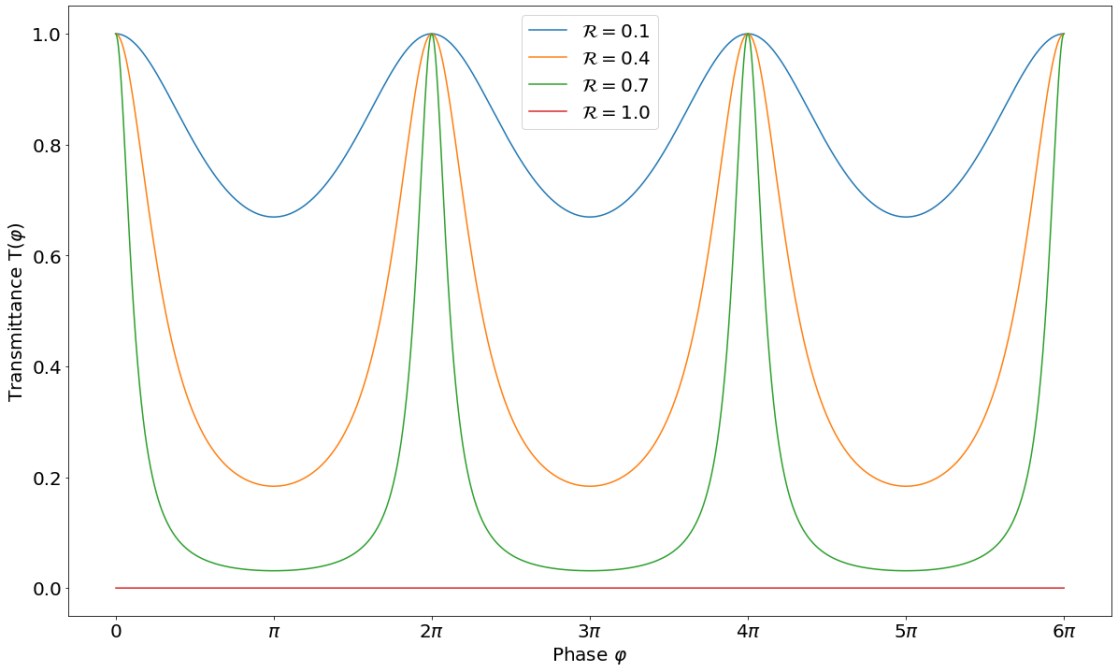


Figure 1.2: Steady-State Transmission spectrum for a Fabry-Perot Cavity for $\mathcal{R} = 0.1, 0.4, 0.7$ and 1.0

And from Eq. (1.9a) we get the total reflected field amplitude

$$\begin{aligned} E_R &= -\left[r_1 + it_1 \frac{it_1 r_2 \alpha^2 e^{-i\varphi}}{1 - r_1 r_2 \alpha^2 e^{-i\varphi}}\right] E_0 \\ &= -\frac{r_1 - r_2 \alpha^2 e^{-i\varphi}}{1 - r_1 r_2 \alpha^2 e^{-i\varphi}} E_0 \end{aligned} \tag{1.12}$$

where we have used $t_1^2 + r_1^2 = 1$ to arrive at the expression for E_R.

Similarly, we can write the beam-splitter relations for mirror M_2 with reflection and transmission coefficients r_2 and t_2 as

$$E_T = it_2 E_1 \tag{1.13a}$$

$$\text{and} \quad E_2 = -r_2 E_1 \tag{1.13b}$$

Here, again, $r_2, t_2 < 1$ and satisfy $r_2^2 + t_2^2 = 1$ as for M_1. Notice, these relations are stated without any input from mirror M_2 into the cavity. From Eq. (1.13a) we can now calculate

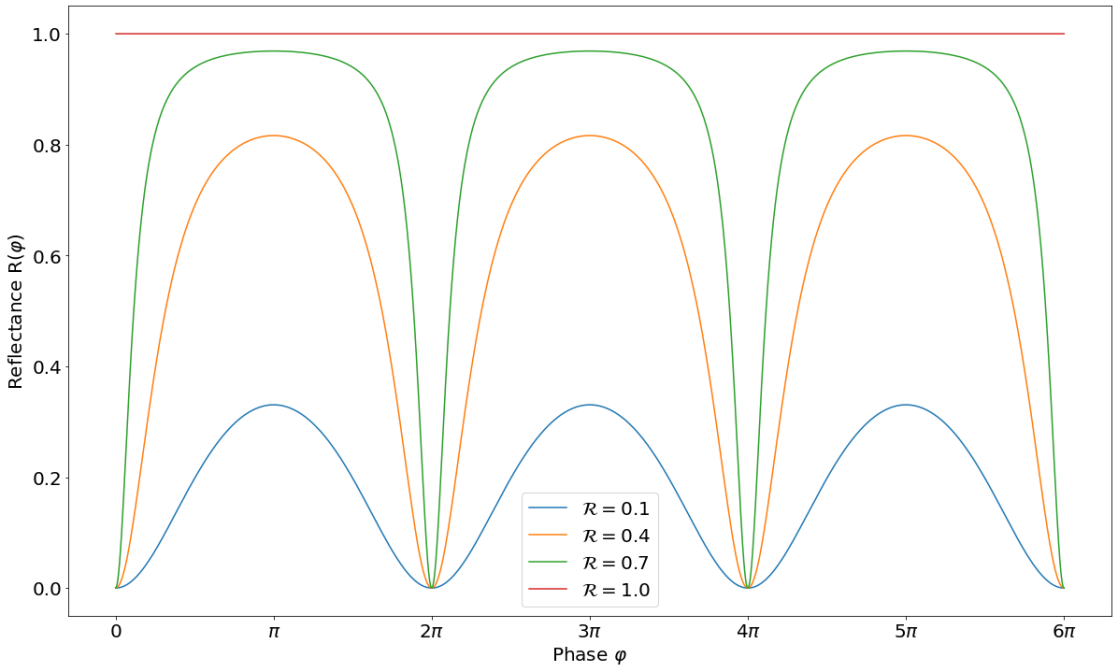


Figure 1.3: Steady-State Reflection spectrum for a Fabry-Perot Cavity for $\mathcal{R} = 0.1, 0.4, 0.7$ and 1.0

the total transmitted field amplitude as

$$E_T = it_2 E_1 = -\frac{\alpha t_1 t_2 e^{-i\varphi/2}}{1 - r_1 r_2 \alpha^2 e^{-i\varphi}} E_0 \tag{1.14}$$

where we have multiplied by $\alpha e^{-i\varphi/2}$ as we can expect the amplitude to attenuate by α and a phase delay of $e^{-i\varphi/2}$ before being transmitted out of the cavity.

Finally, the total cavity reflectance will be

$$R(\omega) = \left|\frac{E_R}{E_0}\right|^2 = \frac{r_1^2 + r_2^2\alpha^4 - 2r_1 r_2 \alpha^2 \cos\varphi}{1 + r_1^2 r_2^2 \alpha^4 - 2r_1 r_2 \alpha^2 \cos\varphi} \tag{1.15}$$

and the total cavity transmittance will be

$$T(\omega) = \left|\frac{E_T}{E_0}\right|^2 = \frac{t_1^2 t_2^2 \alpha^2}{1 + r_1^2 r_2^2 \alpha^4 - 2r_1 r_2 \alpha^2 \cos\varphi} = \frac{\alpha^2 (1 - r_1^2)(1 - r_2^2)}{1 + r_1^2 r_2^2 \alpha^4 - 2r_1 r_2 \alpha^2 \cos\varphi} \tag{1.16}$$

If we plot R and T against a frequency sweep of the input field, we see Lorentzian lineshapes as shown in Figures 1.2 and 1.3.

Let's take a closer look at these relations. We can simplify Eqs. (1.15) and (1.16) by considering the case of a symmetric lossless resonator such that $r_1 = r_2 = r$, $t_1 = t_2 = t$, and $\alpha = 1$ to give us

$$T(\omega) = \frac{(1-\mathcal{R})^2}{(1-\mathcal{R})^2 + 4\mathcal{R}\sin^2\varphi/2} \quad \text{and} \quad R(\omega) = \frac{4\mathcal{R}\sin^2\varphi/2}{(1-\mathcal{R})^2 + 4\mathcal{R}\sin^2\varphi/2} \tag{1.17}$$

where we have set $\mathcal{R} = r^2$. Notice that $R(\omega) + T(\omega) = 1$. In other words, the total energy will be conserved for a lossless resonator.

As can be seen in Figure 1.2, the transmittance achieves a maximum $T(\omega) = 1$ when $\sin\varphi/2 = 0$, or $\varphi = 2m\pi \;\forall\; m \in \mathbb{Z}$. Thus, all the power from the input gets transferred to the cavity output when

$$\omega_m = m\frac{\pi c}{nL}, \quad \forall\; m \in \mathbb{Z}, \tag{1.18}$$

which is the same condition for resonance frequencies as we saw in Eq. (1.7) with wave velocity $v = c/n$ and total round-trip cavity length $2L$. Thus, we expect the Lorentzian lineshapes to have maximas (resonance peaks) whenever the frequency of the input field matches the one of the resonant frequencies ω_m. And as before, the frequency spacing between two consecutive resonances peaks, or simply the free-spectral range of the resonator, will be $\omega_{FSR} = \omega_{m+1} - \omega_m = \pi c/nL$.

We can also derive an expression for the full-width at half-maxima for the Lorentzian peaks. For peaks with $(1-\mathcal{R}) << 1$, $T = 1/2$ whenever

$$\sin^2\varphi/2 = \frac{(1-\mathcal{R})^2}{4\mathcal{R}} \tag{1.19}$$

If we Taylor expand the phase about a resonant frequency $\omega_m = 2m\pi c/2nL$, we get $\varphi(\omega) \approx \varphi(\omega_m) + (\omega - \omega_m)\frac{\mathrm{d}\varphi}{\mathrm{d}\omega}|_{\omega_m} = 2m\pi + \Delta\varphi$ where $\Delta\varphi = (\omega - \omega_m)2nL/c = (2nL/c)\Delta\omega$. Therefore, $\sin^2\varphi/2 = \sin^2\Delta\varphi/2 \approx (\Delta\varphi/2)^2$ for small detunings from the resonance, and consequently

$$\frac{\Delta\varphi}{2} \approx \frac{1-\mathcal{R}}{2\sqrt{\mathcal{R}}}, \tag{1.20}$$

which gives us the linewidth of the resonator

$$\Delta\omega_{FWHM} = \frac{(1-\mathcal{R})}{\sqrt{\mathcal{R}}}\frac{c}{nL} \tag{1.21}$$

We can also define the Finesse of the resonator

$$\mathcal{F} = \frac{\omega_{FSR}}{\Delta\omega_{FWHM}} = \frac{\pi\sqrt{\mathcal{R}}}{1-\mathcal{R}} \tag{1.22}$$

Another important quantity associated with optical resonators is the Quality Factor Q which is described as the number of cycles it takes for the energy in the resonator to decay by $1/e$. More precisely, it is defined as

$$Q = \frac{2\pi(\text{energy stored})}{\text{energy loss per cycle}} \tag{1.23}$$

In terms of frequencies, the quality factor is the same as

$$Q = \frac{\omega_0}{\Delta\omega_{FWHM}} = \frac{\omega_0}{\omega_{FSR}}\mathcal{F} \tag{1.24}$$

where $\omega_0 = 2\pi c/\lambda_0$ is the central frequency of the input light.

1.3 Coupled-Mode theory

We will continue our analysis of the Fabry-Perot cavity, but study it with another powerful approach: Temporal Coupled-Mode Theory (CMT). In CMT, we consider a set of resonators and waveguides as shown in Figure 1.4 such that the former localize electromagnetic modes and the latter serve as inputs and outputs to the resonant cavities[17][18][19]. Further, the waveguides are assumed to be weakly coupled to the cavity such that the overall decay rate is presumed to be much longer than the time period of the cavity mode.

For resonant cavities, much like Eq. (1.4), we can write the total electric field inside the cavity as a sum over individual localized cavity modes as

$$\vec{E}(\vec{r}, t) = \sum_n a_n(t)\vec{E}_n(\vec{r}), \tag{1.25}$$

where $\vec{E}_n(\vec{r})$ represents the spatial distribution of the n^{th} cavity mode with a time-dependent amplitude $a_n(t)$. Note, we have substituted the time-dependence from $e^{i\omega t}$ to a general time-dependent amplitude $a_n(t)$ characteristic to the mode label n. This is important as CMT is the study of how these mode amplitudes vary with time subject to external couplings. This is akin to time-dependent perturbation theory in quantum mechanics where an atom coupled to an external environment is modeled as a time-dependent perturbation in the Hamiltonian, and subsequently the time-dependent Schrodinger's equation is solved to understand how the atom-environment system evolves with time. In a similar manner, here we can solve for the field distribution inside a cavity as a function of time by solving Maxwell's equation at every instant.

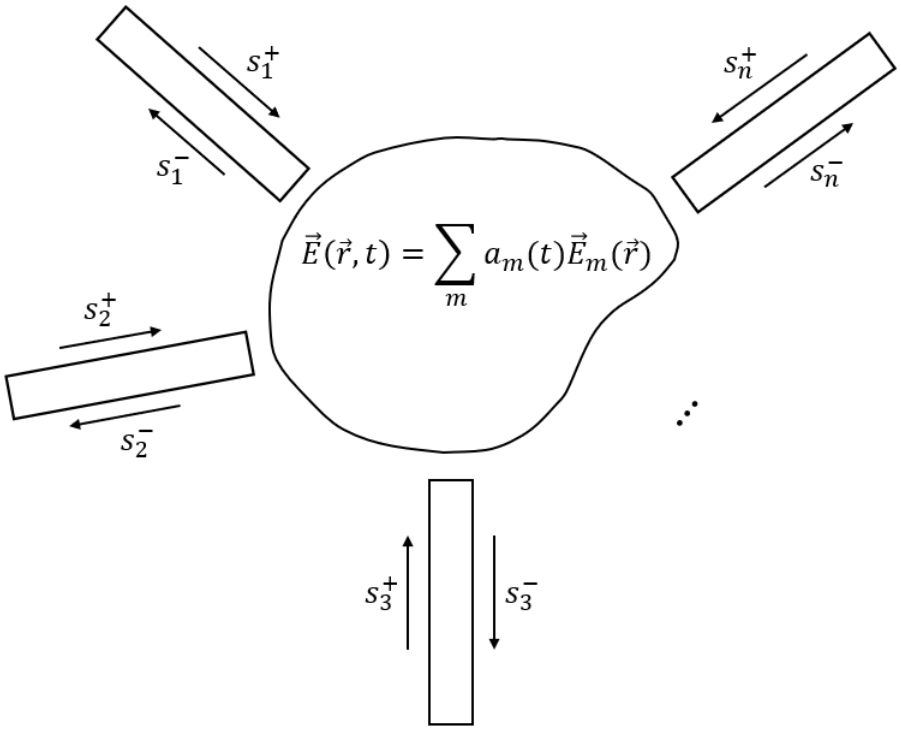


Figure 1.4: A diagram depicting a cavity connected to n waveguides. The cavity modes have time-dependent amplitudes $a_m(t)$ and the waveguide modes with fields going into and out of the cavity are depicted as s_n^+ and s_n^-, respectively.

Similarly, for a field propagating along the axis of a waveguide, we can write the total field as a sum of forward and backward propagating modes as

$$\vec{E}(\vec{r},t) = \sum_n [s_n^+(t)\vec{E}_n^+(\vec{r}) + s_n^-(t)\vec{E}_n^-(\vec{r})] = \sum_n [s_n^+(t)\vec{E}_n^+(\vec{r}) + \text{c.c.}], \tag{1.26}$$

where $\vec{E}_n^+(\vec{r})$ is a forward propagating mode with amplitude $s_n^+(t)$ and $\vec{E}_n^-(\vec{r})$ is a backward propagating mode with amplitude $s_n^-(t)$, and $s_n^-(t) = (s_n^+(t))^*$, where * denotes complex conjugation. Note, a forward propagating mode denotes a field going into the cavity and a backward propagating mode represents a field going out of a cavity. Further, using orthonormality conditions for a waveguide, it can be shown that the average power flowing into the waveguide at any instant of time is

$$P_{\text{avg}} = \sum_n [|s_n^+|^2 - |s_n^-|^2] \tag{1.27}$$

To understand how CMT works, let us just consider a single cavity and a single waveguide. Let the complex cavity mode amplitude be $a(t)$, and the waveguide input and output modes be $s^+(t)$ and $s^-(t)$, respectively. If the cavity and waveguide are completely decoupled, the dynamics of the cavity-waveguide system can be described with the following equations:

$$\frac{\mathrm{d}a}{\mathrm{d}t} = -i\omega_0 a(t) \tag{1.28a}$$

$$\text{and} \quad s^-(t) = e^{i\theta} s^+(t) \tag{1.28b}$$

Note, that the cavity mode is modeled as a first-order differential equation. Here, ω_0 is the resonant frequency of the cavity mode $a(t)$. Further, since the cavity and waveguide are presumed to be decoupled, we can expect the outgoing and ingoing propagating modes to differ by just a phase $e^{i\theta}$ as the outgoing mode will be just a reflection of the ingoing mode. Also, $|a(t)|^2$, $|s^+(t)|^2$, and $|s^-(t)|^2$ are the total energies in the cavity mode and ingoing and outgoing propagating waveguide modes at any time t, respectively.

Next, we couple the cavity and waveguide to get the equations of motion, i.e.,

$$\frac{\mathrm{d}a}{\mathrm{d}t} = -\left(i\omega_0 + \frac{1}{\tau}\right) a(t) + \gamma_1 s^+(t) \tag{1.29a}$$

$$\text{and} \quad s^-(t) = \gamma_2 s^+(t) + \gamma_3 a(t) \tag{1.29b}$$

Here, the cavity mode $a(t)$ is oscillating at a resonant frequency ω_0, but can also decay with lifetime τ. $1/\tau$ is the rate at which the cavity decays. These help us define the quality factor of the cavity mode as $Q = \omega_0\tau/2$. Note, since the cavity is only connected to one waveguide, the mode can only decay through this one channel. Also, the cavity is now excited by external radiation $s^+(t)$ with coupling strength γ_1 between cavity and the input waveguide mode. Interestingly, this is quite similar to a harmonic oscillator being driven by an external drive $s^+(t)$. Lastly, we expect the outgoing propagating mode to be a sum of the reflected ingoing wave $s^+(t)$ with reflection coefficient γ_2 and cavity mode with coupling strength γ_3 between the cavity and the output waveguide mode as the energy in the cavity decays into the waveguide. We will now determine how γ_1, γ_2, γ_3, and τ are related.

γ_3 can easily be determined by a conservation of energy argument. Let the cavity mode have an initial amplitude $a(0)$ at $t = 0$ with no input, i.e., $s^+(t) = 0$. Then we expect the cavity mode to simply leak into the waveguide. Eqs. (1.29) can then easily be solved for

$t > 0$ to give us

$$a(t) = a(0)e^{-i\omega_0 t - t/\tau} \tag{1.30a}$$

$$\text{and} \quad s^-(t) = \gamma_3 a(t) = \gamma_3 a(0)e^{-i\omega_0 t - t/\tau} \tag{1.30b}$$

Since the total energy is conserved, all the cavity radiation will leak into the mode s^-. Thus, we can integrate the waveguide mode over all time such that

$$\begin{aligned} |a(0)|^2 &= \int_0^\infty |s^-(t)|^2 \mathrm{d}t \\ &= \int_0^\infty |\gamma_3|^2 |a(0)|^2 e^{-2t/\tau} \mathrm{d}t \\ &= \frac{\tau}{2} |\gamma_3|^2 |a(0)|^2 \end{aligned} \tag{1.31}$$

This is possible only if $\gamma_3 = \sqrt{2/\tau}$, where we can expect the phase of $s^-(t)$ to be arbitrary. Thus, we see that the cavity-waveguide coupling coefficient is directly related to the rate at the which the cavity decays.

Next, we use time-reversal symmetry to find γ_1 and γ_2. A time-reversed electric field transforms as $\vec{E}(\vec{r}, t) \to \vec{E}^*(\vec{r}, -t)$ to maintain the form of Maxwell's equations. Further, if we reverse the time, we expect the waveguide to excite the cavity by $s^+(t)$ and we get the exponentially growing input

$$s^+(t) = \gamma_3 a^*(0) e^{-i\omega_0 t + t/\tau}, \quad \forall\ t < 0 \tag{1.32}$$

This is a result of conjugating the field in the waveguide $\vec{E}(\vec{r}, t)$ and letting $t \to -t$. Now we can easily integrate Eq. (1.29a) by multiplying both sides with the integrating factor $e^{i\omega_0 t + t/\tau}$ to get

$$\begin{aligned} &\frac{\mathrm{d}}{\mathrm{d}t}\left[a(t)e^{i\omega_0 t + t/\tau}\right] = \gamma_1 \gamma_3 a^*(0) e^{-i\omega_0 t + t/\tau} e^{i\omega_0 t + t/\tau} \\ \Rightarrow \quad &a(t)e^{i\omega_0 t + t/\tau} = \gamma_1 \gamma_3 a^*(0) \int e^{2t'/\tau} \mathrm{d}t' = \gamma_1 \gamma_3 a^*(0) \frac{\tau}{2} e^{2t/\tau} + \mathrm{C} \end{aligned} \tag{1.33}$$

where C is a constant of integration. To solve for C, we can impose the boundary condition $a(t \to -\infty) = 0$ for the time-reversed solution to get

$$a(t) = \gamma_1 \gamma_3 a^*(0) \frac{\tau}{2} e^{-i\omega_0 t + t/\tau}, \quad \forall\ t < 0 \tag{1.34}$$

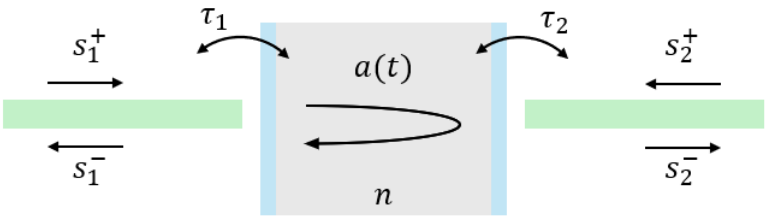


Figure 1.5: In the language of CMT, the Fabry-Perot cavity (containing a medium with refractive index n) can be analyzed as a single-mode cavity with mode amplitude $a(t)$ connected to two waveguide ports with ingoing field amplitudes s_1^+ and s_2^+ and outgoing field amplitudes s_1^- and s_2^-. The fields leak into and out of the cavity via the two waveguides with lifetimes τ_1 and τ_2.

But a time-reversed solution of Eq.(1.30a) will simply be $a(t) = a^*(0)e^{-i\omega_0 t + t/\tau}, \quad \forall\, t < 0$. Comparing this to Eq. (1.34) now gives us $\gamma_1\gamma_3\tau/2 = 1$. Using $\gamma_3 = \sqrt{2/\tau}$, we now have the coupling strength $\gamma_1 = \sqrt{2/\tau} = \gamma_3$. Thus, we come to an important conclusion that the coupling strength between the cavity and input waveguide mode is the same as the coupling strength between the cavity and the output waveguide mode. In other words, the waveguide excites the cavity at the same rate as when the energy in the cavity leaks into the waveguide.

Lastly, since we presumed the cavity to be excited by an ingoing field $s^+(t)$ in the time-reversed case, we can expect $s^-(t) = 0$. Substituting Eqs. (1.34) and (1.32) in Eq. (1.29b) gives us

$$\gamma_2 s^+(t) + \gamma_3 a(t) = \gamma_3 a^*(0)e^{-i\omega_0 t + t/\tau}(\gamma_2 + 1) = 0 \tag{1.35}$$

This gives us $\gamma_2 = -1$ as $a(0) \neq 0$. In other words, a reflection simply changes the phase of the ingoing field by π.

Thus, we finally get our coupled-mode equations of motion for a cavity connected to a single waveguide as

$$\frac{\mathrm{d}a}{\mathrm{d}t} = -\left(i\omega_0 + \frac{1}{\tau}\right) a(t) + \sqrt{\frac{2}{\tau}} s^+(t) \tag{1.36a}$$

$$\text{and} \quad s^-(t) = -s^+(t) + \sqrt{\frac{2}{\tau}} a(t) \tag{1.36b}$$

Extending this model to the case of a Fabry-Perot cavity is a simple matter of noticing that the cavity will now be connected to two waveguides as shown in Figure 1.5. Since

there are two waveguides, there will be two ingoing ($s_1^+(t)$ and $s_2^+(t)$) and outgoing ($s_1^-(t)$ and $s_2^-(t)$) waveguide modes with decay rates $1/\tau_1$ and $1/\tau_2$ for each waveguide. These decay rates also give us external quality factors $Q_1 = \omega_0\tau_1/2$ and $Q_2 = \omega_0\tau_2/2$ between the cavity and the waveguide modes. Again, we are only considering the ideal case where the cavity decays only via the two waveguides and there is no other source of leakage for the energy inside the cavity. Denoting the total cavity decay rate as $1/\tau = 1/\tau_1 + 1/\tau_2$, the equations of motion for a 2-port cavity will now change to

$$\frac{\mathrm{d}a}{\mathrm{d}t} = -\left(i\omega_0 + \frac{1}{\tau}\right)a(t) + \sqrt{\frac{2}{\tau_1}}s_1^+(t) + \sqrt{\frac{2}{\tau_2}}s_2^+(t), \tag{1.37a}$$

$$s_1^-(t) = -s_1^+(t) + \sqrt{\frac{2}{\tau_1}}a(t), \tag{1.37b}$$

$$\text{and} \quad s_2^-(t) = -s_2^+(t) + \sqrt{\frac{2}{\tau_2}}a(t) \tag{1.37c}$$

But in the case of a Fabry-Perot cavity as in the previous section, the input was only from port 1. Thus, with $s_2^+(t) = 0$ we get the equations of motion

$$\frac{\mathrm{d}a}{\mathrm{d}t} = -\left(i\omega_0 + \frac{1}{\tau_1} + \frac{1}{\tau_2}\right)a(t) + \sqrt{\frac{2}{\tau_1}}s_1^+(t), \tag{1.38a}$$

$$s_1^-(t) = -s_1^+(t) + \sqrt{\frac{2}{\tau_1}}a(t), \tag{1.38b}$$

$$\text{and} \quad s_2^-(t) = \sqrt{\frac{2}{\tau_2}}a(t) \tag{1.38c}$$

Experimentally, we usually excite a cavity with an input signal modulated by a function like a ramp which allows us to set the frequency scale for the cavity reflection and transmission spectrum. Thus, it would be fruitful to see the solution of Eqs. (1.38) in the frequency space by taking their Fourier transform:

$$-i\omega a(\omega) = -\left(i\omega_0 + \frac{1}{\tau_1} + \frac{1}{\tau_2}\right)a(\omega) + \sqrt{\frac{2}{\tau_1}}s_1^+(\omega), \tag{1.39a}$$

$$s_1^-(\omega) = -s_1^+(\omega) + \sqrt{\frac{2}{\tau_1}}a(\omega), \tag{1.39b}$$

$$\text{and} \quad s_2^-(\omega) = \sqrt{\frac{2}{\tau_2}}a(\omega) \tag{1.39c}$$

Unlike solving the differential equation for $a(t)$, notice that Eqs. (1.39) are simple linear equations. We can now easily solve for $a(\omega)$ to get

$$a(\omega) = -\frac{\sqrt{2/\tau_1}}{i(\omega - \omega_0) - (1/\tau_1 + 1/\tau_2)} s_1^+(\omega) \tag{1.40}$$

Recall, the expressions for the steady-state transmission and reflection for a cavity with input in port 1 are $T(\omega) = |s_2^-(\omega)/s_1^+(\omega)|^2$ and $R(\omega) = |s_1^-(\omega)/s_1^+(\omega)|^2$. Substituting $a(\omega)$ in the equations for $s_1^-(\omega)$ and $s_2^-(\omega)$ now gives us

$$T(\omega) = \left|\frac{s_2^-(\omega)}{s_1^+(\omega)}\right|^2 = \frac{4/\tau_1\tau_2}{(\omega - \omega_0)^2 + (1/\tau_1 + 1/\tau_2)^2} \tag{1.41a}$$

$$\text{and} \quad R(\omega) = \left|\frac{s_1^-(\omega)}{s_1^+(\omega)}\right|^2 = \frac{(\omega - \omega_0)^2 + (1/\tau_1 - 1/\tau_2)^2}{(\omega - \omega_0)^2 + (1/\tau_1 + 1/\tau_2)^2} \tag{1.41b}$$

It is also fairly easy to show that $T(\omega) + R(\omega) = 1$ as the energy remains conserved. It is interesting to notice that, as in the previous section, the cavity transmission (reflection) are Lorentzian lineshapes with maximas (minimas) at cavity resonances with linewidth dependent on $1/\tau$. Experimentally, when we drive our cavities with a ramp function, we will see transmission maximas (or reflection minimas) whenever the frequency of the input is a cavity resonance. Theoretical lineshapes of Eqs. (1.41) are shown in Figure 1.6.

To see how Eqs. (1.41) are related to Eqs. (1.16) and (1.15), we will use the Taylor expansion of the round-trip phase up to first order again to get

$$\begin{aligned} \cos\varphi &= \cos\left[2m\pi + \Delta\varphi\right] \\ &= \cos\Delta\varphi \approx 1 - \frac{(\Delta\varphi)^2}{2} \\ &\approx 1 - \frac{2(\omega - \omega_m)^2 n^2 L^2}{c^2} \end{aligned} \tag{1.42}$$

Substituting $\cos\varphi$ in Eq. (1.16) now gives us

$$T(\omega) \approx \frac{\alpha(1 - r_1^2) \cdot \alpha(1 - r_2^2)}{(1 - r_1 r_2 \alpha^2)^2 + 4 r_1 r_2 (\alpha n L/c)^2 (\omega - \omega_m)^2} \tag{1.43}$$

If we compare the denominator of Eq. (1.43) to Eq. (1.41a), we can extract the total cavity decay rate

$$\frac{1}{\tau} = \frac{1 - r_1 r_2 \alpha^2}{\alpha\sqrt{r_1 r_2}} \frac{c}{2nL} \tag{1.44}$$

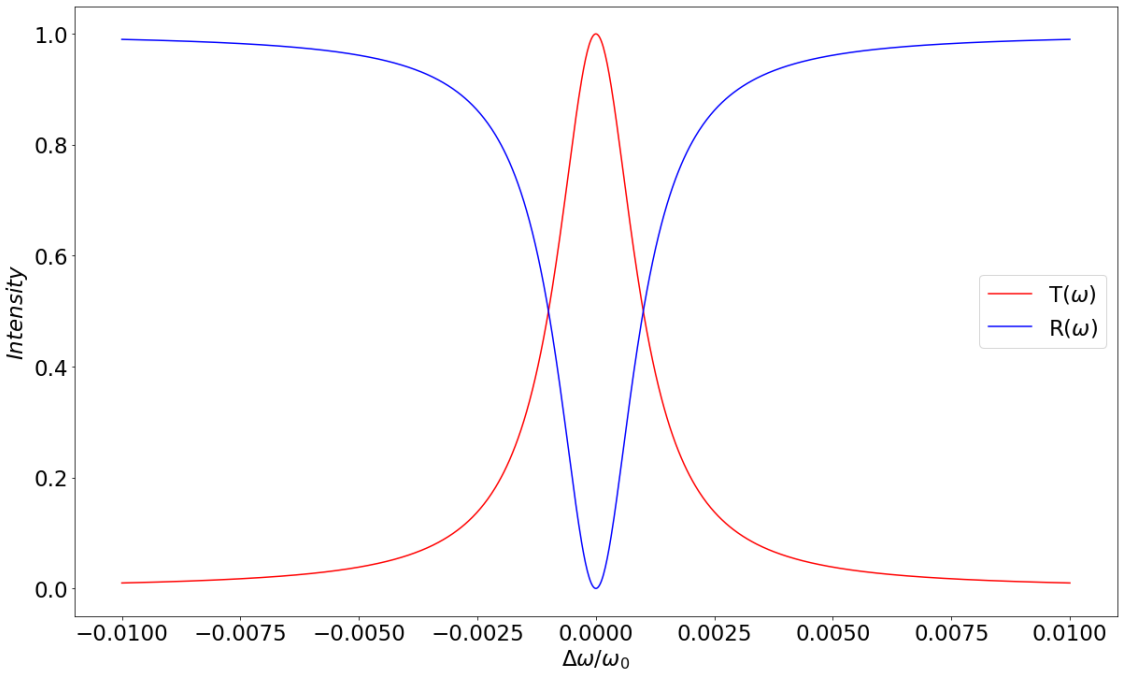


Figure 1.6: Steady-State Transmission $T(\omega)$ and Reflection $R(\omega)$ spectrum for a Fabry-Perot Cavity with cavity-waveguide external quality factors $Q_1 = Q_2 = 1000$ showing a resonance when the cavity detuning $\Delta\omega = \omega_0$. Note, for these simulations we normalized T and R by ω_0.

and the external quality factor

$$Q = \frac{\omega_0 \tau}{2} = \frac{\omega_0 nL}{c} \frac{\alpha\sqrt{r_1 r_2}}{1 - r_1 r_2 \alpha^2} \tag{1.45}$$

We can now analyze the cavity decay for the case of a low-loss resonator with $\alpha = 1$ and $t_1, t_2 \to 0$. In this situation, we can Taylor expand r_1 and r_2 such that $r_1 = (1 - t_1^2)^{1/2} \approx 1 - t_1^2/2$ and $r_2 = (1 - t_2^2)^{1/2} \approx 1 - t_2^2/2$. Moreover, $\sqrt{r_1 r_2} \to 1$ for small t_1 and t_2. Thus, we can approximate the cavity decay and get

$$\begin{aligned} \frac{1}{\tau} &\approx \frac{c}{2nL}\left[1 - \left(1 - \frac{t_1^2}{2}\right)\left(1 - \frac{t_2^2}{2}\right)\right] \\ &\approx \frac{c}{2nL}\left[\frac{t_1^2}{2} + \frac{t_2^2}{2}\right] = \frac{1}{\tau_1} + \frac{1}{\tau_2} \end{aligned} \tag{1.46}$$

Thus, we can now easily conclude that the decay rate $1/\tau_i (i = 1, 2)$ through each mirror is dependent on the transmittance t_i^2 of the mirror. Thus, for a low-loss resonator, we can re-write Eq. (1.43) as

$$\begin{aligned} T(\omega) &\approx \frac{(1 - r_1^2)(1 - r_2^2)}{(1 - r_1 r_2)^2 + 4 r_1 r_2 (nL/c)^2 (\omega - \omega_m)^2} \\ &\approx \frac{\frac{t_1^2}{2nL/c}\frac{t_2^2}{2nL/c}}{(\omega - \omega_m)^2 + 1/\tau^2} \\ &= \frac{4/\tau_1 \tau_2}{(\omega - \omega_m)^2 + 1/\tau^2} \end{aligned} \tag{1.47}$$

as we saw in Eq. (1.41a). Further, it can also be shown in a similar fashion that the cavity reflection $R(\omega)$ in Eq. (1.41b) is the same as Eq. (1.15) in the low-loss limit.

We now conclude our analysis of the Fabry-Perot resonator and are in a strong position to extend the results to the case of a ring resonator and understand its transmission characteristics.

Chapter 2

All Fiber-Optic Ring Resonators

Contributions

Bharat Kuchhal did the literature survey, performed all numerical calculations and simulations, developed the setup, took experimental data, and performed data analysis in this chapter.

Prof. Christopher Wilson devised the study for the Drift calculations in Section 2.2.2.

Prof. Kevin Resch devised the method to understand the laser frequency sweep.

2.1 Overview

A simple ring resonator is a closed-loop optical waveguide which is excited by rectangular bus waveguides either evanescently or via beam-splitters[20][21]. The closed-loop configuration allows multiple resonances, and each resonance occurs whenever the condition for constructive interference is met, i.e., the round-trip phase shift is an integer multiple of 2π. More concisely, $kL = 2m\pi$, $\forall\ m \in \mathbb{Z}$ where the propagation constant $k = 2\pi n_g/\lambda$, n_g is the group index of the medium, L is the circumference of the ring, and λ is the free space wavelength of the incident light. This property has spawned plethora of applications of ring resonators in wavelength-division multiplexing, development of tunable filters[22], whispering gallery mode based optical switches via four-wave mixing processes[23], and even photon-pair generation via spontaneous parametric downconversion[24].

Ring resonators are developed either in the all-pass configuration as shown in Fig. 2.1(a) where the ring is coupled to a single bus waveguide for both input and output, or in the add-drop configuration where the ring is coupled to a bus and a receiver waveguide as shown in Fig. 2.1(b) and the output can be seen both at the drop and through ports of the cavity. In this chapter, we will first theoretically develop a CMT for the all-pass configuration, and extend the theory to the add-drop configuration. The latter will be studied in more detail experimentally with 99:1 beam-splitters. Subsequently, we will modify the add-drop ring by adding a Dense-Wavelength Division Multiplexing (DWDM) filter, a booster optical amplifier (BOA), and a periodically-poled Lithium Niobate ($LiNbO_3$) electro-optic modulator (EOM). In the next chapter, we will modulate the cavity signal by providing a sinusoidal modulation to the EOM and observe how the non-linearity of the $LiNbO_3$ crystal couples the frequency modes of the cavity leading to a band structure in time.

2.2 Theory

In this section, we will first theoretically study the all-pass configuration, and then proceed to the add-drop configuration as it is the configuration we used to prepare our experimental setup. As mentioned earlier, in the all-pass configuration, the ring is coupled to a single waveguide for both input and output. And in the add-drop configuration, the ring is coupled to two waveguides. Since we will experimentally study an all-optical fiber-ring resonator, it suffices to say that we aim at coupling the light into and out of the cavity via fiber beam-splitters. Thus, we will develop a theory, including coupled-mode theory, to first theoretically study the transmission characteristics of a simple ring consisting of two 99:1 beam-splitters excited by a telecom wavelength ($\lambda = 1550$ nm) laser. As indicated in Fig. 2.1, the light will enter through one port of the bus waveguide. For an all-pass configuration, the transmission output is only observed at the Through port. But for an add-drop configuration, the output can be seen via both the bus and receiver waveguides at the Through and Drop ports. As we will see later, the Drop and Through port outputs are usually Lorentzians and inverted Lorentzians about the resonant frequencies.

2.2.1 All-Pass Ring Resonator

As can be seen in Fig. 2.1, a ring resonator is a curved waveguide. Thus, we expect the electric field inside the waveguide to propagate as $E(\vec{r}, t) \propto \exp\{ik(\omega)R\phi\}$, where $k(\omega)$ is the propagation vector, R is the radius of the ring, and ϕ is the polar angle. Since the waveguide is curved into a ring, we can expect the ring to be lossy and consequently

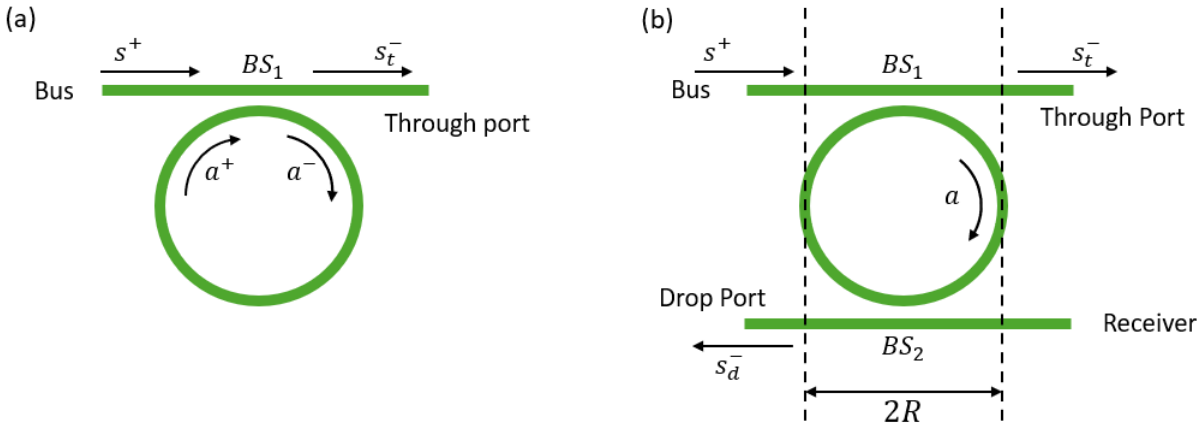


Figure 2.1: (a) All-Pass Ring Resonator; (b) Add-Drop Ring Resonator; BS: Beam-Splitter, R: Radius of Ring

$k(\omega)$ will have an imaginary part $\alpha(\omega)$—measured in dB/m—to characterize the waveguide loss[19][21][22].

We will now develop a theoretical understanding of the transmission characteristics of an all-pass ring resonator the same way as we did in Chapter 1 by looking at the Fabry-Perot relations between electric-fields. Let s^+ and s_t^- be the input and output field amplitudes in the bus waveguide. The subscript t denotes that the output is via the Through port of the cavity-bus system. And let a^+ and a^- be the field amplitudes for EM waves moving towards and away from the beam-splitter inside the ring. Note that we are mixing notation for a here between cavity and waveguide modes. Although a represents the field amplitude inside the cavity, we are using the superscripts "+" and "–" to represent the fields going in or out of the beam-splitter. We will later see how the waveguide mode a^+ (and consequently a^-) is related to the cavity mode a. Further, since light is being coupled into the cavity via a fiber beam-splitter, we can write relations between the field amplitudes as

$$s_t^-(\omega) = r_1 s^+(\omega) + i t_1 a^+(\omega) \tag{2.1a}$$

$$\text{and} \quad a^-(\omega) = i t_1 s^+(\omega) + r_1 a^+(\omega), \tag{2.1b}$$

where r_1 and t_1 are (real) amplitude reflection and transmission coefficients of the beam-splitter satisfying $r_1^2 + t_1^2 = 1$ with $r_1, t_1 < 1$. Note, the field amplitudes are chosen to be in the frequency space. Further, let the round-trip phase shift be $\varphi(\omega)$. Thus, we can write the input amplitude in terms of the output amplitude as

$$a^+(\omega) = \alpha e^{i\varphi(\omega)} a^-(\omega) \tag{2.2}$$

Notice, $a^+(\omega)$ is dependent on α as the field inside will attenuate every round-trip. Also, for one round-trip, the phase shift will be $\varphi(\omega) = k(\omega)L$ where $L = 2\pi R$ is the circumference of the ring.

Substituting Eq. (2.2) in Eq. (2.1b), we get

$$a^+(\omega) = \frac{i\alpha t_1 e^{i\varphi(\omega)}}{1 - \alpha r_1 e^{i\varphi(\omega)}} s^+(\omega) \tag{2.3}$$

and from Eq. (2.1a), we get

$$\frac{s_t^-(\omega)}{s^+(\omega)} = \frac{r_1 - \alpha e^{i\varphi(\omega)}}{1 - r_1\alpha e^{i\varphi(\omega)}} \tag{2.4}$$

Thus, we get the steady-state transmission for an all-pass ring resonator via the Through port[25] as

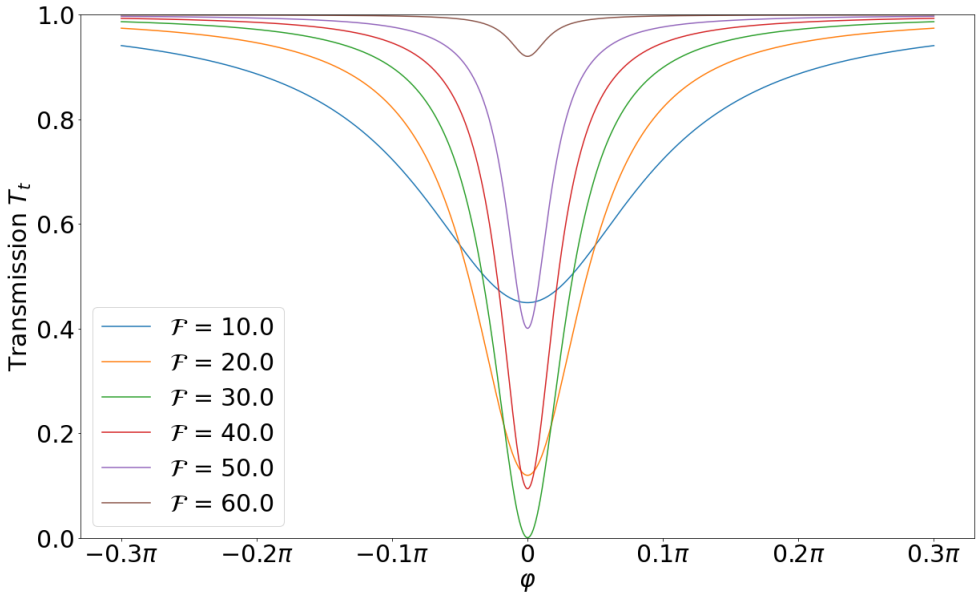
$$T_t(\omega) = \left|\frac{s_t^-}{s^+}\right|^2 = \frac{r_1^2 + \alpha^2 - 2r_1\alpha\cos\varphi}{1 + r_1^2\alpha^2 - 2r_1\alpha\cos\varphi} \tag{2.5}$$

Furthermore, the output field will be phase shifted from the input by

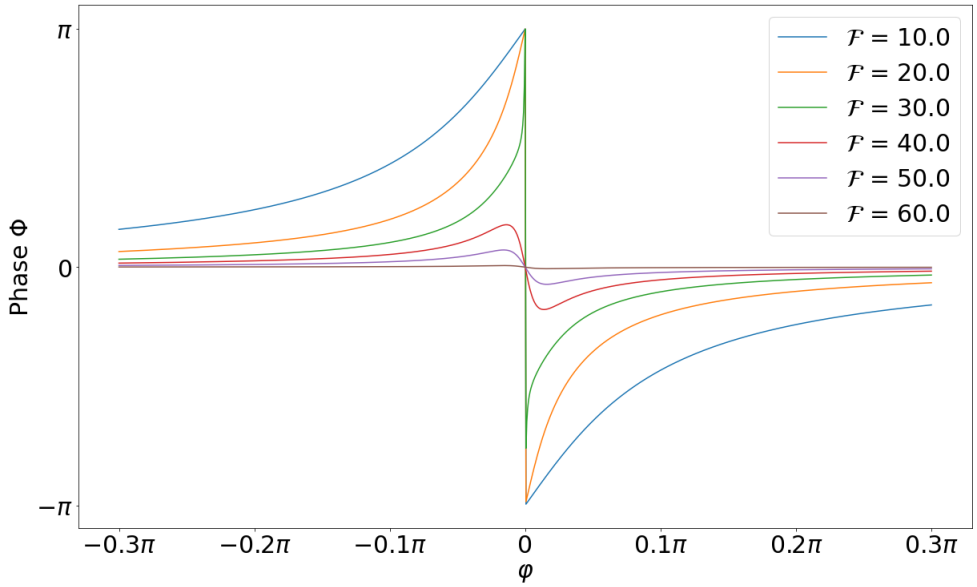
$$\begin{aligned} \Phi &= \arg\left(\frac{s_t^-(\omega)}{s^+(\omega)}\right) \\ &= \pi + \varphi + \tan^{-1}\left[\frac{r_1\sin\varphi}{\alpha - r_1\cos\varphi}\right] + \tan^{-1}\left[\frac{\alpha r_1\sin\varphi}{1 - r_1\alpha\cos\varphi}\right] \end{aligned} \tag{2.6}$$

From Eq. (2.5) it can easily be seen that $T(\omega) = 0$ when the round-trip phase $\varphi = 2m\pi$, $\forall\ m \in \mathbb{Z}$ and $r_1 = \alpha$. This is the critically coupled on-resonance condition when the coupling losses are the same as the internal losses. Thus, we can expect the coupling losses will be higher than internal losses ($r_1 > \alpha$) for an under-coupled cavity and lower ($r_1 < \alpha$) for an over-coupled cavity. It is quite interesting to note that in the lossless case ($\alpha = 1$), the cavity transmission $T(\omega) = 1$, $\forall\ \omega$. Recall, in Chapter 1 we noted that cavity loss can be theoretically modeled as another waveguide port. If we now assume an all-pass cavity to be lossless, we can expect—by energy conservation—all the radiation to leak out only via a single Through port giving us $T(\omega) = 1$. Thus, we can conclude that resonance peaks or dips are a consequence of a lossy ring with $\alpha \neq 0$.

From the resonance condition $\varphi = 2m\pi$, we get $k_m = 2m\pi/L$ or resonance frequencies $\omega_m = 2m\pi c/n_g L$, where n_g is the group index of the fiber medium and $v_g = c/n_g$ is the group velocity of the field inside the medium. Thus, as before, the free-spectral range will



(a)



(b)

Figure 2.2: (a) Transmission Spectrum $T_t(\varphi)$ and (b) Phases $\Phi(\varphi)$ for an all-pass ring resonator with $\alpha = 0.95$, and Finesse values 10, 20, 30, 40, 50, and 60

be $\omega_{FSR} = \omega_{m+1} - \omega_m = 2\pi c/n_g L$. By Taylor expanding the phase φ around a resonance frequency ω_m up to the first order we get

$$\begin{aligned} \varphi(\omega) &\approx \varphi(\omega_m) + (\omega - \omega_m)\frac{\mathrm{d}\varphi}{\mathrm{d}\omega}\bigg|_{\omega_m} \\ &= 2m\pi + (\omega - \omega_m)\frac{L}{v_g} \end{aligned} \tag{2.7}$$

Using $\cos\varphi = \cos\left[2m\pi + (\omega - \omega_m)\frac{n_g L}{c}\right] = \cos\left[(\omega - \omega_m)n_g L/c\right] \approx 1 - (\omega - \omega_m)^2 L^2/2v_g^2$ and substituting it in Eq.(2.5) now gives us the transmission via the Through port as

$$\begin{aligned} T_t(\omega) &\approx \frac{r_1^2 + \alpha^2 - 2r_1\alpha(1 - (\omega - \omega_m)^2 L^2/2v_g^2)}{1 + \alpha^2 r_1^2 - 2r_1\alpha(1 - (\omega - \omega_m)^2 L^2/2v_g^2)} \\ &= \frac{(r_1 - \alpha)^2 + r_1\alpha(\omega - \omega_m)^2 L^2/v_g^2}{(1 - r_1\alpha)^2 + r_1\alpha(\omega - \omega_m)^2 L^2/v_g^2} \\ &= 1 - \frac{(1 - r_1^2)(1 - \alpha^2)}{(1 - r_1\alpha)^2 + r_1\alpha(\omega - \omega_m)^2 L^2/v_g^2} \end{aligned} \tag{2.8}$$

We can now extract the cavity decay from $T(\omega)$ as

$$\begin{aligned} \frac{1}{\tau^2} &= \frac{v_g^2}{L^2}\frac{(1 - r_1\alpha)^2}{r_1\alpha} \\ \Rightarrow \quad \tau &= \frac{L}{v_g}\frac{\sqrt{r_1\alpha}}{1 - r_1\alpha} \end{aligned} \tag{2.9}$$

And we finally get the quality factor of the ring resonator as

$$Q = \frac{\omega_0\tau}{2} = \frac{\omega_0 L\sqrt{r_1\alpha}}{2v_g(1 - r_1\alpha)} \tag{2.10}$$

and the finesse as

$$\mathcal{F} = \frac{\omega_{FSR}}{\omega_0}Q = \frac{\pi\sqrt{r_1\alpha}}{1 - r_1\alpha} \tag{2.11}$$

Figure 2.2 shows transmission spectrum and phase shift of output fields given by Eqs. (2.5) and (2.6) for fixed round-trip loss $\alpha = 0.95$ and different finesse values for an all-pass ring resonator. Notice that $T_t(\varphi = 0) \to 0$ for $\mathcal{F} = 30$. This is the critically-coupled case where $r_1 = 0.948 \approx \alpha$. For $\mathcal{F} < 30$, we can observe that the inverted Lorentzians are broader as this is the under-coupled regime where $r_1 < \alpha$. On the other hand, for $\mathcal{F} > 30$,

the Lorentzians are narrower and shorter corresponding to the over-coupled regime with $r_1 > \alpha$.

Notice that cavity loss occurs via 2 mechanisms —intrinsic losses due to a finite α and coupling losses due to a nonzero t_1. For a low-loss resonator, $\alpha \to 1$ and $t_1 \to 0$. Thus, $r_1 = (1 - t_1^2)^{1/2} \approx 1 - t_1^2/2$ and $\sqrt{r_1 \alpha} \approx 1$. Consequently, we can re-write the quality factor Q as

$$\frac{1}{Q} \approx \frac{2v_g}{\omega_0 L}\left[1 - \left(1 - \frac{t_1^2}{2}\right)\alpha\right] = \frac{2v_g}{\omega_0 L}(1-\alpha) + \frac{v_g t_1^2}{\omega_0 L} = \frac{1}{Q_i} + \frac{1}{Q_c}, \tag{2.12}$$

where Q_i and Q_c are known as intrinsic and external coupling quality factors, respectively, denoting intrinsic cavity losses and external losses due to the coupling with the bus waveguide.

We can also use Eqs. (2.1) to develop a coupled mode theory of an all-pass ring resonator. Eq. (2.1a) will remain as is. But we can use Eq. (2.7) to Taylor expand the phase up to first order and get

$$\begin{aligned} \exp(-i\varphi(\omega)) &\approx \exp[-i(2m\pi + (\omega - \omega_m)\tau_g)] \\ &= \exp[-i(\omega - \omega_m)\tau_g)] \\ &\approx 1 - i(\omega - \omega_m)\tau_g \end{aligned} \tag{2.13}$$

where $\tau_g = L/v_g$. From Eq. (2.1b) and Eq. (2.2) we now get

$$\begin{aligned} & e^{-i\varphi(\omega)} a^+(\omega) = it_1 \alpha s^+(\omega) + r_1 \alpha a^+(\omega) \\ \Rightarrow \quad & a^+(\omega) - i(\omega - \omega_m)\tau_g a^+(\omega) = it_1 \alpha s^+(\omega) + r_1 \alpha a^+(\omega) \end{aligned} \tag{2.14}$$

Since $a^+(\omega)$ also represents a cavity mode, we can simplify the expression by defining cavity mode $a(\omega) = a^+(\omega)\sqrt{\tau_g}$. To get the equation of motion in the time domain, we can take the inverse Fourier transform of Eq. (2.14) to get

$$\sqrt{\tau_g}\frac{\mathrm{d}a(t)}{\mathrm{d}t} = -i\omega_m \sqrt{\tau_g} a(t) - \frac{1}{\sqrt{\tau_g}}(1 - r_1\alpha)a(t) + it_1 \alpha s^+(t) \tag{2.15}$$

Again, as we saw in Eq. (2.12), $\alpha \to 1$ and $(1 - r_1\alpha) \approx (1 - \alpha) + t_1^2/2$ in the low-loss limit. Dividing the differential equation by $\sqrt{\tau_g}$ and substituting these values now gives us

$$\frac{\mathrm{d}a(t)}{\mathrm{d}t} = -i\omega_m a(t) - \left[\frac{1-\alpha}{\tau_g} + \frac{t_1^2}{2\tau_g}\right] a(t) + i\frac{t_1}{\sqrt{\tau_g}} s^+(t) \tag{2.16}$$

We can now define intrinsic and extrinsic cavity decay rates

$$\tau_i \approx \frac{\tau_g}{(1-\alpha)} \quad \text{and} \quad \tau_1 \approx \frac{2\tau_g}{t_1^2} \tag{2.17}$$

And we finally get the equation of motion for the cavity mode as

$$\frac{\mathrm{d}a(t)}{\mathrm{d}t} \approx -i\omega_m a(t) - \left[\frac{1}{\tau_i} + \frac{1}{\tau_1}\right] a(t) + i\sqrt{\frac{2}{\tau_1}} s^+(t) \tag{2.18}$$

We can also take the inverse Fourier transform and re-write Eq. (2.1a) in the low-loss limit as

$$\begin{aligned} & s_t^-(\omega) = r_1 s^+(\omega) + i t_1 a^+(\omega) \\ \Rightarrow \quad & s_t^-(t) \approx s^+(t) + i\sqrt{\frac{2}{\tau_1}} a(t) \end{aligned} \tag{2.19}$$

Notice, in the above equation, $s_t^-(t) \propto +s^+(t)$ and not $-s^+(t)$ as the output seen in the through port is due to the direct transmission (not reflection) of the input energy. Lastly, Eqs. (2.18) and (2.19) are the combined equations of motion for the CMT of an all-pass ring resonator.

2.2.2 Add-drop Ring Resonator

As with the Fabry-Perot cavity connected with 2 ports for output, we can now easily extend the above analysis to an add-drop ring resonator as in Fig. 2.1b. Since the receiver waveguide is decoupled from the bus waveguide, Eq. (2.19) will remain as is. But the equation of motion for the field amplitude in the cavity will now exhibit a decay through both bus and receiver waveguides[22]. Thus, Eq. (2.18) will modify to

$$\frac{\mathrm{d}a(t)}{\mathrm{d}t} \approx -i\omega_m a(t) - \left[\frac{1}{\tau_i} + \frac{1}{\tau_1} + \frac{1}{\tau_2}\right] a(t) + i\sqrt{\frac{2}{\tau_1}} s^+(t) \tag{2.20}$$

Note, the input $s^+(t)$ is still only via the first beam-splitter. We will not consider any input via the second receiver waveguide in the add-drop configuration. Thus, the equation of motion for the drop port will now simply be

$$s_d^-(t) = i\sqrt{\frac{2}{\tau_2}} a(t), \tag{2.21}$$

where $\tau_2 \approx 2\tau_g/t_2^2$ is the decay rate between cavity and receiver waveguide via the second beam-splitter. Finally, Eqs. (2.19), (2.20), and (2.21) will together constitute the equations of motion for the CMT of an add-drop ring resonator with the total cavity decay rate

$$\frac{1}{\tau} = \frac{1}{\tau_i} + \frac{1}{\tau_1} + \frac{1}{\tau_2} \tag{2.22}$$

Notice the resemblance between Eqs. (2.19), (2.20), and (2.21) and the equations of motion in Eqs. (1.38). We just obtained the exact same equations of motion for an add-drop ring resonator as that of a 2-port Fabry-Perot cavity with a few phase differences. Thus, we can follow the procedure laid out in Sec. 1.2 and extend our results to get the steady-state transmission for an add-drop ring resonator via the drop port[20]

$$T_d(\omega) = \left|\frac{s_d^-}{s_0}\right|^2 = \frac{4/\tau_1\tau_2}{(\omega-\omega_m)^2 + 1/\tau^2} = \frac{\alpha(1-r_1^2)(1-r_2^2)}{1 + r_1^2 r_2^2 \alpha^2 - 2r_1 r_2 \alpha \cos\varphi} \tag{2.23}$$

and via the through port as

$$T_t(\omega) = \left|\frac{s_t^-}{s_0}\right|^2 = \frac{(\omega-\omega_m)^2 + (1/\tau_i - 1/\tau_1 + 1/\tau_2)^2}{(\omega-\omega_m)^2 + 1/\tau^2} = \frac{r_1^2 + r_2^2\alpha^2 - 2r_1 r_2 \alpha \cos\varphi}{1 + r_1^2 r_2^2 \alpha^2 - 2r_1 r_2 \alpha \cos\varphi} \tag{2.24}$$

Notice that we have replaced the intrinsic cavity decay α^2 in the expressions for the Fabry-Perot resonator with the round-trip cavity loss α for a ring resonator.

Further, the total quality factor for an add-drop ring resonator will be

$$Q = \frac{\omega_0 \tau}{2} = \frac{\omega_0 L \sqrt{r_1 r_2 \alpha}}{2v_g(1 - r_1 r_2 \alpha)} \tag{2.25}$$

such that in the low-loss limit where $\alpha \to 1$, and $t_1, t_2 \to 0$, we can get $\sqrt{r_1 r_2 \alpha} \to 1$, $1 - r_1 r_2 \alpha = 1 - (1-t_1^2)^{1/2}(1-t_2^2)^{1/2}\alpha \approx 1 - (1 - t_1^2/2 - t_2^2/2)\alpha$, and finally

$$\begin{aligned} \frac{1}{Q} = \frac{2}{\omega_0 \tau} &= \frac{2v_g}{\omega_0 L}(1-\alpha) + \frac{v_g t_1^2}{\omega_0 L} + \frac{v_g t_2^2}{\omega_0 L} \\ &= \frac{1}{Q_i} + \frac{1}{Q_1} + \frac{1}{Q_2}, \end{aligned} \tag{2.26}$$

where Q_i is the intrinsic quality factor and Q_1 and Q_2 are external quality factors for cavity-waveguide coupling with the bus and receiver waveguides, respectively. Further, the quality factors are related to the lifetimes as $Q_i = \omega_0 \tau_i/2$, $Q_1 = \omega_0 \tau_1/2$, and $Q_2 = \omega_0 \tau_2/2$.

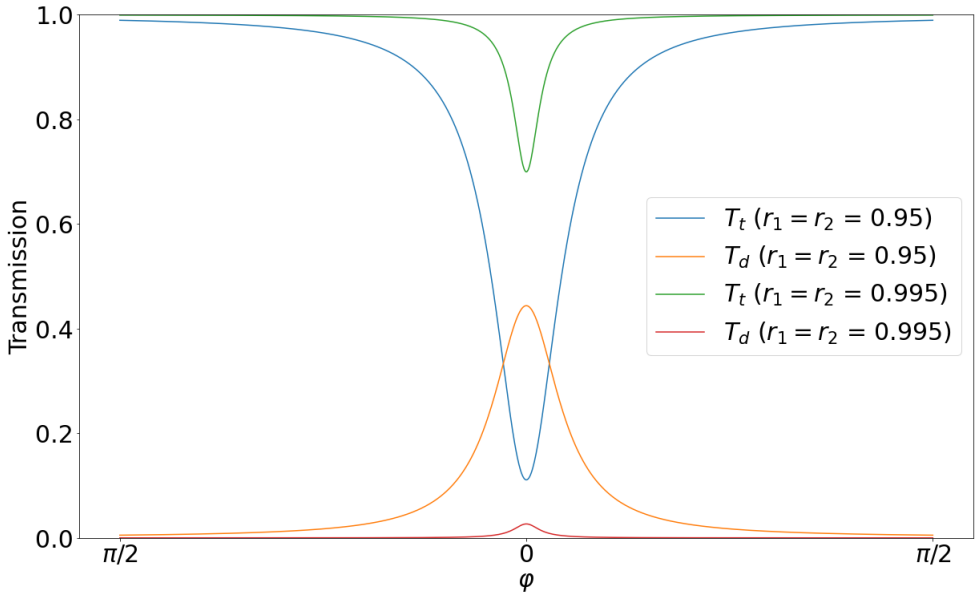


Figure 2.3: Transmission characteristics via through port (T_t) and drop port (T_d) for an add-drop ring resonator with $\alpha = 0.95$, and 2 cases—$r_1 = r_2 = 0.95$ and $r_1 = r_2 = 0.995$.

Lastly, the quality factor and finesse of a cavity are related to each other as $Q = \omega_0 \mathcal{F}/\omega_{FSR}$. Thus, the finesse for an add-drop ring resonator can be calculated to be

$$\mathcal{F} = \frac{\omega_{FSR}}{\omega_0} Q = \frac{\pi\sqrt{r_1 r_2 \alpha}}{1 - r_1 r_2 \alpha} \tag{2.27}$$

Figure 2.3 shows plots for Eqs. (2.23) and (2.24) for a round-trip loss $\alpha = 0.95$ and reflectivities $r_1 = r_2 = 0.95$ and $r_1 = r_2 = 0.995$, the latter case being pertinent to us as we will experimentally work with 99:1 beam splitters.

2.3 Experimental Results

2.3.1 Cavity Resonance

Following the theory from the previous sub-section, we can now proceed to build a basic add-drop all-optical fiber ring resonator with just two 2x2 99:1 couplers. As pointed out earlier, we will inject a laser light through one of the 99% ports in the cavity. The laser

is a cw Rio Orion Laser Module with a center wavelength of 1542.149 nm and a linewidth of 1.8 kHz with peak power of 12 mW. The laser output frequency will be swept by an Arbitrary Function Generator (AFG) by a 1 V_{pp}, 100 Hz ramp function. For a 100 Hz ramp, the laser frequency will be swept at a rate of 106.125 MHz/V over 5 ms if we only account for the rising edge of the ramp.

The circumference of the ring with just the two beam-splitters is $L = 3.64$ m. This corresponds to a free-spectral range of $\omega_{FSR} = 2\pi c/n_g L = 2\pi \cdot 56.96$ MHz. The FSR was calculated only using the circumference of the ring using the component lengths from spec sheets. Although this is a low precision method, we avoided using other methods. For example, as stated in Chapter 1 and can be seen theoretically in Figures 1.2 and 1.3, the FSR can be determined by looking at the frequency separation between consecutive modes. This can be done by providing a maximum of 4 V_{pp} ramp and sweeping the laser frequency up to 424.5 MHz to observe several resonances. But, and as we will see in Section 2.2.2, the fiber-optic ring causes a thermal drift. This caused a distortion and the consecutive resonance peaks were not observed to be equidistant from each other.

Additionally, since the polarization of light rotates every round trip, we also inserted a Thorlabs' 3-paddle polarization controller (with 56 mm diameter) to maintain a single polarization of light inside the cavity. In the next section, where we will add the EOM to the ring, the polarization controller will also be needed to match the single polarization to the principal axis of the Lithium-Niobate crystal.

The through port and drop port outputs were fed to fast 5 GHz InGaAs photodiodes (Thorlabs DET08CFC). According to the datasheets, both InGaAs photodiodes have a responsivity of $\mathcal{R} = 0.9$ A/W at 1550 nm. Subsequently, the photodiode data was fed to a 4-channel Stanford Research Systems SR445A RF preamplifier via a 50 Ω coaxial cable. Each channel of the amplifier has a gain of 5(V/V). The channels of the amplifier can also be cascaded to give a total gain of $5^4 = 625$(V/V). We mostly took data from the drop port as the through port output was modulated by the ramp input from the AFG to the laser which made it harder to do data processing at later stages. Thus, the through port was terminated by a terminator, and the drop port output was fed to two cascading channels on the amplifier for a total gain of 25(V/V). The amplifier output was finally observed on a 8 GHz Keysight oscilloscope (DSOS404A) and recorded on a computer through VISA commands in Igor Pro.

Without the cavity, a simple 12 mW laser input was fed through a 10 dB attenuator to the photodiode and subsequently the voltage was measured on the scope. The attenuator was needed as high laser power heats up the electronics of the photodiode causing the voltage on the scope to continuously drop over time. The power after the attenuator was

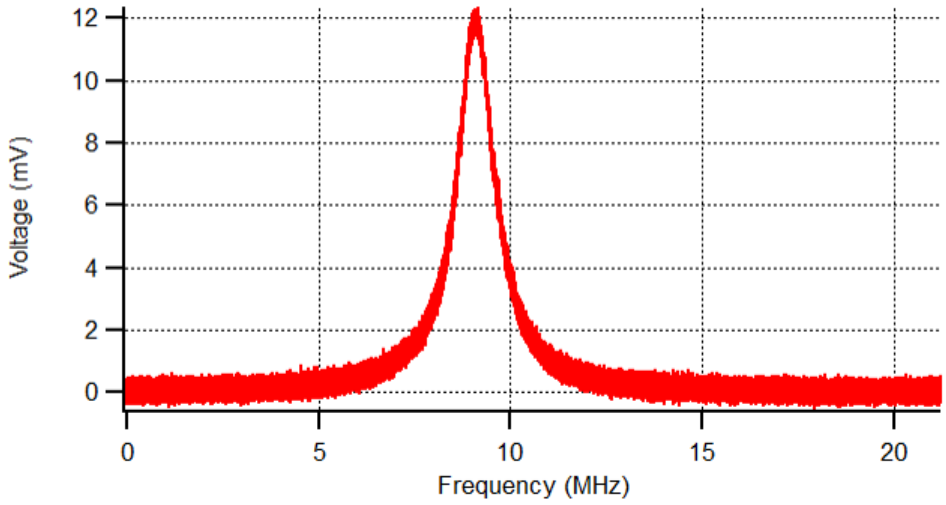


Figure 2.4: A single ring resonance for an add-drop ring made with just 99:1 beam-splitters.

measured to be 1.1 mW and the total voltage observed was 60.2 mV. Using the photodiode transfer function and Ohm's Law, we get a simple relation for the observed voltage to be $V = I \cdot Z = \mathcal{R}PZ$. For a 60.2 mV observed voltage, 1.1 mW of attenuated laser power, and an impedance of 50 Ω, the observed reponsivity of the photodiode is $\mathcal{R}_{\text{obs}} = V/PZ = 1.095$ A/W at 1550 nm. Further, using this value of responsivity, we can calculate the maximum voltage for the full 12 mW laser input to be $V_{\text{laser}} = \mathcal{R}_{\text{obs}}PZ = 657$ mV.

Figure 2.4 shows a typical cavity response for the ring resonator composed of just two fiber beam-splitters collected at its drop port. The figure shows scope voltage plotted against frequency. The frequency axis can easily be determined via the laser frequency sweep by setting the $\omega = 0$ at the minima of every period of the linear ramp. The peak voltage observed was 308.9 mV. It is important to note that this result includes a gain of 25(V/V) from the RF pre-amplifier. Thus, the result was divided by 25, and the peak voltage was measured to be $V_{\text{max}} = 12.356$ mV. This was done as we did not use a RF amplifier for just the laser input. Further, the steady-state transmission of the cavity was measured to be $T = V_{\text{max}}/V_{\text{laser}} = 0.019$ corresponding to a single-pass amplitude transmission of $\alpha = 0.94$. The low single-pass transmission could be attributed to the fact that the cavity has several bend losses as the circumference is 3.64 m, and to the fact that we are using 99:1 beam-splitters.

We can also now figure out the linewidth (full-width at half-maxima). Fitting the curve to a Lorentzian gives us a linewidth of $\Delta\nu_{FWHM} = 1.2\ MHz$. Since we are working at

1550 nm, the central frequency is $\nu_0 = 194.4$ THz. This allows us to calculate the quality factor of the resonator given by $Q = \nu_0/\Delta\nu_{FWHM}$. For the above values, $Q = 1.6 \times 10^8$.

Lastly, we can also calculate the signal-to-noise ratio (SNR). The SNR (in dB) of a signal is the ratio of the maximum height of the signal and the standard deviation of its noise profile on a logarithmic scale. We smoothed the signal via a 300 point running average and subtracted it from the original data to get its noise profile. The standard deviation of the noise was found to be $\Delta V = 0.1$ mV. Thus, the output signal has a SNR $= 20 \log_{10}(V_{\max}/\Delta V) = 39.8$ dB.

2.3.2 Drift Calculation

During our analysis of the fiber-optic ring resonator, we discovered that the cavity resonances drifted on the scope. This drift was primarily caused by the thermal effects in the fiber-optic ring. As the light propagates inside the ring, the silica fiber heats up. This temperature change modulated the phase of the cavity signal and the resonance peak consistently drifted from its position. This can pose concerns with regards to data acquisition and signal processing. Thus, we conducted an experiment to understand the drift better.

To quantify the drift, we first increased our scope acquisition to 500 ms to accommodate for 50 periods of the ramp. Every period of the ramp had a rising and a falling edge. For every rising and falling edge, we recorded the position of the cavity resonance with respect to the nearest ramp minima. The position denotes the frequency corresponding to the cavity resonance (in MHz). These frequency positions have been plotted against scope acquisition time as can be seen in Figures 2.5 and 2.6. The graph of the Frequency vs Time was a straight line with its slope corresponding to the thermal drift caused by the fiber-optic cavity. We performed the experiment for three different ramp amplitudes—0.6 V_{pp}, 0.8 V_{pp}, and 1.0 V_{pp} with average drifts 1.145 MHz/s, 1.56 MHz/s, and 3.545 MHz/s, respectively. The averages were done over the rising and falling edges of the ramp.

Notice that these thermal drifts are in the range of MHz/s. In comparison, the laser drift is around a few kHz/s as per the available information of the laser. Thus, most of the drift is caused by the fiber-optic cavity alone. Although, these numbers indicate that the thermal drift is huge, and they do pose a hindrance for the purposes of signal acquisition and processing, compared to the central frequency of 194.4 THz, the number is still fairly acceptable. Lastly, please note that the thermal drift is not correlated with the slew rate of the laser despite the fact that the drift decreases with decreasing ramp amplitude. In other words, the correlation may not be reproducible.

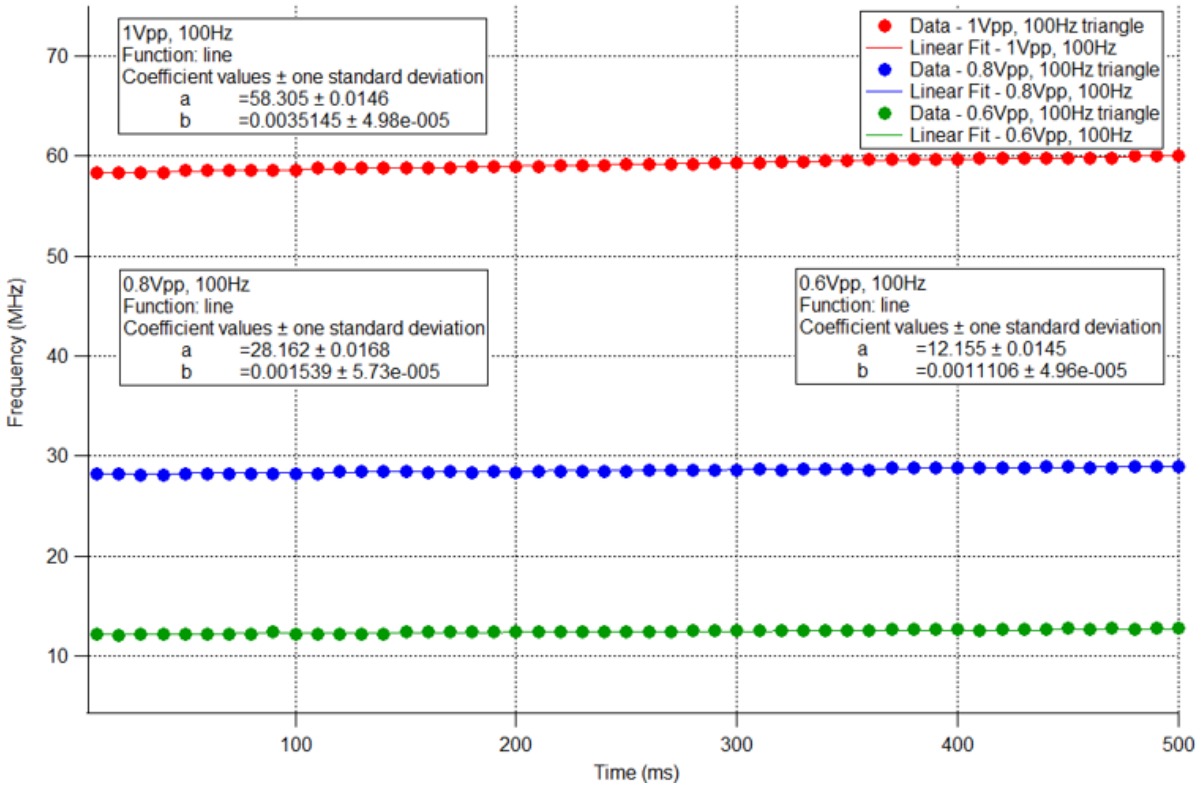


Figure 2.5: Thermal Drift for rising edge of the ramp with slopes 0.00111 ($0.6V_{\text{pp}}$), 0.00153 ($0.8V_{\text{pp}}$), and 0.00351 ($1.0V_{\text{pp}}$), and drifts 1.11 MHz/s, 1.53 MHz/s, 3.51 MHz/s, respectively.

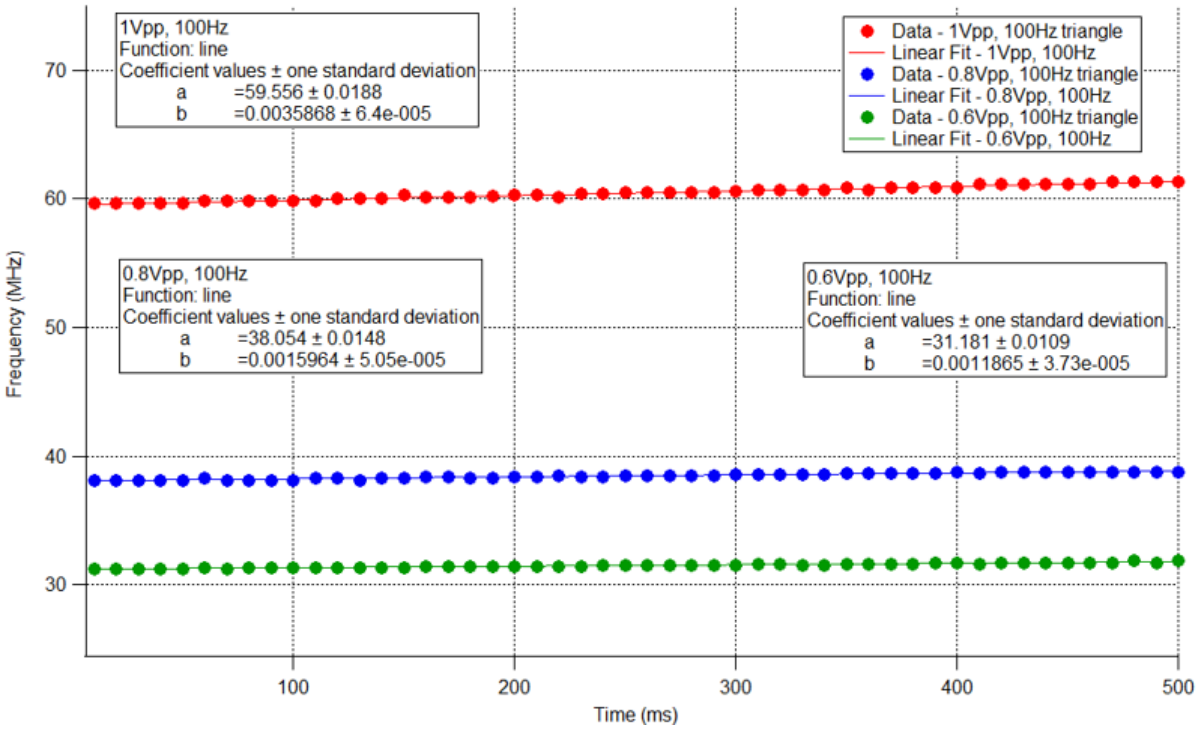


Figure 2.6: Thermal Drift for falling edge of the ramp with slopes 0.00118 ($0.6V_{\text{pp}}$), 0.00159 ($0.8V_{\text{pp}}$), and 0.00358 ($1.0V_{\text{pp}}$), and drifts 1.18 MHz/s, 1.59 MHz/s, 3.58 MHz/s, respectively.

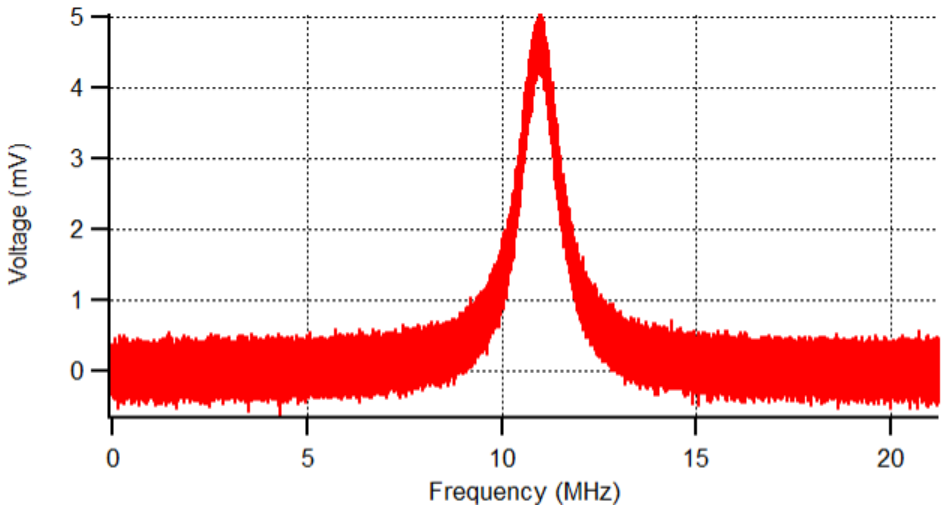


Figure 2.7: A single ring resonance for an add-drop ring made with just 99:1 beam-splitters and a DWDM filter.

2.4 Modified Ring Resonator

As mentioned earlier in the chapter, the essential ingredient is a Lithium-Niobate electro-optic modulator to measure the band structure in time. Unfortunately, the EOM has a massive insertion loss which lowers the power inside the cavity by half. This is in addition to the fact that only 1% of the signal enters the cavity in the first place. Thus, there is a need to amplify the signal with a gain medium like a Booster Optical Amplifier. But the optical amplifier adds Amplified Spontaneous Emission (ASE) noise. To overcome this noise, we added a Dense-Wavelength Division Multiplexer. The DWDM filtered most of the noise outside a 100 GHz bandwidth. In this section, we will add the DWDM and EOM one-by-one and study how the signal changes and why the optical amplifier is needed.

We first added the DWDM filter. We used a Fiberdyne 100 GHz DWDM with a 0.26 dB insertion loss at the pass channel. Adding the filter increased the rings' circumference to 6.16 m and thereby decreased the FSR to $\omega_{FSR} = 2\pi \cdot 33.66$ MHz. The cavity response showing a single resonance is in Figure 2.7. Again, to calculate the steady-state transmission, this result was achieved by dividing the original data by 25, the gain added by the RF amplifier. Thus, the maximum voltage observed on the scope is $V_{\max} = 5.052$ mV and the steady-state transmission $T = V_{\max}/V_{\text{laser}} = 7.7 \times 10^{-3}$ which corresponds to a single-pass transmission amplitude of $\alpha = 0.9$. Further, adding a lossy component increased the linewidth of the cavity to $\Delta\nu_{FWHM} = 1.2$ MHz, giving us a quality factor $Q = 1.58 \times 10^8$.

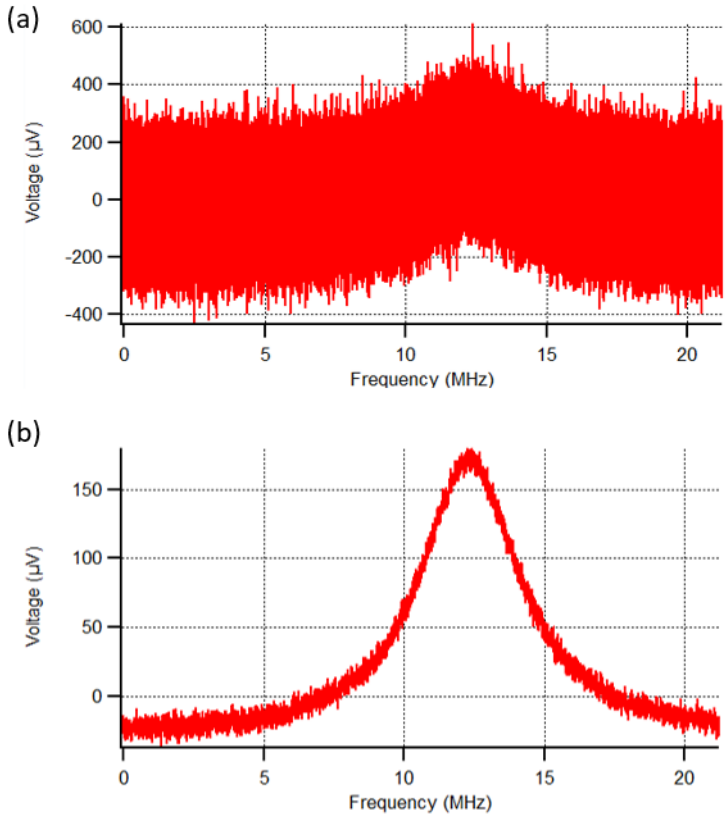


Figure 2.8: A single (a) noisy ring resonance and (b) averaged ring resonance for an add-drop ring made with just 99:1 beam-splitters, a DWDM filter, and an electro-optic modulator.

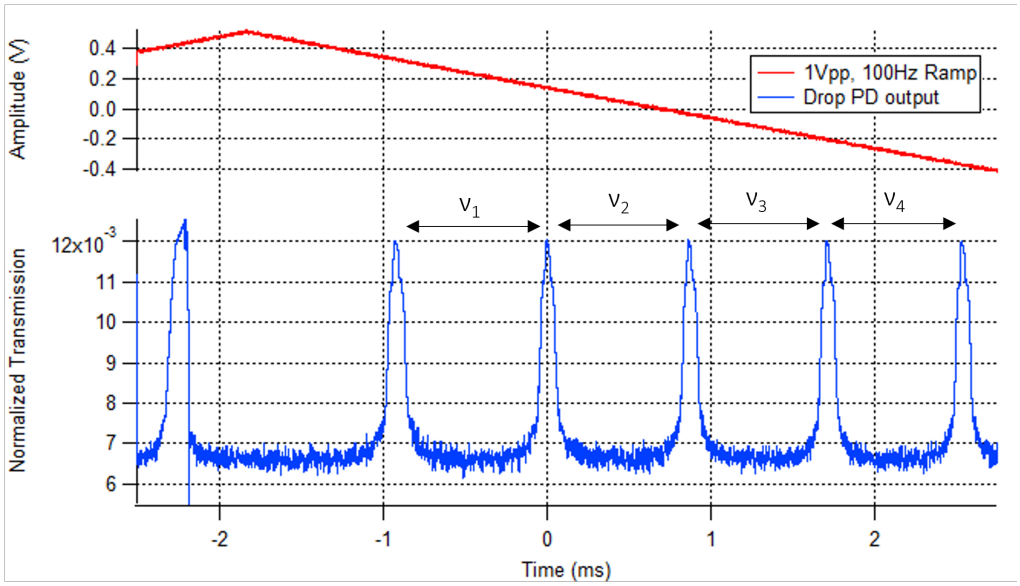
Lastly, the standard deviation of the noise profile is $\Delta V = 0.1$ mV, and the corresponding SNR has decreased to 32 dB.

Next, we added an Optilab 1550 nm EOM. The EOM consists of a Lithium-Niobate nonlinear crystal with a high insertion loss of 2.94 dB and a forward transmission bandwidth (S_{21}) of 9.3 GHz. It also has a half-wave voltage—the voltage needed to change the phase of the signal by π—of 11 V at 1 GHz RF input. If we add the EOM, the circumference of the ring increases to 8.695 m and the FSR decreases to $\omega_{FSR} = 2\pi \cdot 23.84$ MHz. As can be seen in Figure 2.8a, the EOM caused a significant signal loss and we are largely dominated by the thermal noise from the RF amplifier at the cavity output. To see the cavity response, we had to perform a 300 point moving average to obtain a cleaner signal as shown in Figure 2.8b. The maximum of the averaged signal is $V_{\max} = 179.53$ μV giving us

an incredibly low steady-state transmission of $T = V_{\max}/V_{\text{laser}} = 2.7 \times 10^{-4}$ and single-pass transmission amplitude of $\alpha = 0.5$. Further, the linewidth is $\Delta\nu_{FWHM} = 4.2$ MHz, and the cavity quality factor dropped to $Q = 4.6 \times 10^7$. Finally, the standard deviation of the noise profile, which mostly is a result of the thermal noise from the RF amplifier is $\Delta V = 89$ μV with a corresponding SNR of 6 dB.

Finally, we added a booster optical amplifier (BOA) to overcome the cavity losses caused by the EOM. Specifically, we used a Thorlabs' BOA1004P C-band amplifier with a 3 dB ASE bandwidth of 99 nm. The BOA increases the circumference of the ring to 11.755 m and consequently the theoretical FSR decreased to $\omega_{FSR} = 2\pi \cdot 17.279$ MHz. The cavity resonances can be seen in the blue curve in Figure 2.9a for a BOA gain of 19 dB. Given the high noise observed in Figure 2.8, the data was taken with a High Resolution Acquisition Mode directly on the oscilloscope before collecting it on the computer. As pointed out earlier, the resonance peaks are not equidistant and follow a quadratic dependence as can be seen with a quadratic fit in 2.9b. The crookedness of the ring resonances can be attributed to a combination of the ring's thermal drift and the oscilloscope's High Resolution Acquisition Mode. With a 19 dB gain, the steady-state transmission now increased to $T = 0.012$ and a single-pass transmission amplitude of $\alpha =$. The linewidth has also improved to $\Delta\nu_{FWHM} = 1.96$ MHz and the quality factor has more than doubled to $Q = 9.9 \times 10^7$. Note, the above linewidth is an average of all the four resonance peaks. Thus, given these results, it is very clear that the Booster Optical Amplifier provides an advantage to a hgihly lossy cavity.

(a)



(b)

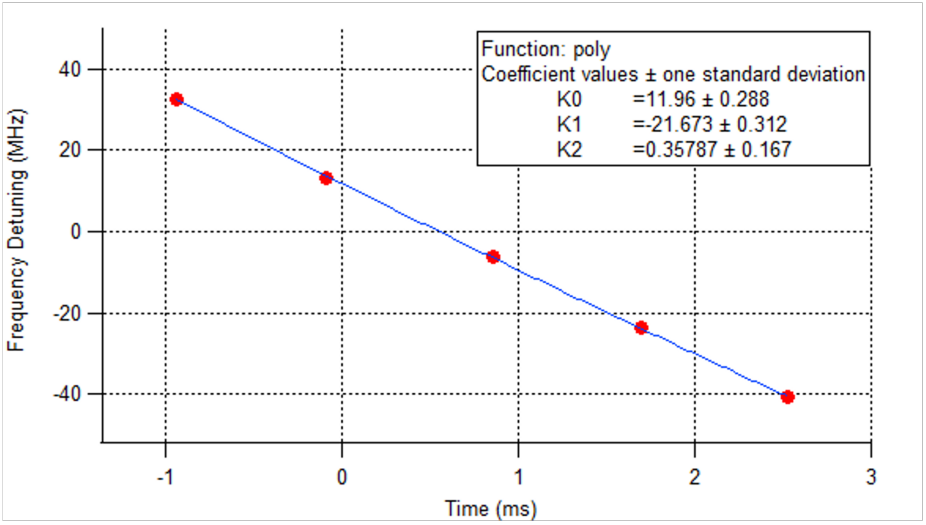


Figure 2.9: (a) Multiple ring resonances with the complete ring. The red curve is the ramp and the blue curve are the ring resonances under the falling edge of the ramp. The resonances were observed in High Resolution Acquisition Mode on the oscilloscope, and they are drifted from each other at frequencies $\nu_1 = 19.39$ MHz, $\nu_2 = 19.46$ MHz, $\nu_3 = 17.43$ MHz, and $\nu_4 = 16.99$ MHz. (b) The drifted ring resonances follow a quadratic dependence.

Chapter 3

Optical Simulation with a Fiber-Ring Resonator

Contributions

Bharat Kuchhal replicated the theory and experiment from *Nat Commun* **10**, 3122 (2019), performed all the algebraic and numerical calculations for the simulation of Figures 3.3, 3.6, 3.7, 3.8, and 3.9, constructed the experimental setup, took experimental results, and performed data analysis in Section 3.2.

Dr. Zheng Shi wrote Python scripts to emulate how Eqs. (3.54), (3.60), and (3.64) contribute to the simulations in Figures 3.3, 3.6, 3.7, 3.8, and 3.9.

3.1 Overview

Now that we have developed a CMT for an add-drop ring resonator and observed experimental results for a modified ring resonator, we can proceed to modulate the EOM inside the cavity with a sinusoid to couple the cavity modes and study topological phenomena.

We understand that a ring-resonator has equally spaced frequency modes separated by a Free-Spectral Range. In practice, there can be more than $\sim$2000 such frequency modes. This is reminiscent of atoms in a solid-state system periodically placed a lattice distant apart from each other in physical space. Typically, there are three such physical dimensions. For example, a CsCl crystal crystallizes in a simple cubic crystal structure, and NaCl

crystallizes in a face-centered cubic crystal structure[26]. But we need not restrict ourselves to three physical spatial dimensions. In relativity and high-energy physics, we often add a fourth temporal dimension and study the effects due to the richer topology. Physically, topology refers to the spatial connections of a geometrical system under continuous deformations [27]. In a similar fashion, we can tailor a lattice system with several higher dimensions with a lower order physical system. In this respect, equally distant frequency modes in a ring resonator give us an opportunity to investigate a synthetic dimension in frequency space [28][29][14].

Recall, in a solid-state system like NaCl, the atoms/ions oscillate about their mean positions. For this purpose, one can imagine the physics as an infinitely long chain of harmonic oscillators not only oscillating about their mean, but also coupled to each other via Coulomb interactions. Since position and momentum are conjugates of each other with a nonzero commutator, solutions to the Schrodinger's equation for a coupled harmonic oscillator system leads to discrete band structures in momentum space, sometimes even separated by band gaps. Given that every electromagnetic frequency mode in a ring resonator can be modeled as a harmonic oscillator, and frequency and time are also reciprocal to each other, we can expect band structures in time (or quasimomentum) space if we couple the equidistant frequency modes. The mode coupling can be achieved with an electro-optic modulator as can be seen in Figure 3.1. Thus, in this chapter, we will attempt at replicating the results published by Dutt et. al.[14] with a silica optical fiber ring resonator connected to a Lithium-Niobate electro-optic phase modulator. The EOM modulates the phase of the optical signal inside the cavity depending on the applied voltage. Specifically, we will explore how a sinusoidal modulation with frequency equal to the free-spectral range couples the frequency modes leading to band structures in the quasimomentum space both theoretically and experimentally. These energy band structures also happen to be solutions to the Floquet Hamiltonian. We will also explore theoretically that modulations of the form of a sum of sinusoids can even lead to asymmetric band structures.

3.2 Band Structure Measurements

In this section, we will excite the RF port of the EOM and modulate the phase of the cavity signal. We will start by solving Maxwell's equations to get an expression for an electric field in a 2D ring. From there, we will develop a coupled-mode theory and understand in detail how the cavity modes behave when modulated by a phase modulator. Typically, an EOM distributes energy into sidebands from the frequency mode. But when we modulate the EOM at the same sinusoidal frequency as the free-spectral range of the cavity, we will end

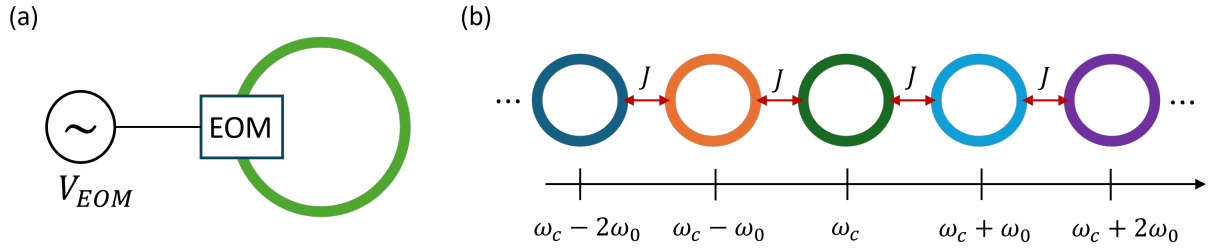


Figure 3.1: (a) A ring resonator dynamically modulated by an electro-optic modulator. (b) Different modes of the resonator coupled to each other. V_{EOM}: Modulation voltage, ω_c: Fundamental cavity mode, ω_0: Free spectral range, J: Nearest neighbor coupling constant

up coupling the frequency modes in much the same way as Coulomb interactions couple atoms in a solid-state lattice. In a solid-state structure where atoms are placed periodically in space, it is very well known that we get energy bands in the reciprocal (momentum) space. Similarly, if we couple periodically placed frequency modes in a resonator, we can expect to see energy bands in time, which is reciprocal to frequency. Once we develop this theory, we will look at some experimental results and observe how a Lithium-Niobate modulator in a all-optical fiber ring-resonator can help us achieve this goal.

3.2.1 Theory

In this section, we will consider a planar 2D ring and solve for Maxwell's equations for a portion of the ring's refractive index modulated by the Lithium-Niobate phase modulator. Then we will take a quantum coupled-mode theory approach and solve the time-dependent Schrodinger's equation to study Floquet energy bands. Note, this section has been taken from Dutt et. al.[14]

Coupled-Mode Equations

From Maxwell's equations, we know

$$\begin{aligned} \nabla \times \vec{E}(\vec{r},t) &= -\frac{\partial \vec{B}(\vec{r},t)}{\partial t} \\ \text{and} \quad |\vec{B}(\vec{r},t)| &= \mu_0 |\vec{H}(\vec{r},t)| = \frac{n|\vec{E}(\vec{r},t)|}{c} \end{aligned} \tag{3.1}$$

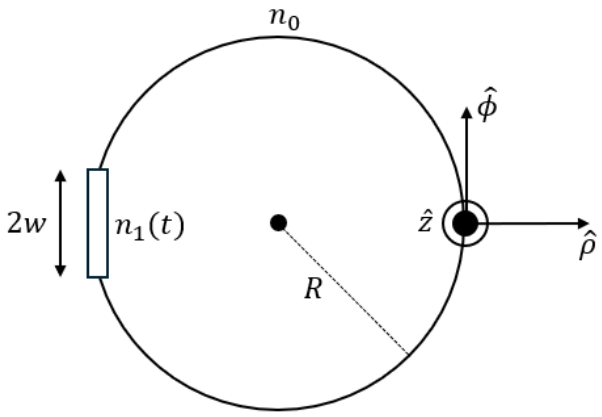


Figure 3.2: A simple ring resonator with an electro-optic modulator of width $2w$.

Here, μ_0 is permeability of free-space and c is the speed of light in vacuum. Since we will modulate the phase of the cavity with a RF field, the refractive index n will be a function of time and will depend on the electro-optic coefficient r and thickness d of the Lithium-Niobate crystal. Specifically, the refractive index will be $n = n_0 + n_1(t)$, where n_0 is the refractive index of silica optical fiber, and n_1 for a nonlinear $\chi^{(2)}$ material will be

$$n_1(t) = \frac{n_0^3 r}{2d} V_{\text{EOM}}(t), \tag{3.2}$$

where $V_{\text{EOM}}(t)$ is the modulation voltage applied to the RF port of the EOM. Notice, that $n_1(t)$ is also dependent on ϕ, the angular location of the EOM on the ring. We will make this more explicit shortly. We can also express $n_1(t)$ in terms of the half-wave voltage V_π, i.e., the voltage needed to change the phase by π as

$$n_1(t) = \frac{\lambda}{4w} \frac{V_{\text{EOM}}(t)}{V_\pi}, \tag{3.3}$$

where $V_\pi = \lambda d / 2wrn_0^3$ and λ is the wavelength.

We will work in a cylindrical coordinate system as shown in Figure 3.2 and recognize that since the propagation is along $\hat{\phi}$, we can solve for the magnetic field $\vec{B} = B_\rho(\phi, t)\hat{\rho}$ and the electric field will be $\vec{E} = E_z(\phi, t)\hat{z}$. Thus,

$$\nabla \times \vec{E} = \frac{1}{\rho}\frac{\partial E_z}{\partial \phi}\hat{\rho} - \frac{\partial E_z}{\partial \rho}\hat{\phi} = \frac{1}{R}\frac{\partial E_z(\phi, t)}{\partial \phi}\hat{\phi}, \tag{3.4}$$

where we realize ρ is a constant and simply equals the radius R.

If we now substitute Eq. (3.4) in Eq. (3.1), we get the relation

$$\begin{aligned}\frac{1}{R}\frac{\partial E_z}{\partial \phi} &= -\frac{\partial B_\rho}{\partial t} = -\frac{1}{c}\frac{\partial}{\partial t}\left[n(\phi,t)E_z\right] \\ &= -\frac{1}{c}\left[E_z\frac{\partial n}{\partial t} + n\frac{\partial E_z}{\partial t}\right]\end{aligned} \tag{3.5}$$

Recognizing that $e^{im\phi}$ forms a complete basis, we now choose a solution for the electric field as $E_z(\phi,t) \sim Ca(t)e^{im\phi}$. Here $a(t)$ is the mode amplitude and C is a constant of integration. Given that the solution to the differential equation will be a superposition of all the mode functions, we can now use the trial solution

$$E_z(\phi,t) = \sum_{m'} C_{m'}a_{m'}(t)e^{-im'\phi} + \text{c.c.} \tag{3.6}$$

where c.c. represents the complex conjugate. If we now substitute Eq. (3.6) in Eq. (3.5), we get

$$\begin{aligned}&\frac{1}{R}\frac{\partial}{\partial\phi}\sum_{m'} C_{m'}a_{m'}(t)e^{-im'\phi} = -\frac{1}{c}\left[\frac{\partial n}{\partial t}\sum_{m'} C_{m'}a_{m'}(t)e^{-im'\phi} + n\frac{\partial}{\partial t}\sum_{m'} C_m a_{m'}(t)e^{-im'\phi}\right] \\ \Rightarrow\ &\frac{1}{R}\sum_{m'} C_{m'}(-im')a_{m'}(t)e^{-im'\phi} = -\frac{1}{c}\sum_{m'} C_{m'}\left[\frac{\partial n(\phi,t)}{\partial t}a_{m'} + n(\phi,t)\frac{\mathrm{d}a_{m'}}{\mathrm{d}t}\right]e^{-im'\phi}\end{aligned} \tag{3.7}$$

We can now divide both sides by $n(\phi,t)$ and multiply and integrate both sides w.r.t. $\frac{1}{2\pi}\int_0^{2\pi} e^{im\phi}\mathrm{d}\phi$, we get

$$\begin{aligned}\frac{1}{2\pi R}\sum_{m'} im'C_{m'}a_{m'}(t)\int_0^{2\pi}\frac{e^{i(m-m')\phi}}{n(\phi,t)}\mathrm{d}\phi &= \frac{1}{c}\sum_{m'} C_{m'}\frac{\mathrm{d}a_{m'}}{\mathrm{d}t}\frac{1}{2\pi}\int_0^{2\pi} e^{i(m-m')\phi}\mathrm{d}\phi \\ &+\frac{1}{c}\sum_{m'} C_{m'}a_{m'}(t)\frac{1}{2\pi}\int_0^{2\pi}\frac{e^{i(m-m')\phi}}{n(\phi,t)}\frac{\partial n(\phi,t)}{\partial t}\mathrm{d}\phi\end{aligned} \tag{3.8}$$

But $\int_0^{2\pi} e^{i(m-m')\phi}\mathrm{d}\phi = 2\pi\cdot\delta(m-m')$. Thus, the first summation on the RHS of Eq. (3.8) simply becomes $C_m\dot{a}_m$. Thus, the above equation can be reduced to the form

$$\frac{\mathrm{d}}{\mathrm{d}t}a_m(t) = \sum_{m'}\left(i\alpha_{mm'} + \beta_{mm'}\right)a_{m'}(t), \tag{3.9}$$

where

$$\alpha_{mm'} = m' \frac{c}{L} \frac{C_{m'}}{C_m} \int_0^{2\pi} \frac{e^{i(m-m')\phi}}{n(\phi,t)} \mathrm{d}\phi \tag{3.10}$$

and

$$\beta_{mm'} = \frac{1}{2\pi} \frac{C_{m'}}{C_m} \int_0^{2\pi} \frac{e^{i(m-m')\phi}}{n(\phi,t)} \frac{\partial n}{\partial t} \mathrm{d}\phi \tag{3.11}$$

Here $L = 2\pi R$ is the circumference of the ring.

Since the effect of $\partial n/\partial t$ will be very small, we will ignore $\beta_{mm'}$ for the remainder of our calculations.

Notice that for the simplest case with no modulation ($V_{\mathrm{EOM}}(t) = 0$), $n = n_0 + n_1(t) = n_0$, and consequently

$$\begin{aligned} \sum_{m'} \alpha_{mm'} a_{m'}(t) &= \frac{c}{n_0 L} \sum_{m'} m' \frac{C_{m'}}{C_m} a_{m'}(t) \int_0^{2\pi} e^{i(m-m')\phi} \mathrm{d}\phi \\ &= \frac{c}{n_0 L} \sum_{m'} m' \frac{C_{m'}}{C_m} a_{m'}(t) 2\pi\delta(m-m') = m \frac{2\pi c}{n_0 L} a_m(t) \end{aligned} \tag{3.12}$$

Denoting the frequency of the m^{th} cavity mode as $\omega_m = m \times 2\pi\nu_m = m \times 2\pi \cdot c/n_0 L$, we can re-write Eq. (3.9) simply as

$$\frac{\mathrm{d}}{\mathrm{d}t} a_m(t) = i\alpha_{mm} a_m(t) = i\omega_m a_m(t) \tag{3.13}$$

Notice that the frequency spacing, or the free-spectral range, will be $\omega_{\mathrm{FSR}} = \omega_{m+1} - \omega_m = 2\pi \cdot c/n_0 L$, the same as we saw in Sec. (3.1) provided that the group-velocity dispersion inside the ring is negligible. Further, since the energy in the m^{th} mode is $\hbar\omega_m$, and since $|a_m|^2$ represents photon number flux, the coefficients will be $C_m = \sqrt{\hbar\omega_m/2\epsilon_0 n_0^2 L}$.

We now add the phase modulator to the ring. We will model the refractive index as a perturbation in the angular position ϕ:

$$n(\phi,t) = n_0 + n_1(t)\,\mathrm{rect}\left(\frac{\phi}{\phi_w}\right) \tag{3.14}$$

where $\phi_w = 2\pi \times 2w/L$ and rect(.) is the rectangular function. Therefore, from Eq. (3.10) we get

$$\alpha_{mm'} = m' \frac{c}{L} \frac{C_{m'}}{C_m} \int_0^{2\pi} \frac{e^{i(m-m')\phi}}{n_0 + n_1(t)\mathrm{rect}\left(\frac{\phi}{\phi_w}\right)} \mathrm{d}\phi \tag{3.15}$$

Assuming $|n_1(t)| << n_0$, $\forall\ t$, we can re-write the above equation as

$$\begin{aligned}\alpha_{mm'} &= m'\frac{c}{n_0 L}\frac{C_{m'}}{C_m}\int_0^{2\pi} e^{i(m-m')\phi}\left[1+\frac{n_1(t)}{n_0}\text{rect}\left(\frac{\phi}{\phi_w}\right)\right]^{-1}\mathrm{d}\phi \\ \Rightarrow \alpha_{mm'} &\approx m'\frac{c}{n_0 L}\frac{C_{m'}}{C_m}\int_0^{2\pi} e^{i(m-m')\phi}\left[1-\frac{n_1(t)}{n_0}\text{rect}\left(\frac{\phi}{\phi_w}\right)\right]\mathrm{d}\phi\end{aligned} \tag{3.16}$$

where we have used $L = 2\pi R$ and the approximation $(1+x)^n \approx 1 + nx$ for small x and $n = -1$.

Further, notice that

$$\frac{C_{m'}}{C_m} = \sqrt{\frac{\omega_{m'}}{\omega_m}} = \sqrt{\frac{m'}{m}} \tag{3.17}$$

and

$$\begin{aligned}\int_0^{2\pi} e^{i(m-m')\phi}\text{rect}\left(\frac{\phi}{\phi_w}\right)\mathrm{d}\phi &= \int_{-\phi_w/2}^{\phi_w/2} e^{i(m-m')\phi}\mathrm{d}\phi \\ &= \frac{e^{i(m-m')\phi_w/2} - e^{-i(m-m')\phi_w/2}}{i(m-m')} \\ &= \frac{2\sin[(m-m')\phi_w/2]}{(m-m')} \\ &= \phi_w\,\text{sinc}[(m-m')\phi_w/2]\end{aligned} \tag{3.18}$$

If we substitute these along with $\int_0^{2\pi} e^{i(m-m')\phi}\mathrm{d}\phi = 2\pi\cdot\delta(m-m')$ in Eq. (3.15), we can now get an expression for $\alpha_{mm'}$ as

$$\alpha_{mm'} \approx m'\frac{c}{n_0 L}\sqrt{\frac{m'}{m}}\left[2\pi\delta(m-m') - \frac{n_1(t)}{n_0}\phi_w\,\text{sinc}\left[(m-m')\frac{\phi_w}{2}\right]\right] \tag{3.19}$$

Thus, for the case with modulation $V_{\text{EOM}}(t) \neq 0$, we can now get the summation

$$\sum_{m'}\alpha_{mm'}a_{m'}(t) \approx 2\pi m\frac{c}{n_0 L} - \frac{n_1(t)}{n_0}\phi_w\frac{c}{n_0 L}\sum_{m'} m'\sqrt{\frac{m'}{m}}\,\text{sinc}\left[(m-m')\frac{\phi_w}{2}\right] \tag{3.20}$$

But $c/n_0 L = \omega_{\text{FSR}}$, $\omega_m = m\omega_{\text{FSR}}$ and $\phi_w = 2\pi \times 2w/L$. Therefore, the equation of motion for the mode amplitude $a_m(t)$ reduces to

$$\begin{aligned}\frac{\mathrm{d}a_m}{\mathrm{d}t} &= i\sum_{m'}\alpha_{mm'}a_{m'}(t) \\ &\approx i\omega_m a_m(t) - i\omega_{\text{FSR}}\frac{n_1(t)}{n_0}\frac{2w}{L}\sum_{m'} m'\sqrt{\frac{m'}{m}}\,\text{sinc}\left[2\pi(m-m')\frac{w}{L}\right]a_{m'}(t)\end{aligned} \tag{3.21}$$

We are now in a position to define the mode couplings $J_{m-m'}(t)$ between modes m and m' as

$$J_{m-m'}(t) = -\omega_{\text{FSR}} \frac{n_1(t)}{n_0} \frac{2w}{L} m' \sqrt{\frac{m'}{m}} \operatorname{sinc}\left[2\pi(m-m')\frac{w}{L}\right] \tag{3.22}$$

Notice that compared to the central mode m_0 near 194 THz (or 1550 nm), $|m_0 - m|$ and $|m_0 - m'|$ will be very small. Thus, $m' \approx m$ giving us $\sqrt{m'/m} \approx 1$, and $m'\omega_{\text{FSR}} \approx \omega_{m_0}$. Further, substituting Eq. (3.3) now gives us

$$\begin{aligned} J_{m_0-m}(t) &\approx -\omega_{m_0} \frac{2w}{n_0 L} \frac{\lambda_{m_0}}{4w} \operatorname{sinc}\left[2\pi(m_0-m)\frac{w}{L}\right] \frac{V_{\text{EOM}}(t)}{V_\pi} \\ &= -\frac{2\pi\lambda_{m_0}\nu_{m_0}}{2n_0 L} \operatorname{sinc}\left[2\pi(m_0-m)\frac{w}{L}\right] \frac{V_{\text{EOM}}(t)}{V_\pi} \\ &= -\frac{\pi c}{n_0 L} \operatorname{sinc}\left[2\pi(m_0-m)\frac{w}{L}\right] \frac{V_{\text{EOM}}(t)}{V_\pi} \\ &= -\frac{\omega_{\text{FSR}}}{2} \operatorname{sinc}\left[2\pi(m_0-m)\frac{w}{L}\right] \frac{V_{\text{EOM}}(t)}{V_\pi} \end{aligned} \tag{3.23}$$

And the simplified equation of motion will now be

$$\frac{\mathrm{d}a_m}{\mathrm{d}t} = i\omega_m a_m(t) + i\sum_{m'} J_{m_0-m'}(t) a_{m'}(t) \tag{3.24}$$

An interesting thing to notice that the coupling is definitely dependent on the modulation voltage $V_{\text{EOM}}(t)$, but not the form or periodicity of the voltage function. Also notice that the the couplings are related to the difference $(m_0 - m)$ and not the individual modes themselves. As we will see shortly, this will allow our Hamiltonian to be translationally invariant in the frequency space.

Floquet Modes

Now that we have developed a coupled-mode theory for the modes of a ring-resonator modulated by a phase modulator, we will take a quantum mechanical approach, construct a time-periodic Floquet Hamiltonian, and solve for the eigenstates and eigenergies. To introduce coupling in the ring, we will modulate the EOM with a sinusoidal of frequency $\omega_{\text{EOM}} = \omega_{\text{FSR}} = \omega_0$, i.e., we will choose $V_{\text{EOM}}(t) = V_0 \cos\omega_0 t$. Notice, the couplings are now time-periodic, i.e., $J_{n-m}(t) = J_{n-m}(t + T_0)$, where $T_0 = 2\pi/\omega_0$.

Going over to a rotating frame, we will now let $b_m(t) = a_m(t)e^{-im\omega_0 t}$. And consequently,

$$\frac{\mathrm{d}b_m}{\mathrm{d}t} = \left[\frac{\mathrm{d}a_m}{\mathrm{d}t} - im\omega_0 a_m(t)\right] e^{-im\omega_0 t} \tag{3.25}$$

Substituting from Eq. (3.24), we get

$$\begin{aligned}\frac{\mathrm{d}b_m}{\mathrm{d}t} &= \left[i\omega_m a_m(t) + i\sum_n J_{n-m}(t)a_n(t) - im\omega_0 a_m(t)\right] e^{-im\omega_0 t} \\ &= i\sum_n J_{n-m}(t)b_n(t)e^{i(n-m)\omega_0 t} \\ \Rightarrow i\frac{\mathrm{d}b_m}{\mathrm{d}t} &= -\sum_n J_{n-m}(t)b_n(t)e^{i(n-m)\omega_0 t}\end{aligned} \tag{3.26}$$

where we have used the fact that $\omega_m = m\omega_0$ to cancel the first and third terms in the rectangular brackets.

Let the ket vector

$$|b\rangle = (..., b_{m-1}, b_m, b_{m+1}, ...)^T = \sum_m b_m |m\rangle \tag{3.27}$$

Here, $|m\rangle$ represents the m^{th} mode of an unmodulated cavity. The cavity modes satisfy our usual properties of orthonormality ($\langle m|n\rangle = \delta_{mn}$) and completeness ($\sum_m |m\rangle \langle m| = \mathbb{1}$). Further, we can define Hamiltonian matrix elements as $H_{mn}(t) = \langle m|H(t)|n\rangle = -J_{n-m}e^{i(n-m)\omega_0 t}$. Therefore, we can now re-write Eq. (3.26) as

$$i\frac{\mathrm{d}}{\mathrm{d}t}|b\rangle = H(t)|b\rangle \tag{3.28}$$

This is nothing but the Schrodinger's equation for the cavity modes $|b\rangle$.

As pointed out earlier, $J_{n-m}(t) = J_{n-m}(t+T_0)$. Thus, $H(t) = H(t+T_0)$ and the Hamiltonian has a time-translation symmetry. Further, the Hamiltonian is also translationally symmetric in the discrete frequency space as $H_{mn}(t) \propto J_{n-m} \propto \mathrm{sinc}\,[2\pi(n-m)w/L]$. In other words, $H_{mn}(t)$ is dependent on the difference of the mode indices $(m-n)$. These allow us to to define conserved Bloch quasi-momentum k in the reciprocal time space and Floquet energy bands in the time interval $[-\omega_0/2, \omega_0/2]$. We also define Bloch modes in the quasi-momentum space as

$$|k\rangle = \sum_m e^{-im\omega_0 k}|m\rangle \tag{3.29}$$

We can check that these Bloch modes in the quasi-momentum space are also orthogonal as

$$\begin{aligned}\langle k|k'\rangle &= \sum_m \sum_n e^{im\omega_0 k} e^{-in\omega_0 k'} \langle m|n\rangle \\ &= \sum_m \sum_n e^{im\omega_0 k} e^{-in\omega_0 k'} \delta_{mn} \\ &= \sum_m e^{im\omega_0 (k-k')} = \frac{2\pi}{\omega_0}\delta(k-k')\end{aligned} \tag{3.30}$$

and complete as

$$\begin{aligned}\int_{-\pi/\omega_0}^{\pi/\omega_0} \mathrm{d}k\, |k\rangle \langle k| &= \int_{-\pi/\omega_0}^{\pi/\omega_0} \mathrm{d}k \sum_m \sum_n e^{-im\omega_0 k} e^{in\omega_0 k} |m\rangle \langle n| \\ &= \sum_m \sum_n |m\rangle \langle n| \int_{-\pi/\omega_0}^{\pi/\omega_0} e^{-i(m-n)\omega_0 k} \mathrm{d}k \\ &= \frac{2\pi}{\omega_0} \sum_m \sum_n |m\rangle \langle n| \, \delta(m-n) \\ &= \frac{2\pi}{\omega_0} |m\rangle \langle m| = \frac{2\pi}{\omega_0} \mathbb{1} \\ \Rightarrow \ \frac{\omega_0}{2\pi} \int_{-\pi/\omega_0}^{\pi/\omega_0} \mathrm{d}k\, |k\rangle \langle k| &= \mathbb{1}\end{aligned} \tag{3.31}$$

Thus, we can now write $|b\rangle$ in the quasi-momentum space as

$$|b\rangle = \frac{\omega_0}{2\pi} \int_{-\pi/\omega_0}^{\pi/\omega_0} \mathrm{d}k \tilde{b}_k |k\rangle \,, \tag{3.32}$$

where $\tilde{b}_k$ are the Fourier amplitudes. Comparing it to $|b\rangle = \sum_m b_m |m\rangle$, we get

$$\begin{aligned} b_m &= \frac{\omega_0}{2\pi} \int_{-\pi/\omega_0}^{\pi/\omega_0} \tilde{b}_k e^{-im\omega_0 k} \mathrm{d}k \\ \iff \tilde{b}_k &= \sum_m b_m e^{im\omega_0 k} = \langle k|b\rangle \end{aligned} \tag{3.33}$$

Taking the time-derivative of b_m and inserting it into Eq. (3.26), we now get

$$\begin{aligned} i\frac{\mathrm{d}b_m}{\mathrm{d}t} &= i\frac{\omega_0}{2\pi}\int_{-\pi/\omega_0}^{\pi/\omega_0}\frac{\mathrm{d}\tilde{b}_k}{\mathrm{d}t}e^{-im\omega_0 k}\mathrm{d}k \\ &= -\sum_n J_{n-m}(t)\left[\frac{\omega_0}{2\pi}\int_{-\pi/\omega_0}^{\pi/\omega_0}\tilde{b}_k e^{-in\omega_0 k}\mathrm{d}k\right]e^{i(n-m)\omega_0 t} \\ \Rightarrow\ i\int_{-\pi/\omega_0}^{\pi/\omega_0}\frac{\mathrm{d}\tilde{b}_k}{\mathrm{d}t}e^{-im\omega_0 k}\mathrm{d}k &= -\int_{-\pi/\omega_0}^{\pi/\omega_0}\left[\sum_n J_{n-m}(t)e^{-in\omega_0 k}e^{i(n-m)\omega_0 t}\tilde{b}_k\right]\mathrm{d}k \end{aligned} \tag{3.34}$$

This is possible if and only if the integrands on both sides of the equation are equal. Thus,

$$\begin{aligned} i\frac{\mathrm{d}\tilde{b}_k}{\mathrm{d}t}e^{-im\omega_0 k} &= -\sum_n J_{n-m}(t)e^{-in\omega_0 k}e^{i(n-m)\omega_0 t}\tilde{b}_k \\ \Rightarrow\ i\frac{\mathrm{d}\tilde{b}_k}{\mathrm{d}t} &= -\sum_n J_{n-m}(t)e^{-i(n-m)\omega_0 k}e^{i(n-m)\omega_0 t}\tilde{b}_k \end{aligned} \tag{3.35}$$

Changing the summation variable to $q = (n-m)$, we can simply re-write the above equation as

$$i\frac{\mathrm{d}\tilde{b}_k}{\mathrm{d}t} = -\sum_q J_q(t)e^{-iq\omega_0(k-t)}\tilde{b}_k \tag{3.36}$$

As before, we can now define our new Hamiltonian in the quasi-momentum space as

$$H_k(t) = -\sum_q J_q(t)e^{-iq\omega_0(k-t)}, \quad \forall q \in \mathbb{Z} \tag{3.37}$$

and re-write the Schrodinger's equation as

$$i\frac{\mathrm{d}\tilde{b}_k}{\mathrm{d}t} = H_k(t)\tilde{b}_k \tag{3.38}$$

We can also find the relation between $H(t)$ and $H_k(t)$ by looking at the $k-k^{\text{th}}$ matrix

element of the Hamiltonian, i.e.,

$$\begin{aligned}\langle k|H(t)|k'\rangle &= \sum_m \sum_n e^{im\omega_0 k} \langle m|H(t)|n\rangle e^{-in\omega_0 k'} \\ &= -\sum_m \sum_n J_{n-m}(t) e^{i(n-m)\omega_0 t} e^{im\omega_0 k} e^{-in\omega_0 k'} \\ &= -\sum_m \sum_n J_{n-m}(t) e^{i(n-m)\omega_0 t} e^{i(m-n)\omega_0 k} e^{in\omega_0(k-k')} \\ &= -\delta(k-k') \sum_q J_q(t) e^{iq\omega_0(t-k)} = \delta(k-k') H_k(t)\end{aligned} \tag{3.39}$$

where again we changed summation variable to $q = n - m$. Additionally, this also allows us to solve for $\langle k|H(t)|b\rangle$ as

$$\begin{aligned}\langle k|H(t)|b\rangle &= \frac{\omega_0}{2\pi} \int_{-\pi/\omega_0}^{\pi/\omega_0} \tilde{b}_{k'} \langle k|H(t)|k'\rangle \, \mathrm{d}k' \\ &= \frac{\omega_0}{2\pi} \int_{-\pi/\omega_0}^{\pi/\omega_0} \tilde{b}_{k'} \delta(k-k') H_k(t) \mathrm{d}k' = H_k(t) \tilde{b}_k\end{aligned} \tag{3.40}$$

From Eq. (3.37), we can see that the Hamiltonian is diagonal in k-space, $\forall\ t$. Such a definition allows us to study the Floquet Hamiltonian

$$(H_k(t) - i\partial_t)\psi_{kn}(t) = \varepsilon_{k,n}\psi_{kn}(t) \tag{3.41}$$

with $\psi_{kn}(t)$ as the eigenstates and $\varepsilon_{k,n}$ as the corresponding eigenenergies of the Floquet Hamiltonian $(H_k(t) - i\partial_t)$ with the properties that the eigenstates are also time-periodic with period T_0 and the eigenenergies satisfy $\varepsilon_{k,n} = \varepsilon_k + n\omega_0$, $\forall\ n \in \mathbb{Z}$. Here, the labels k represent the quasimomentum value corresponding to the eigenvalue and eigenstate. And n represents the band label.

Band Structure in Time

It is important to note that the above analysis was for a closed-system. We will now drive our cavity externally with amplitudes $|s^+\rangle = s^+ \sum_m e^{-im\omega_0 t} |m\rangle$ and modify our coupled-mode equations for an open system to obtain a theoretical solution for the steady-state transmission for the band structure. Thus, our cavity modes in Eq. (3.26) can now be re-written as

$$\frac{\mathrm{d}b_m}{\mathrm{d}t} = i \sum_q J_q(t) b_{m+q}(t) e^{is\omega_0 t} - \kappa b_m + i\sqrt{\kappa} e^{-i(\omega + m\omega_0)t} s^+ \tag{3.42}$$

Here, the first term, as before, is due to the modes coupling to each other in the ring-resonator. The second term is a result of losses, both internal within the cavity and externally to bus waveguides via the beam-splitters with a loss-rate κ. Since κ denotes cavity losses, it will also determine the linewidth of cavity resonances for an unmodulated cavity. And the third term is a result of the cavity being driven from an external monochromatic source like a laser with amplitude s^+ and frequency ω.

Given that we have only talked about cavity modes, we still need an expression for the cavity output. Since the cavity output is a result of all the modes prevalent within the cavity, we can simply write

$$s_d^- = i\sqrt{\kappa}\sum_m b_m(t)e^{im\omega_0 t} = i\sqrt{\kappa}\tilde{b}_k(t)|_{k=t} \tag{3.43}$$

where we have used Eq. (3.35). Eqs. (3.42) and (3.43) collectively form the coupled-mode equations for a cavity modulated by a phase-modulator and externally coupled to waveguides.

Just as in Eq. (3.28), we can re-write Eq. (3.42) more compactly as

$$i\frac{\mathrm{d}}{\mathrm{d}t}\left|b(t)\right\rangle = \left(-i\kappa + H(t)\right)\left|b(t)\right\rangle - \sqrt{\kappa}e^{-i\omega t}\left|s^+\right\rangle \tag{3.44}$$

To solve Eq. (3.44), we can consider a steady-state time-periodic solution

$$\left|b(t)\right\rangle = e^{-i\omega t}\left|b'(t)\right\rangle, \text{ where } \left|b'(t)\right\rangle = \left|b'(t+T_0)\right\rangle \tag{3.45}$$

Substituting Eq. (3.45) in Eq. (3.44), we get

$$\begin{aligned} i\left[-i\omega\left|b'\right\rangle + \frac{\mathrm{d}}{\mathrm{d}t}\left|b'\right\rangle\right]e^{-i\omega t} &= \left(-i\kappa + H(t)\right)e^{-i\omega t}\left|b'\right\rangle - \sqrt{\kappa}e^{-i\omega t}\left|s^+\right\rangle \\ \Rightarrow\ \omega\left|b'\right\rangle + i\frac{\mathrm{d}}{\mathrm{d}t}\left|b'\right\rangle &= \left(-i\kappa + H(t)\right)\left|b'\right\rangle - \sqrt{\kappa}\left|s^+\right\rangle \\ \Rightarrow \left[\omega - \left(H(t) - i\partial_t\right) + i\kappa\right]\left|b'\right\rangle &= -\sqrt{\kappa}\left|s^+\right\rangle \end{aligned} \tag{3.46}$$

Taking the inner product with $\langle k|$ on both sides and recognizing that $\langle k|b'\rangle = \tilde{b'}_k$, and $\langle k|(H(t) - i\partial_t)|b'\rangle = (H_k(t) - i\partial_t)\tilde{b'}_k$, we get

$$\left[\omega - \left(H_k(t) - i\partial_t\right) + i\kappa\right]\tilde{b'}_k = -\sqrt{\kappa}\left\langle k\middle|s^+\right\rangle \tag{3.47}$$

Further, notice that

$$\begin{aligned}\left\langle k\middle|s^{+}\right\rangle &= s^{+}\sum_{m}\sum_{n}e^{im\omega_0 k}e^{-in\omega_0 t}\left\langle m|n\right\rangle \\ &= s^{+}\sum_{m}\sum_{n}e^{i\omega_0(mk-nt)}\delta_{mn} = s^{+}\sum_{m}e^{im\omega_0(k-t)} \\ &= s^{+}\frac{2\pi}{\omega_0}\delta(k-t) = s^{+}T_0\delta(k-t)\end{aligned} \tag{3.48}$$

Therefore, we can now write Eq. (3.47) as

$$\left[\omega-\left(H_k(t)-i\partial_t\right)+i\kappa\right]\tilde{b'}_k = -\sqrt{\kappa}s^{+}T_0\delta(k-t) \tag{3.49}$$

Recall that ψ_{kn} are the eigenstates of the Floquet Hamiltonian. Thus, we can use $\psi_{kn}(t)$ as a complete basis and take the inner product with $\langle\psi_{kn}|$ on both sides. Since the inner product is the same as multiplying and integrating with $\frac{1}{T_0}\int_0^{T_0}\psi^{*}_{kn}(t)$, we now get

$$\begin{aligned}\left\langle\psi_{kn}\middle|\left[\omega-\left(H_k(t)-i\partial_t\right)+i\kappa\right]\middle|\tilde{b'}_k\right\rangle &= -\sqrt{\kappa}s^{+}T_0\cdot\frac{1}{T_0}\int_0^{T_0}\mathrm{d}t\psi^{*}_{kn}\delta(k-t) \\ &= -\sqrt{\kappa}s^{+}\psi^{*}_{kn}(t=k)\end{aligned} \tag{3.50}$$

But $\left\langle\psi_{kn}|H_k(t)-i\partial_t\middle|\tilde{b'}_k\right\rangle = \varepsilon_{k,n}\left\langle\psi_{kn}\middle|\tilde{b'}_k\right\rangle = (\varepsilon_k+n\omega_0)\left\langle\psi_{kn}\middle|\tilde{b'}_k\right\rangle$. Therefore, we can now re-write Eq. (3.50) as

$$\left\{\omega-(\varepsilon_k+n\omega_0)+i\kappa\right\}\left\langle\psi_{kn}\middle|\tilde{b'}_k\right\rangle = -\sqrt{\kappa}s^{+}\psi^{*}_{kn}(t=k) \tag{3.51}$$

or

$$\left\langle\psi_{kn}\middle|\tilde{b'}_k\right\rangle = \frac{-\sqrt{\kappa}s^{+}\psi^{*}_{kn}(t=k)}{\omega-(\varepsilon_k+n\omega_0)+i\kappa} \tag{3.52}$$

Since $\psi_{kn}(t)$ form a complete basis, we can expand the cavity modes $\tilde{b'}_k$ in terms of ψ_{kn} as $\tilde{b'}_k = \sum_n|\psi_{kn}\rangle\left\langle\psi_{kn}\middle|\tilde{b'}_k\right\rangle$ and find the steady-state transmission of the cavity output by

substituting Eq. (3.52) in Eq. (3.43) to get

$$\begin{aligned} s_d^- &= i\sqrt{\kappa}\tilde{b}_k \\ &= i\sqrt{\kappa}e^{-i\omega t}\tilde{b'}_k \\ &= i\sqrt{\kappa}e^{-i\omega t}\sum_n |\psi_{kn}\rangle \left\langle \psi_{kn}\middle|\tilde{b'}_k\right\rangle \\ &= i\sqrt{\kappa}e^{-i\omega t}\sum_n \psi_{kn}\left[\frac{-\sqrt{\kappa}s^+\psi^*_{kn}(t=k)}{\omega-(\varepsilon_k+n\omega_0)+i\kappa}\right] \\ &= -i\kappa s^+ e^{-i\omega t}\sum_n \left[\frac{|\psi_{kn}|^2}{\omega-(\varepsilon_k+n\omega_0)+i\kappa}\right]_{k=t} \end{aligned} \tag{3.53}$$

Assuming that the cavity linewidth will be much smaller than the FSR and $|J_{n-m}| < \omega_0/2$, we can safely choose the n in the summation in Eq. (3.53) for which the laser frequency is close to $n\omega_0$. Let the detuning from the laser frequency be $\Delta\omega = \omega - n\omega_0$. Given that the steady-state transmission $T = |s_d^-/s^+|^2$, we finally get

$$T = \left|\frac{s_d^-}{s^+}\right|^2 = \frac{\kappa^2}{(\Delta\omega-\varepsilon_k)^2+\kappa^2}|\psi_{kn}(k=t)|^4 \tag{3.54}$$

This expression tells us that as we sweep the laser frequency, we will see peaks at quasimomentum values $k = t$ as the laser detuning will be equal to the eigenvalues of the Floquet Hamiltonian at these particular times. As we will see in the experimental section, we will either see zero peaks, a single peak, or a double peak whenever the laser detuning equals the Floquet energies. We will eventually scan these peaks in a raster fashion and stack them on top of each other to form an image plot revealing the band structure in time. But before that we still need to figure out the eigenstates $\psi_{kn}(t)$ as $T \propto |\psi_{kn}|^4$. Thus, we first need to diagonalize the Floquet Hamiltonian.

Hamiltonian Diagonalization

To diagonalize the Floquet Hamiltonian and numerically calculate its eigenstates and eigenenergies, we can use the fact that $\psi_{kn}(t)$ is periodic with period T_0. This allows us to expand $\psi_{kn}(t)$ in the Fourier basis:

$$\psi_{kn}(t) = \sum_p e^{ip\omega_0 t}\tilde{\psi}_{kn}(p) \tag{3.55}$$

Thus, $|p\rangle = e^{ip\omega_0 t}$ forms a basis and we can look at the $(p'-p)^{\text{th}}$ component of the Floquet Hamiltonian, i.e.,

$$\begin{aligned}\langle p'|H_k(t) - i\partial_t|p\rangle &= \frac{1}{T_0}\int_0^{T_0} \mathrm{d}t e^{-ip'\omega_0 t}(H_k(t) - i\partial_t)e^{ip\omega_0 t} \\ &= \frac{1}{T_0}\int_0^{T_0} \mathrm{d}t e^{-ip'\omega_0 t}(H_k(t) + p\omega_0)e^{ip\omega_0 t}\end{aligned} \tag{3.56}$$

From Eq. (3.37), we get

$$\begin{aligned}\langle p'|H_k(t) - i\partial_t|p\rangle &= -\frac{1}{T_0}\int_0^{T_0} \mathrm{d}t e^{i(p-p')\omega_0 t}\sum_q J_q(t)e^{-iq\omega_0(k-t)} + p\frac{\omega_0}{T_0}\int_0^{T_0}\mathrm{d}t e^{i(p-p')\omega_0 t} \\ &= -\sum_q e^{-iq\omega_0 k}\left[\frac{1}{T_0}\int_0^{T_0} J_q(t)e^{i(p+q-p')\omega_0 t}\mathrm{d}t\right] + p\frac{\omega_0}{T_0}\frac{2\pi}{\omega_0}\delta(p-p') \\ &= p\omega_0\delta(p-p') - \sum_q e^{-iq\omega_0 k}\left[\frac{1}{T_0}\int_0^{T_0} J_q(t)e^{i(p+q-p')\omega_0 t}\mathrm{d}t\right]\end{aligned} \tag{3.57}$$

Now we go back to Eq. (3.23) and calculate the matrix elements for couplings with a cosinusoidal input to the phase modulator, i.e., we will work with $V_{\text{EOM}}(t) = V_0\cos\omega_0 t = \frac{1}{2}V_0(e^{i\omega_0 t} + e^{-i\omega_0 t})$. Notice that we used the frequency of the modulation as $\omega_0 (= \omega_{\text{FSR}})$ since we would like to couple the modes, and the nearest modes are a free-spectral range away. Therefore,

$$\begin{aligned}\frac{1}{T_0}\int_0^{T_0} J_q(t)e^{i(p+q-p')\omega_0 t}\mathrm{d}t &= -\frac{\omega_{\text{FSR}}}{2}\,\text{sinc}\left[2\pi q\frac{w}{L}\right]\frac{1}{T_0}\frac{V_0}{V_\pi}\int_0^{T_0} e^{i(p+q-p')\omega_0 t}\cos\omega_0 t\mathrm{d}t \\ &= -\frac{\omega_0 V_0}{4T_0 V_\pi}\,\text{sinc}\left[2\pi q\frac{w}{L}\right]\int_0^{T_0} e^{i(p+q-p')\omega_0 t}(e^{i\omega_0 t} + e^{-i\omega_0 t})\mathrm{d}t \\ &= -\frac{\omega_0 V_0}{4T_0 V_\pi}\,\text{sinc}\left[2\pi q\frac{w}{L}\right]\int_0^{T_0}(e^{i(p+q-p'+1)\omega_0 t} + e^{i(p+q-p'-1)\omega_0 t})\mathrm{d}t\end{aligned} \tag{3.58}$$

Notice that the integral on the RHS will evaluate to zero over one full period, i.e., $t \in [0, T_0]$ unless $p + q - p' \pm 1 = 0$, or $q = p' - p \mp 1$. At these values of q, the integral on the RHS simply gives us T_0 and we get

$$\frac{1}{T_0}\int_0^{T_0} J_{q=p'-p\mp1}(t)e^{i(p+q-p')\omega_0 t}\mathrm{d}t = -\frac{\omega_0 V_0}{4V_\pi}\,\text{sinc}\left[2\pi(p'-p\mp1)\frac{w}{L}\right] \tag{3.59}$$

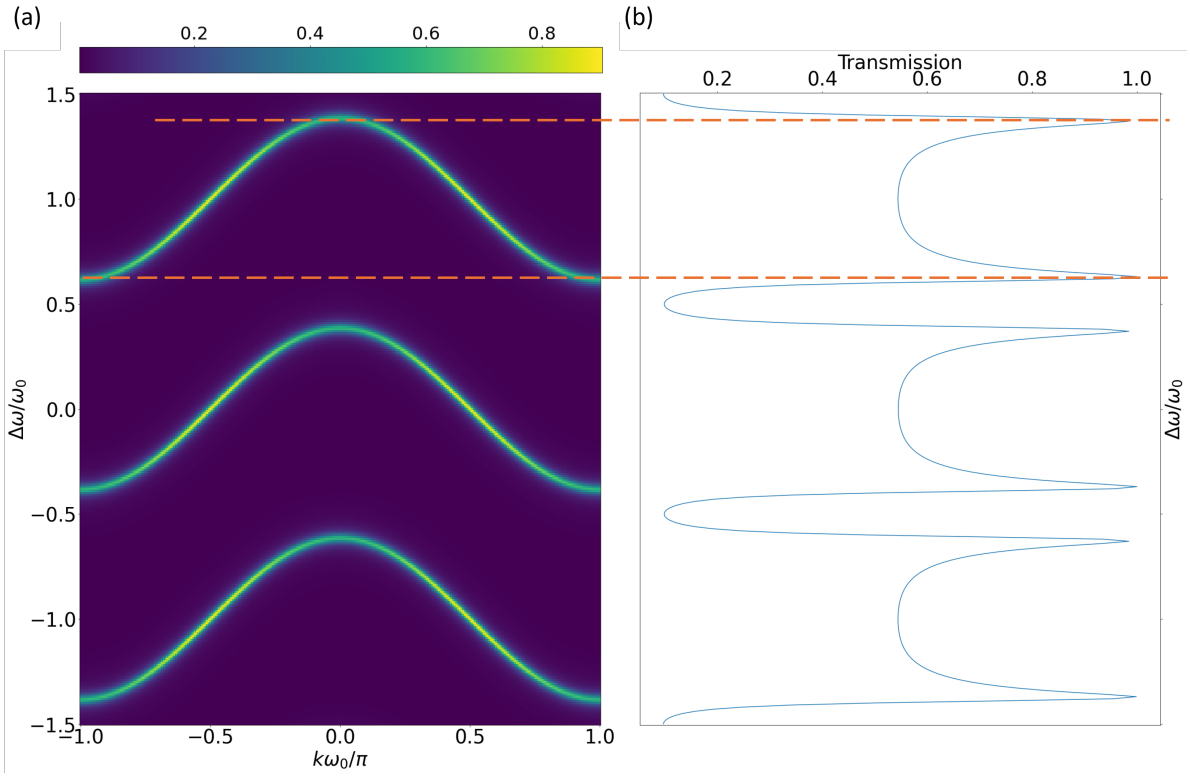


Figure 3.3: (a) Band structure resulting from a $V_0 = 10$V modulation, (b) Expected scope trace representing a 1D photonic density of states. To obtain the scope trace, we can integrate (or sum) over every eigenvalue $\Delta\omega$ in the band structure trace in (a). Note, this simulation was performed in collaboration with Dr. Zheng Shi.

and the sum in Eq. (3.57) collapses to only 2 values finally giving us the $(p'-p)^{\text{th}}$ matrix element as

$$\begin{aligned}\langle p'|H_k(t) - i\partial_t|p\rangle = p\omega_0\delta(p-p') &- \frac{\omega_0 V_0}{4V_\pi}\,\text{sinc}\left\{2\pi(p'-p+1)\frac{w}{L}\right\} \\ &- \frac{\omega_0 V_0}{4V_\pi}\,\text{sinc}\left\{2\pi(p'-p-1)\frac{w}{L}\right\}\end{aligned} \tag{3.60}$$

We can now write a code in Python with these matrix elements, set a limit to the maximum p to truncate the matrix, and use the numpy.linalg library to numerically diagonalize the Floquet Hamiltonian. We can then substitute the eigenvectors in Eq. (3.54) and plot the steady-state transmission T as a meshgrid.

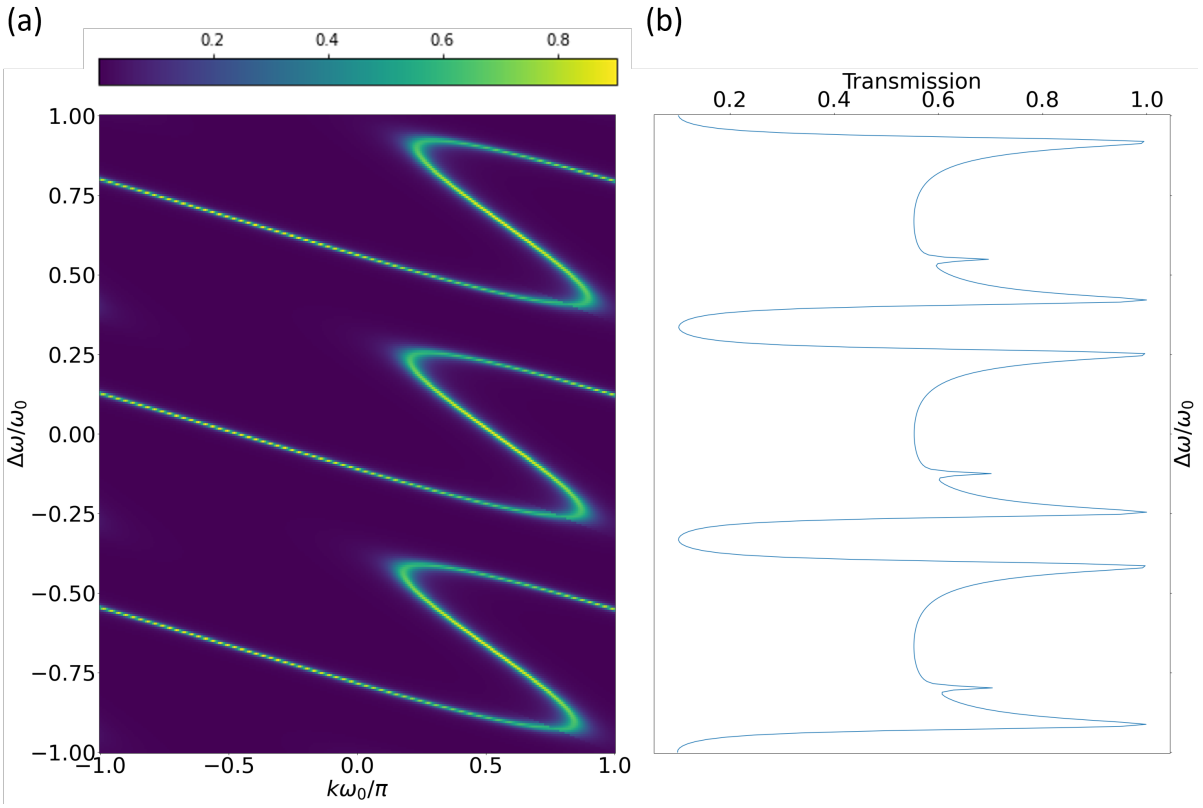


Figure 3.4: (a) Band structure resulting from a $V_0 = 10$V modulation when sliced off at a $\nu_{\mathrm{FSR}} = 17.1$ MHz (b) Expected scope trace. Note, this simulation was performed in collaboration with Dr. Zheng Shi.

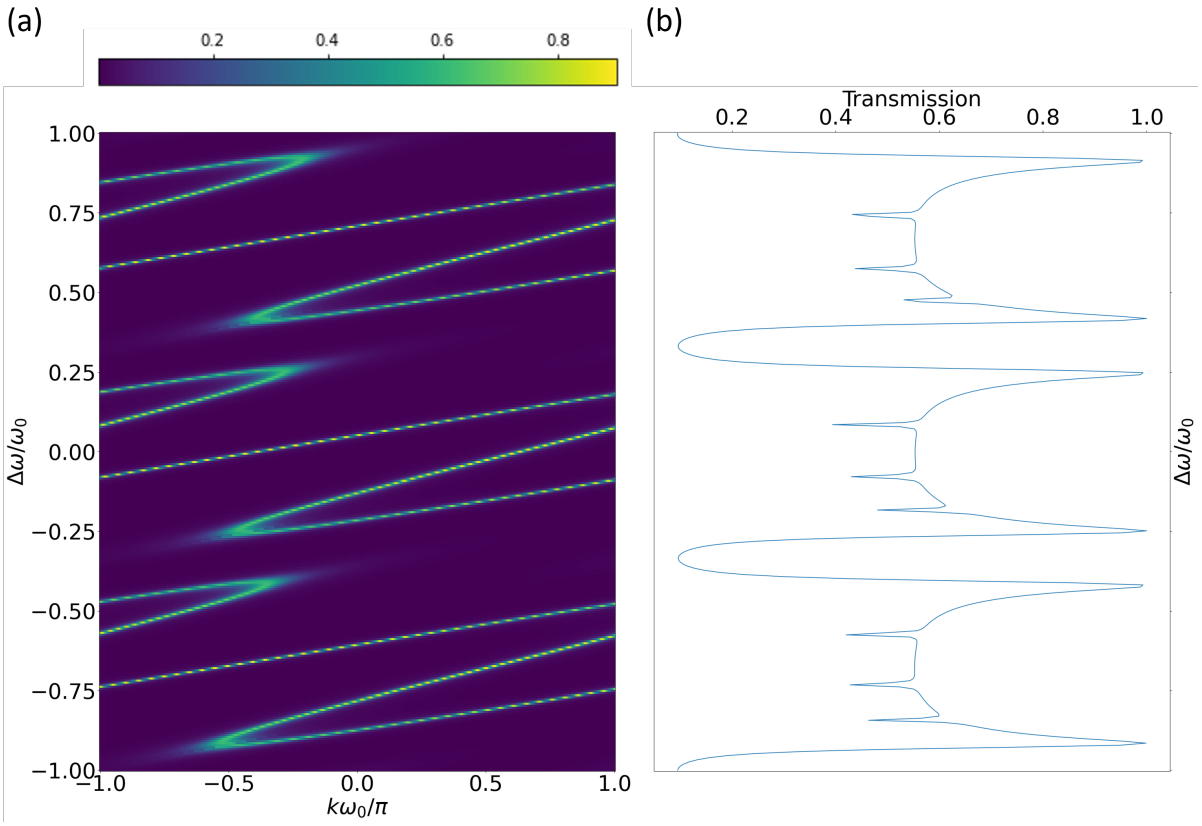


Figure 3.5: (a) Band structure resulting from a $V_0 = 10$V modulation when sliced off at a $\nu_{\mathrm{FSR}} = 17.62$ MHz (b) Expected scope trace. Note, this simulation was performed in collaboration with Dr. Zheng Shi.

To get a theoretical simulation of the above analysis, we can now relate some of this theory to our experimental setup. After attaching the Booster Optical Amplifier, the total length of the ring was $L = 11.755$ m corresponding to a free-spectral range of $\omega_{\text{FSR}} = 17.279$ MHz. Further, our Optilab phase modulator has a half-wave voltage of $V_\pi = 11$ V and an aspect ratio of $w/L = 0.05$, where w is the width of the Lithium-Niobate crystal. We also used a RF modulation voltage $V = V_0 \cos \omega_0 t$ with $V_0 = 10$V to excite our EOM. Lastly, for our theoretical simulations, we chose a cavity linewidth of $\kappa = \omega_0/50 = 345.58$ kHz, truncated our matrix with a $p_{\max} = 20$ and diagonalized it numerically with these values. Figure 3.3(a) shows an image plot for the expected theoretical band structure for a cosine modulation with $V_0 < V_\pi$. The horizontal axis of the plot are the quasimomentum values with $k \in [-\pi/\omega_0, \pi/\omega_0]$, the first Brillouin zone, and the vertical axis is the laser detuning normalized to the FSR. $\Delta\omega$ was measured in MHz. Figure 3.3(b) shows the expected scope trace. The theoretical scope trace was obtained by summing over the transmission intensity for every detuning $\Delta\omega$ as the scope trace represents the 1D photonic density of states. Figure 3.6 also shows an image plot and the expected trace for $V_0 > V_\pi$ with $V_0 = 13$ V.

In the experimental section, we will not only see a phase shifted band structure, but we will also see a moving effect when the scope trace will be sliced off using different free-spectral ranges. In Figures 3.4 and 3.5 we show how the band structure seems to be become asymmetric and phase shifts when sliced off at frequencies different than the FSR. We specifically sliced off at 17.1 MHz and 17.62 MHz, and the difference is within 3%. Although, we are able to see some moving effect, the band structure starts to dissolve when we slice off at frequencies very far off from the FSR. We also theoretically expect either dips or peaks in the middle of the scope trace patterns. To study the off-resonance effect on the band structure in-depth, we may have to reconstruct the entire theory starting from the coupled-mode equations.

Asymmetric Bands in Time

As was pointed out earlier, the couplings in Eq. (3.23) are independent of the form of the RF modulation voltage. Thus, we can attempt at trying to simulate asymmetric band structures by exciting the EOM with a general voltage $V_{\text{EOM}}(t) = V_1 \cos \omega_0 t + V_2 \cos(n\omega_0 t + \sigma)$. To understand the effect of such a modulation theoretically, we again find the $(p' - p)^{\text{th}}$ matrix element of the Floquet Hamiltonian. We start by solving for the integral

$$\frac{1}{T_0}\int_0^{T_0} J_q(t) e^{i(p+q-p')\omega_0 t} \mathrm{d}t = -\frac{\omega_0}{2} \operatorname{sinc}\left[2\pi q \frac{w}{L}\right] \frac{1}{V_\pi} \frac{1}{T_0} \int_0^{T_0} e^{i(p+q-p')\omega_0 t} V_{\text{EOM}}(t) \mathrm{d}t \quad (3.61)$$

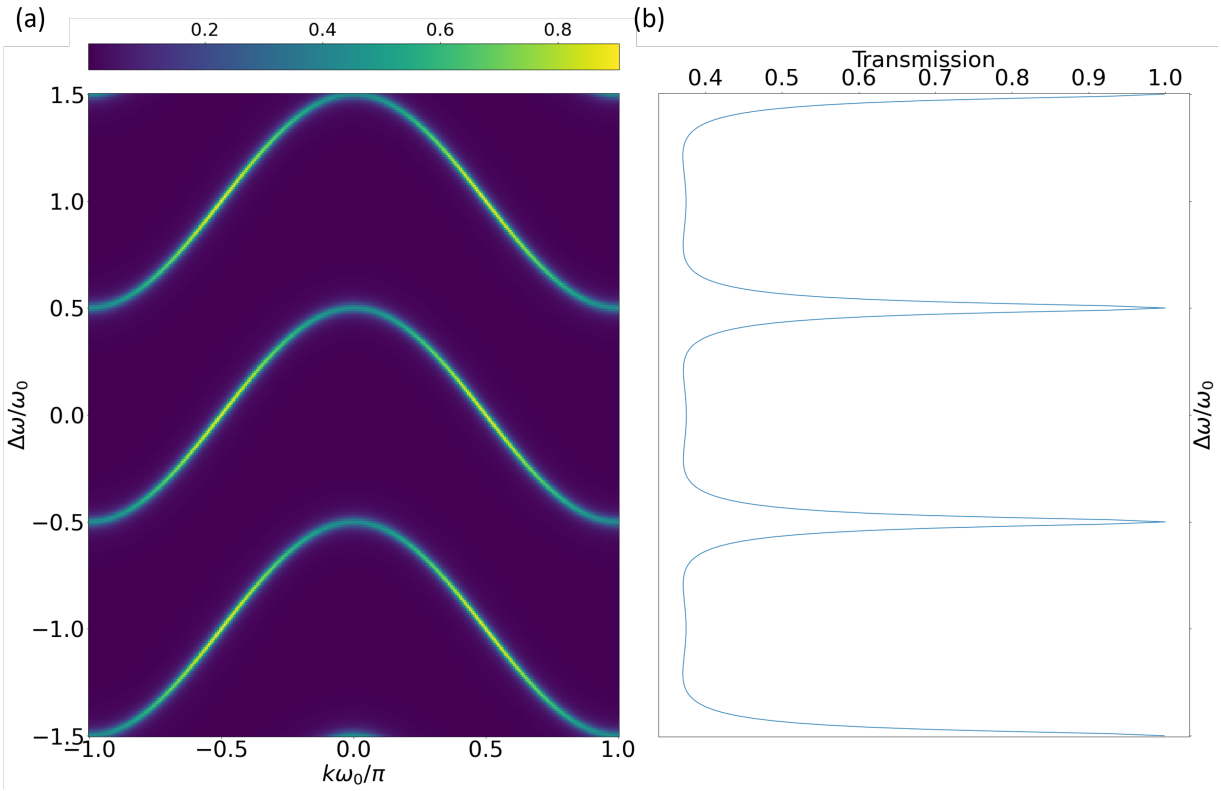


Figure 3.6: (a) Band structure for a $V_0 = 13$V modulation (b) Expected scope trace. Note, this simulation was performed in collaboration with Dr. Zheng Shi.

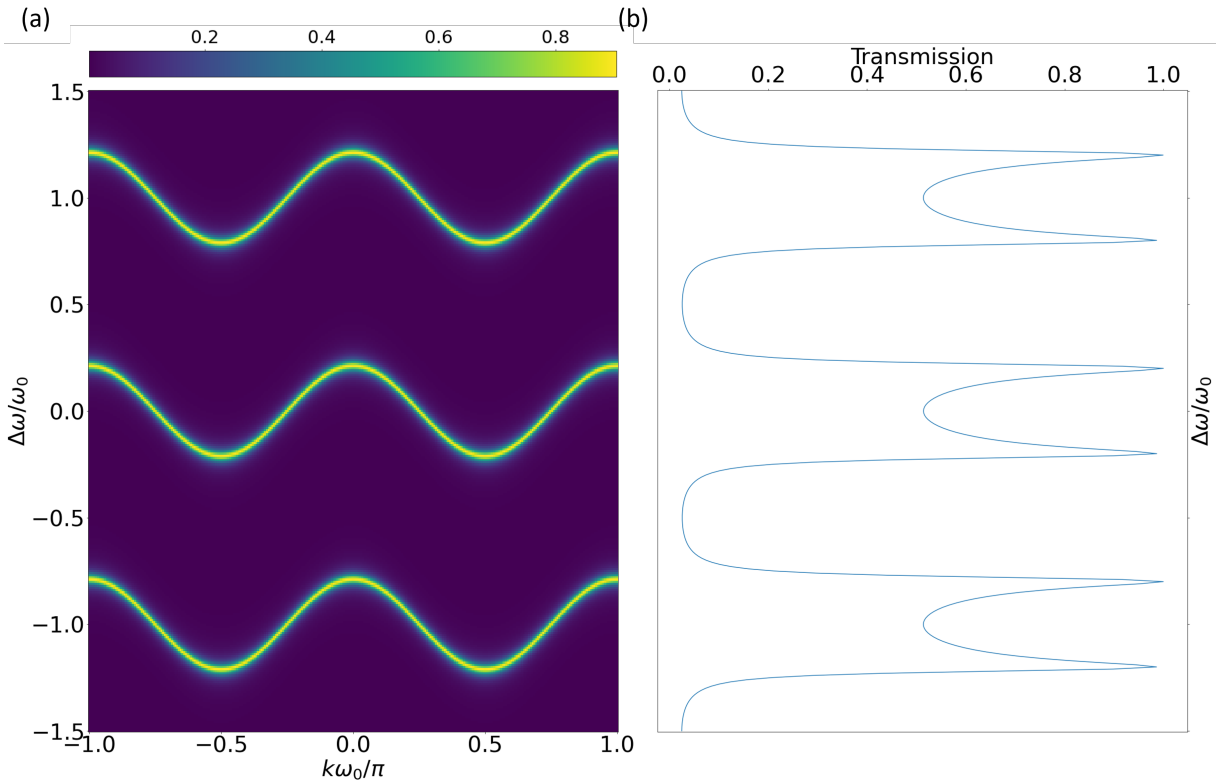


Figure 3.7: (a) Band structure for $V_1 = 0$V, $V_2 = 10$V, $n = 2$, $\sigma = 0$; (b) Expected scope trace. Note, this simulation was performed in collaboration with Dr. Zheng Shi.

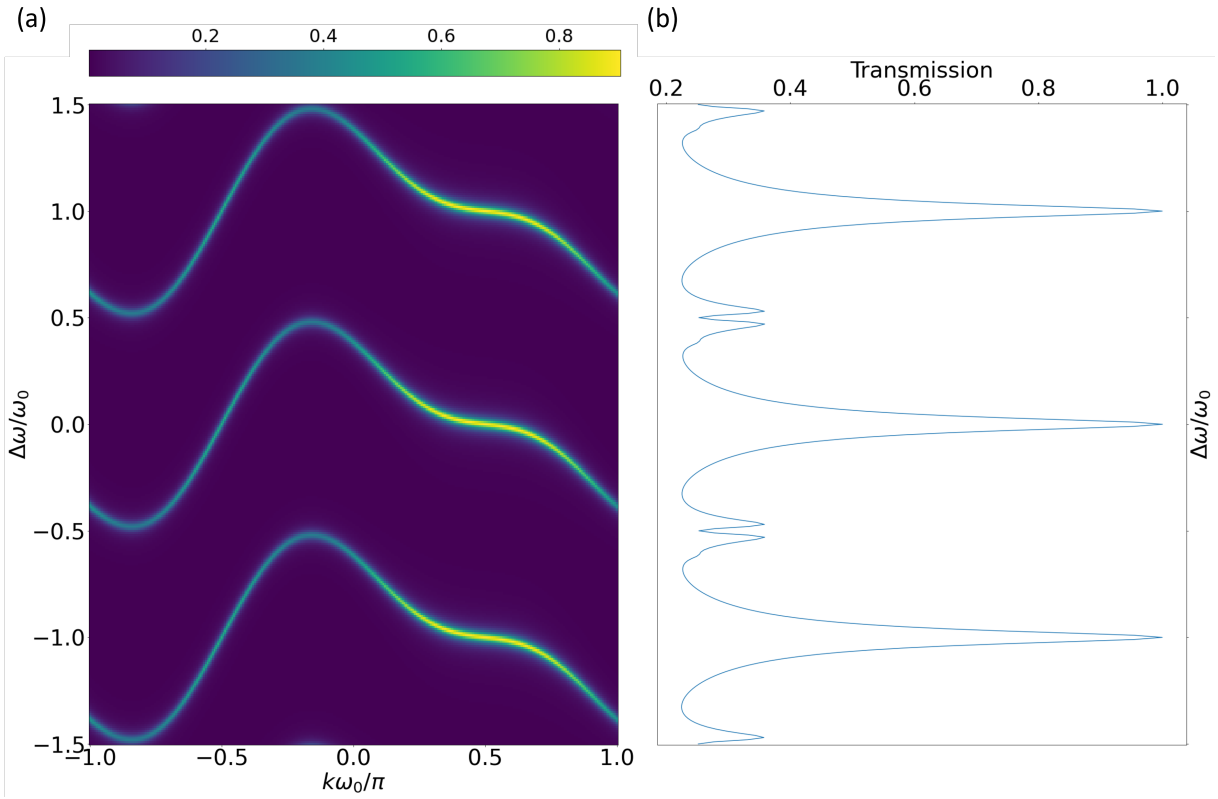


Figure 3.8: (a) Band structure for $V_1 = 10\text{V}$, $V_2 = 8\text{V}$, $n = 2$, $\sigma = \pi/2$; (b) Expected scope trace. Note, this simulation was performed in collaboration with Dr. Zheng Shi.

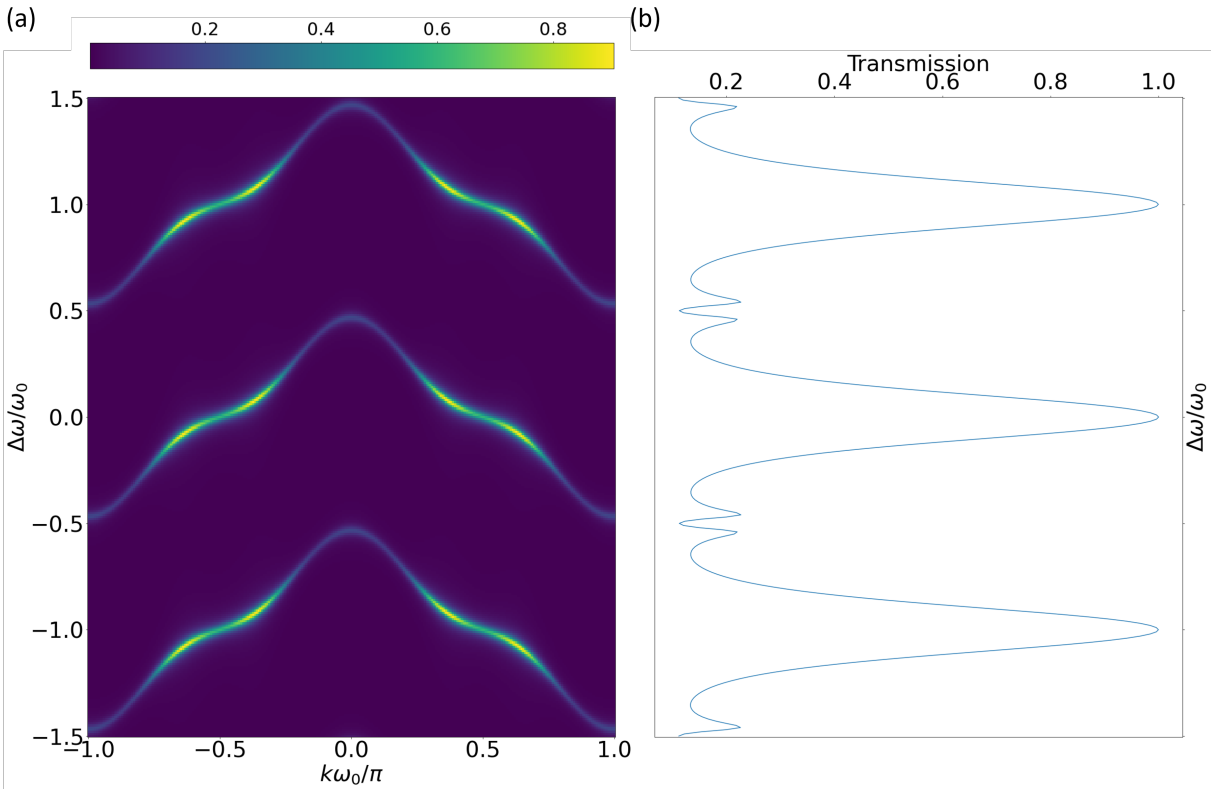


Figure 3.9: (a) Band structure for $V_1 = 10\text{V}$, $V_2 = 30\text{V}$, $n = 3$, $\sigma = 0$; (b) Expected scope trace. Note, this simulation was performed in collaboration with Dr. Zheng Shi.

Since the integral can be split over the sum, the first term will be again simply

$$\int_0^{T_0} e^{i(p+q-p')\omega_0 t} V_1 \cos\omega_0 t = V_1 \int_0^{T_0} (e^{i(p+q-p'+1)\omega_0 t} + e^{i(p+q-p'-1)\omega_0 t}) \mathrm{d}t \tag{3.62}$$

and the integral can only evaluate to a non-zero value when $q = p' - p \mp 1$. The value of the integral will then be $V_1 T_0$. But in the second term, we will also see the effect of the phase σ as

$$\int_0^{T_0} e^{i(p+q-p')\omega_0 t} V_2 \cos(n\omega_0 t + \sigma) = V_2 \int_0^{T_0} (e^{i(p+q-p'+n)\omega_0 t} e^{i\sigma} + e^{i(p+q-p'-n)\omega_0 t} e^{-i\sigma}) \mathrm{d}t \tag{3.63}$$

Here, the integral will evaluate to a non-zero value only when $q = p' - p \mp n$ and the value of the integral will be $V_2 T_0 e^{i\sigma}$ when $q = p' - p - n$ and $V_2 T_0 e^{-i\sigma}$ when $q = p' - p + n$. Therefore, the sum in Eq. (3.57) will collapse to 4 values giving the $(p' - p)^{\text{th}}$ matrix element as

$$\begin{aligned} \langle p'|H_k(t) - i\partial_t|p\rangle = p\omega_0\delta(p-p') &- \frac{\omega_0 V_1}{4V_\pi} \operatorname{sinc}\left\{2\pi(p'-p-1)\frac{w}{L}\right\} \\ &- \frac{\omega_0 V_1}{4V_\pi} \operatorname{sinc}\left\{2\pi(p'-p+1)\frac{w}{L}\right\} \\ &- \frac{\omega_0 V_2}{4V_\pi} \operatorname{sinc}\left\{2\pi(p'-p-n)\frac{w}{L}\right\} e^{i\sigma} \\ &- \frac{\omega_0 V_2}{4V_\pi} \operatorname{sinc}\left\{2\pi(p'-p+n)\frac{w}{L}\right\} e^{-i\sigma} \end{aligned} \tag{3.64}$$

As in the previous sub-section, we will now look at the theoretical results for a few cases. As before, $\omega_0 = 17.279$ MHz, $V_\pi = 11$ V, aspect ratio $w/L = 0.05$, and linewidth $\kappa = \omega_0/50 = 345.58$ kHz. Figure 3.7 shows the band structure for $V_1 = 0$, $V_2 = 10$ V, $n = 2$, and $\sigma = 0$. Figure 3.8 shows the band structure for $V_1 = 10$ V, $V_2 = 8$ V, $n = 2$, and $\sigma = \pi/2$. Lastly, Figure 3.9 shows the band structure for $V_1 = 10$ V, $V_2 = 30$ V, $n = 3$, and $\sigma = 0$.

3.2.2 Experimental Results

As we saw earlier, we modified the ring resonator to add an EOM, a BOA, and a DWDM. The final setup can be seen in Figures 3.10 and 3.11. The free-spectral range of the ring—as pointed out in the last section—is $\nu_{\text{FSR}} = 17.279$ MHz. This FSR is actually an approximation as there can be length imperfections in the cavity. For example, due

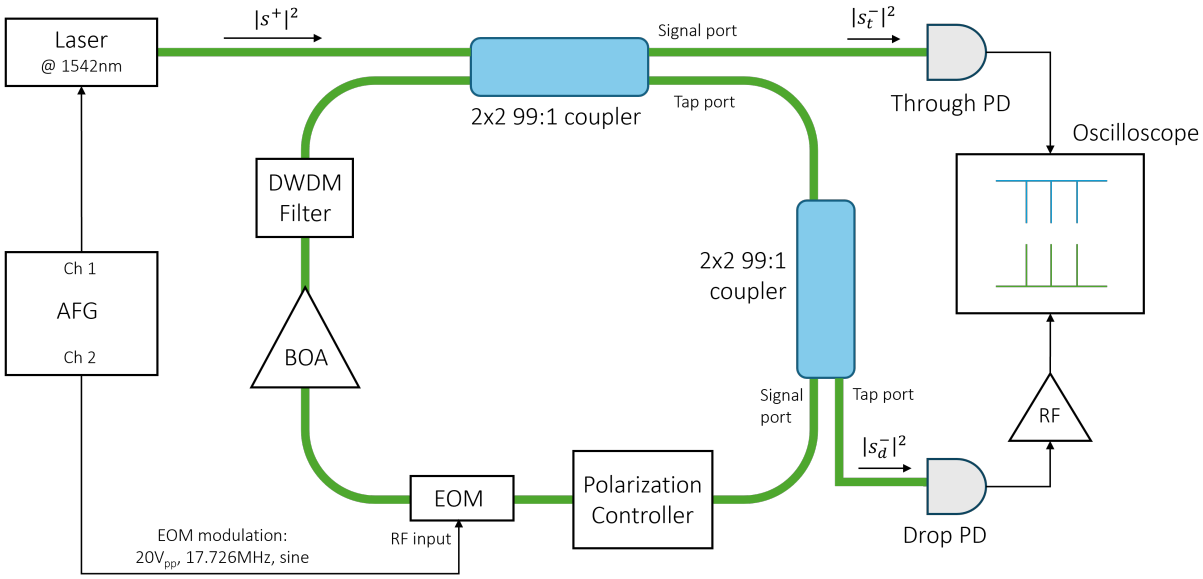


Figure 3.10: Experimental setup for a modified ring resonator to determine the band structure in a synthetic dimension

to thermal effects, the optical path length can actually differ from the physical length. Thus, to get the band structure, the RF frequency exciting the RF port was varied near ν_{FSR}. We specifically excited the EOM with a sinusoid of amplitude $20V_{\text{pp}}$ and frequency $\nu_{\text{EOM}} = 17.818$ MHz. The BOA was operated at a temperature of 35°C and a current of 135 mA to compensate for a 2.94 dB insertion loss from the EOM and a 0.18 dB loss from the pass channel of the DWDM. If we isolate the BOA and give it a laser input of approximately –10 dBm (100 μW), a current of 135 mA corresponds to a gain of about 9.5 dB.

The cavity output was observed with a 5 GHz fast InGaAs photodiode at the drop-port. This signal was fed to a SRS pre-amplifier and boosted by a gain of 25(V/V) by cascading two of its channels. And finally, the signal was observed on a fast 8 GHz Keysight oscilloscope. The acquisition time of the trace was 1 ms and 1.125 million points were collected at a sampling rate of 1.25 GSa/s. The trace was then down-sampled to 2^{20} points (corresponding to a 0.932 ms acquisition time) by eliminating points from the tail of the trace. The scope trace can be seen in Figure 3.12(a). Notice that the signal is incredibly small (max 20 mV) and incredibly noisy. The noise is largely thermal resulting from the two cascaded channels of the SRS with a standard deviation of $\text{ACV}_{\text{rms}} \sim 5$ mV, which is highly comparable to the signal maximum of 20 mV.

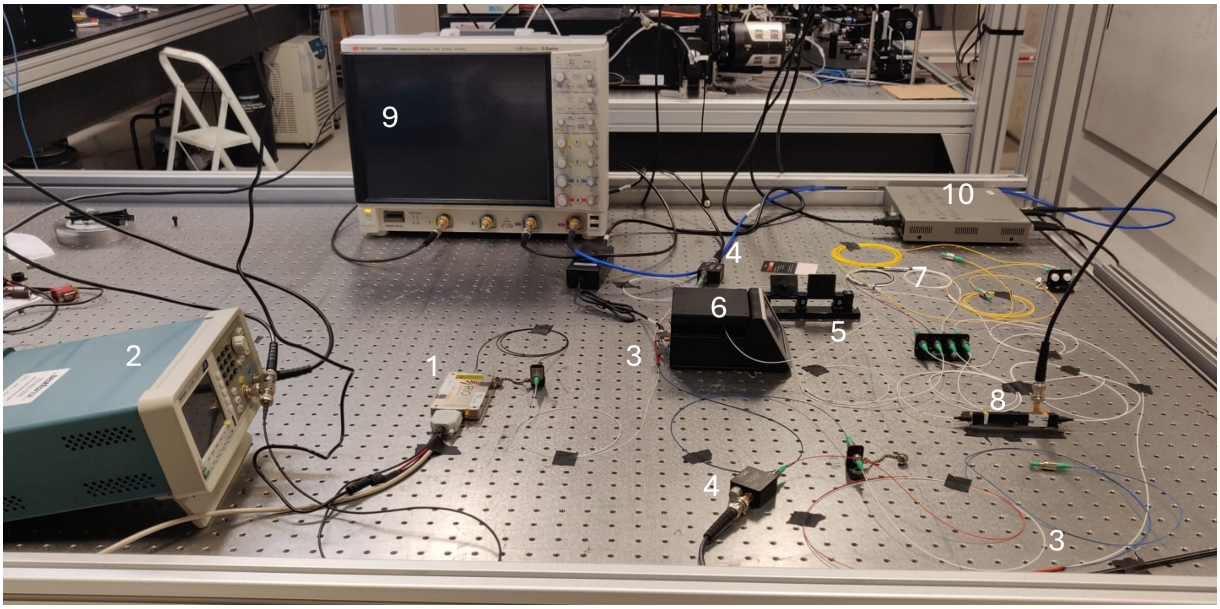


Figure 3.11: Experimental Setup: 1. Rio Orion 1542 nm laser, 2. Tektronix AFG1062 – 2 channel, 3. Thorlabs 2x2 99:1 couplers, 4. Thorlabs 5 GHz InGaAs PDs, 5. Thorlabs paddle polarization controller, 6. Thorlabs 26 dB gain Booster Optical Amplifier + Temperature Controller, 7. Fiberdyne 100 GHz, 1550 nm DWDM filter, 8. Optilab 10 GHz, 1550 nm electro-optic phase modulator, 9. Keysight 8 GHz, 20 GSa/s oscilloscope, 10. SRS DC – 350 MHz amplifier

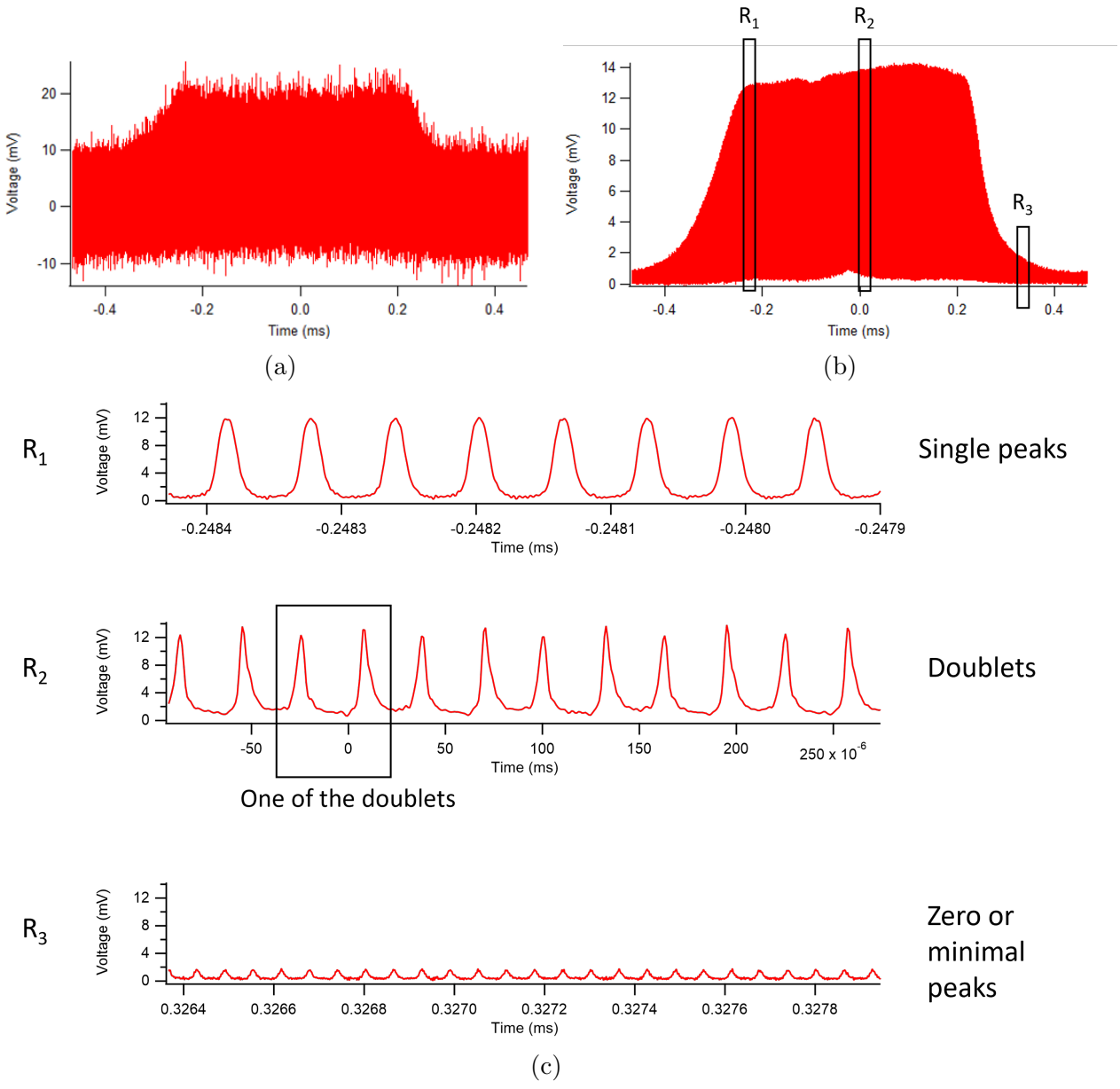


Figure 3.12: (a) Scope Trace, (b) Averaged scope trace indicating regions R_1, R_2, and R_3, (c) Regions R_1, R_2, and R_3 in (b) have been magnified to show a single peak, doublets, and no peaks as a result of phase modulation.

To reduce the noise and improve the SNR of the signal, we averaged over 1000 such noisy datasets. Since the fiber-optic cavity causes a thermal drift at the MHz scale, the 1000 datasets were all drifted apart from each other. As we can observe in Figure 3.3, the basic pattern we need to recognize in the scope trace is two peaks containing a valley. In the figure, a single pattern is contained within $-0.5 < \Delta\omega/\omega_0 < 0.5$ with the peaks with transmission $T = 1$ and the valley with transmission $T \approx 0.6$. The figure shows three such patterns and hence three band structures. In Figure 3.12a, the maximum is around 20 mV and contained within $\approx \pm 0.25$ ms. Thus, we first imposed boundaries and collected data only when the maximas were within ± 0.3 ms. Next, we took one such scope trace and using it as a reference, correlated the other 999 datasets with it. The correlation function in Igor Pro works as a discrete convolution sum and calculates a correlation function value by delaying a dataset with the reference using the Fast-Fourier Transform (FFT) algorithm. The delay corresponding to the maximum function value tells us how much we need to shift the dataset by for maximum correlation. In other words, if the delay corresponding to the function maximum is t_d, we rotate (or shift cyclically) the dataset by $-t_d$ to align the maximas of the band structure pattern with the reference. We then correlate and rotate all the remaining 999 datasets with the reference, and average over them to get the pattern in Figure 3.12b. Earlier, we down-sampled the datasets from 1.125 million to 2^{20} points. This was done as FFT, and hence correlation, works fastest when the number of points in datasets is a power of 2. As a result, the total time taken by this averaging procedure was 32 minutes.

Even though Figure 3.12(b) still does not match the theoretical pattern in Figure 3.3, we can still extract useful information—as can be observed in Figure 3.12(c))—so we can start to see the band structure. To get the band structure, we use the "Redimension" command in Igor Pro. We first note that the time corresponding to the FSR is $t_{\text{FSR}} = 1/\nu_{\text{FSR}} = 57.88$ ns. Thus, we take the 0.932 ms one-dimensional scope trace and re-dimension it in to a 2D matrix such that every row is a 57.88 ns interval corresponding to 65 data points. And we get 16015 such rows stacked vertically as can be seen in Figure 3.13. The horizontal axis in the figure corresponds to the quasimomentum values $t_{\text{FSR}} \in [-28.94 \text{ ns}, +28.94 \text{ ns}]$ with a total length of 57.88 ns. And the vertical axis corresponds to the laser detuning (in MHz) across the time trace converted using the ramp function for laser frequency sweeping.

We can also notice an interesting feature as can be seen in Figures 3.14(a) and (b) where it seems that the band structures seem to be phase shifting when we re-dimension using different free-spectral ranges. Figure 3.14a was obtained with $\nu_{\text{FSR}} = 17.1$ MHz and is a 2D plot with dimensions (15938 x 65). Similarly, 3.14b has dimensions (16497 x 63) and was obtained by using $\nu_{\text{FSR}} = 17.7$ MHz.

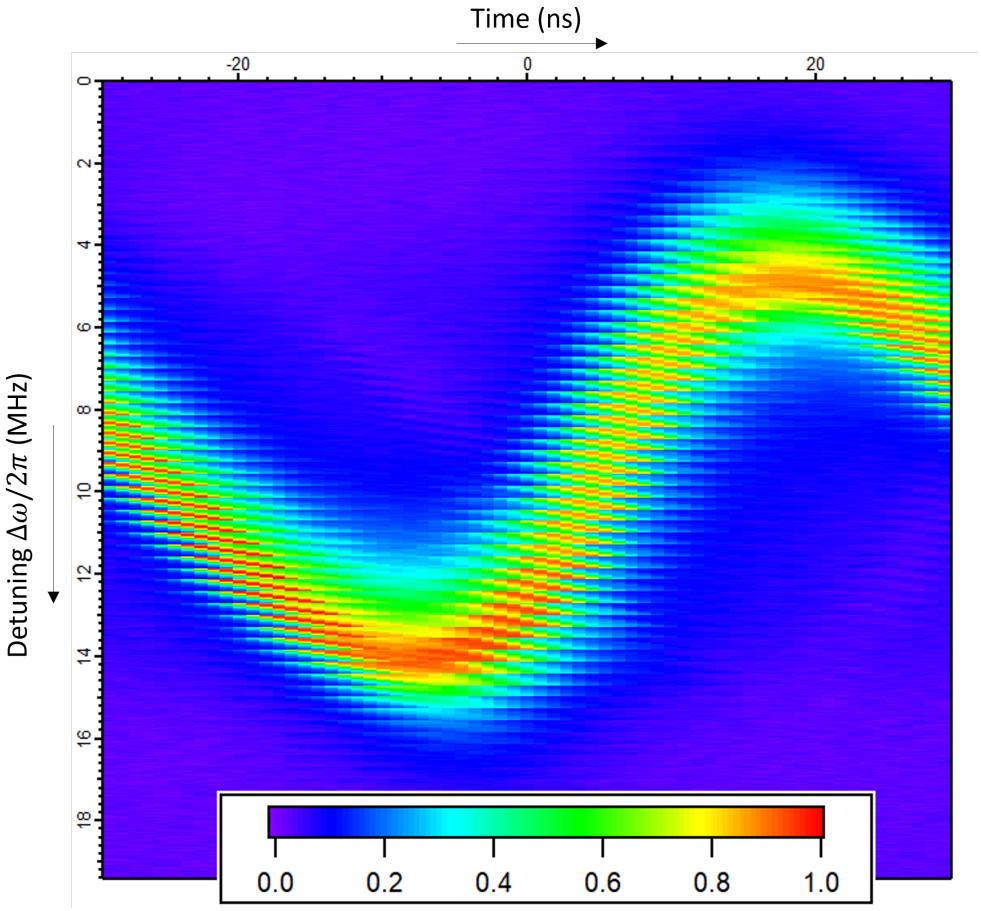
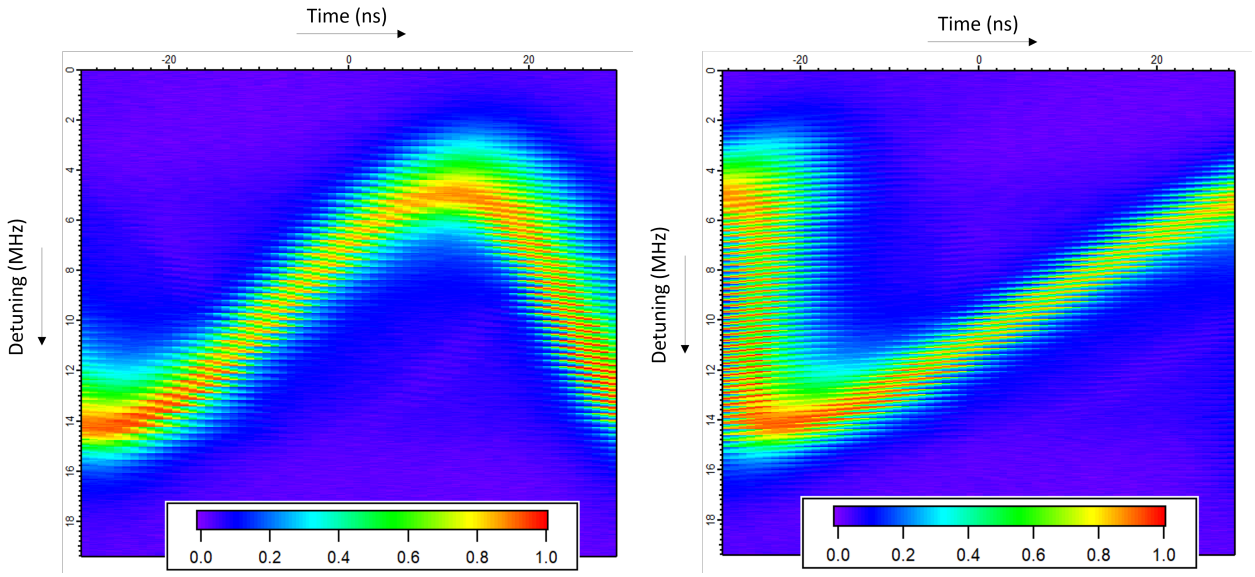


Figure 3.13: Band Structure obtained by changing the 1D averaged scope trace in Figure 3.12(b) to a 2D plot.



(a) (b)

Figure 3.14: Resulting band structures when the one-dimensional scope trace in Figure 3.12(b) is converted to a two-dimensional image plots using different free-spectral ranges (a) $\nu_{\text{FSR}} = 17.1$ MHz (b) $\nu_{\text{FSR}} = 17.7$ MHz

3.3 Future Work

As a first pass, we have started to observe the band structure in time. But the result needs improvement. For starters, in Figure 3.12(b), we can see that the averaged scope trace does not resemble the steady-state transmission as expected from the theoretical simulation in Figure 3.3(b) as the signal we received on the photodiode is incredibly small. Practically, we need another optical amplifier to improve the SNR of the optical output from the ring resonator. Next, in Figures 3.13 and 3.14, we can see a huge number of horizontal streaks which need to be resolved. Lastly, it remains to be figured out why the band structures seem to be tilted.

Further, the results presented in this chapter are only for a modulation of the form $V_{\text{EOM}}(t) = V_0 \cos \omega_0 t$. We still need to extend the experimental results for a modulation of the form $V_{\text{EOM}}(t) = V_1 \cos \omega_0 t + V_2 \cos(n\omega_0 t + \sigma)$ to observe asymmetric band structures as seen in theoretical simulations in Figures 3.7, 3.8, and 3.9.

Given these experimental results, we can also be in a strong position to perform future

experiments and replicate other papers from the main authors to observe other interesting topological features in synthetic dimensions. For example, in Ref. [30], the authors Li et. al. extended the setup and connected two ring resonators with a 50:50 beam splitter to extract the Zak phase from the bulk band structure of the Su-Schrieffer-Heeger model. In Ref. [15], the authors have created two independent physical synthetic frequency dimensions—one formed by the longitudinal cavity modes, and the other is a synthetic pseudospin dimension formed by the clockwise and counter-clockwise modes—thereby creating a synthetic Hall ladder. This allowed them to study spin-orbit coupling, spin-momentum locking, magnetic fields, and Meissner-to-vortex phase transitions in the synthetic dimension. And in Ref. [16], the authors have studied winding of energy bands in the complex energy plane, a topological feature typical of non-Hermitian systems. They implemented the non-Hermitian lattice Hamiltonian along a synthetic frequency dimension of a ring resonator undergoing simultaneous phase and amplitude modulation with two EOMs.

Thus, our current results serve as a strong starting point to continue exploring the plethora of opportunities offered by synthetic dimensions.

Chapter 4

Conclusions

In conclusion, we have investigated how resonators, and specifically ring resonators, can be used to develop a synthetic frequency dimension to explore topological phenomena both theoretically and experimentally. In this thesis, we first began with looking at the most basic resonator, a Fabry-Perot resonator by deriving its transmission and reflection spectrum. We then extended our analysis and explored coupled-mode theory. The basics of coupled-mode theory were looked at in their full generality and applied to the case of the Fabry-Perot resonator. Coupled-mode theory specifically looks at how resonator modes in a single cavity or multiple cavities evolve in time when coupled with external waveguides for input and output in terms of simple algebraic and first-order differential equations of motion. Thus, we were able to model the Fabry-Perot resonator as a single cavity connected to two waveguide ports for input and output. At the end of Chapter 1, we concluded that the result from a general application of electric fields and coupled-mode theory lead us to the same result for the expressions of transmission and reflection spectrum if we Taylor expanded the round-trip phase and realized the relation between the cavity linewidth and the transmissivity of the mirrors.

We then began Chapter 2 by looking at the ring resonator, expanding the theoretical results from Chapter 1, and developing a coupled-mode theory for both an all-pass and add-drop ring resonators. We first started with an all-pass ring resonator where a single ring is evanescently coupled with a bus waveguide for both input and output by first deriving the transmission spectrum via the through port from basic beam-splitter relations and subsequently developing a coupled-mode theory for it. Given the curved nature of the ring resonator, it was important to note that it was the intrinsic cavity loss which resulted in cavity resonances. We then extended the coupled-mode theory to the case of an add-drop ring resonator where the ring is evanescently coupled to a bus and a re-

ceiver waveguide for input and output. The coupled-mode theory for an add-drop ring indicated that the theoretical transmission via the through and drop ports were identical to the case of a Fabry-Perot resonator connected to two waveguides. This allowed us to state the transmission expressions via the through and drop output waveguides in a straightforward fashion. Next, we experimentally developed an all optical-fiber add-drop ring resonator with off the shelf fiber optic components. We first started by connecting two fiber beam-splitters to observe the cavity resonances via the drop port, and calculated the quality factor of the ring. We then modified the ring by adding other components like a Dense-Wavelength Division Multiplexing filter, an electro-optic modulator, and an optical amplifier, and observed how they modified the cavity response by lowering the quality factor of the ring.

Lastly, in Chapter 3, we finally explored how the ring resonator can be used to develop a synthetic dimension in frequency space. Since a ring resonator has equally space frequency modes separated by a Free-Spectral Range, we can use an electro-optic modulator to couple the modes by applying a voltage $V_{\text{EOM}} = V_0 \cos \omega_0 t$ at the same frequency as the free-spectral range. In solid-state physics, atoms placed periodically a lattice constant apart are coupled via a Coulomb interaction. This leads to energy band structures in the reciprocal momentum space. In a similar fashion, by modulating a cavity at the same frequency as the free-spectral range, we can expect energy band structures in the 'time' space, as time and frequency are reciprocal to each other. In Chapter 3, we start by developing a coupled-mode theory for every resonator mode of the ring perturbed by an electro-optic modulator by solving Maxwell's equations. The coupling between modes is revealed to be directly related to the modulation voltage V_{EOM} apart from a sinc function dependent on the aspect ratio and electro-optic coefficient of the Lithium-Niobate nonlinear crystal inside the modulator. Interestingly, the coupling was time periodic with period as the inverse of the free-spectral range. We then took a rotating-wave approximation and figured out the Hamiltonian for such a system leading to a time-periodic Hamiltonian. This allowed us to develop a Schrodinger's equation for the Floquet Hamiltonian by transforming the system in the Bloch basis. We now moved to an open system by exciting the cavity with a laser input. Upon solving the coupled-mode equations, we realized a steady-state transmission through the drop port dependent on the eigenfunctions of the Floquet Hamiltonian and the detuning of the cavity dependent on the eigenenergies. Upon diagonalizing the Hamiltonian for a cosinusoidal modulation voltage, the band structures were revealed. Given that these bands are 1D photonic density of states, we were able to integrate them and get a picture of the expected scope trace. Here, we were also able to use the methodology developed to look at some asymmetric band structures by applying a modulation voltage of the form $V_{\text{EOM}} = V_1 \cos \omega_0 t + V_2 \cos n\omega_0 t + \sigma$. We then proceeded to observe at least the

symmetric cosine band structure experimentally by correlating and averaging datasets. We also noticed an interesting effect where we were able to see the band phase shift when we changed the dimensions of the 2D image plots obtained from the 1D scope traces.

Possible future directions for the project involves optical amplification to improve the signal-to-noise ratio to clearly observe the band structures, experimentally observing asymmetric band structures and confirming the theory in Chapter 3, and exploring other topological features like spin-orbit coupling, spin-momentum locking, magnetic fields, and Meissner-to-vortex phase transitions by developing synthetic Hall ladders by coupling multiple ring resonators.

References

[1] B. E. Saleh and M. C. Teich, *Fundamentals of Photonics*. Wiley Series in Pure and Applied Optics, 3rd ed., 2019.

[2] S. Haroche and J.-M. Raimond, "Radiative properties of rydberg states in resonant cavities," *Advances in Atomic and Molecular Physics*, vol. 20, 1985.

[3] P. Krantz, M. Kjaergaard, F. Yan, T. P. Orlando, S.Gustavsson, and W. D. Oliver, "A quantum engineer's guide to superconducting qubits," *Appl. Phys. Rev. 6 (2): 021318*, 2019.

[4] D. Englund, D. Fattal, E. Waks, G. Solomon, B. Zhang, T. Nakaoka, Y. Arakawa, Y. Yamamoto, and J. Vuckovic, "Controlling the spontaneous emission rate of single quantum dots in a two-dimensional photonic crystal," *PRL 95, 013904*, 2005.

[5] J. D. Thompson, B. M. Zwickl, A. M. Jayich, F. Marquardt, S. M. Girvin, and J. G. E. Harris, "Strong dispersive coupling of a high-finesse cavity to a micromechanical membrane," *Nature volume 452, pages 72–75*, 2008.

[6] E. Verhagen, S. Deléglise, S. Weis, A. Schliesser, and T. J. Kippenberg, "Quantum-coherent coupling of a mechanical oscillator to an optical cavity mode," *Nature*, vol. 482, pp. 63–67, 2012.

[7] G. Anetsberger, O. Arcizet, Q. P. Unterreithmeier, R. Rivière, A. Schliesser, E. M. Weig, J. P. Kotthaus, and T. J. Kippenberg, "Near-field cavity optomechanics with nanomechanical oscillators," *Nature Physics*, vol. 5, pp. 909–914, 2009.

[8] I. M. Georgescu, S. Ashhab, and F. Nori, "Quantum simulation," *Rev. Mod. Phys.*, vol. 86, pp. 153–185, Mar 2014.

[9] K. Kim, M.-S. Chang, S. Korenblit, R. Islam, E. E. Edwards, J. K. Freericks, G.-D. Lin, L.-M. Duan, and C. Monroe, "Quantum simulation of frustrated ising spins with trapped ions," *Nature*, vol. 465, pp. 590–593, 2010.

[10] C. Monroe, W. C. Campbell, L.-M. Duan, Z.-X. Gong, A. V. Gorshkov, P. W. Hess, R. Islam, K. Kim, N. M. Linke, G. Pagano, P. Richerme, C. Senko, and N. Y. Yao, "Programmable quantum simulations of spin systems with trapped ions," *Rev. Mod. Phys.*, vol. 93, p. 025001, Apr 2021.

[11] R. Ma, B. Saxberg, C. Owens, N. Leung, Y. Lu, J. Simon, and D. I. Schuster, "A dissipatively stabilized mott insulator of photons," *Nature*, vol. 566, pp. 51–57, 2019.

[12] M. Fitzpatrick, N. M. Sundaresan, A. C. Y. Li, J. Koch, and A. A. Houck, "Observation of a dissipative phase transition in a one-dimensional circuit qed lattice," *Phys. Rev. X*, vol. 7, p. 011016, Feb 2017.

[13] L. Yuan, A. Dutt, and S. Fan, "Synthetic frequency dimensions in dynamically modulated ring resonators," *APL Photonics*, 2021.

[14] A. Dutt, M. Minkov, Q. Lin, L. Yuan, D. A. B. Miller, and S. Fan, "Experimental band structure spectroscopy along a synthetic dimension," *Nat Commun*, vol. 10, p. 3122, 2019.

[15] A. Dutt, Q. Lin, L. Yuan, M. Minkov, M. Xiao, and S. Fan, "A single photonic cavity with two independent physical synthetic dimensions," *Science*, vol. 367, pp. 59–64, 2019.

[16] K. Wang, A. Dutt, K. Y. Yang, C. C. Wojcik, J. Vučković, and S. Fan, "Generating arbitrary topological windings of a non-hermitian band," *Science*, vol. 371, pp. 1240–1245, 2021.

[17] H. A. Haus, *Waves and Fields in Optoelectronics*. Englewood Cliffs, NJ: Prentice Hall, 1984.

[18] J. D. Joannopoulos, S. G. Johnson, J. N. Winn, and R. D. Meade, *Photonic Crystals: Molding the Flow of Light*. Princeton University Press, 2nd ed., 2008.

[19] R. Trivedi, D. Lukin, and J. Vuckovic, "Lecture notes on ee340: Optical micro and nano resonators," 2019.

[20] W. Bogaerts, P. D. Heyn, T. V. Vaerenbergh, K. D. Vos, S. K. Selvaraja, T. Claes, P. Dumon, P. Bienstman, D. V. Thourhout, and R. Baets, "Silicon microring resonators," *Laser Photonics Rev. 6, No. 1*, pp. 47–73, 2012.

[21] C. Manolatou, M. Khan, S. Fan, P. Villeneuve, H. Haus, and J. Joannopoulos, "Coupling of modes analysis of resonant channel add-drop filters," *IEEE Journal of Quantum Electronics*, vol. 35 No. 9, 1999.

[22] B. Little, S. Chu, H. Haus, J. Foresi, and J.-P. Laine, "Microring resonator channel dropping filters," *Journal of Lightwave Technology*, vol. 15 No. 6, pp. 998–1005, 1997.

[23] V. Ilchenko and A. Matsko, "Optical resonators with whispering-gallery modes-part ii: applications," *IEEE Journal of Selected Topics in Quantum Electronics*, vol. 12 No. 1, pp. 15–32, 2006.

[24] E. Engin, D. Bonneau, C. M. Natarajan, A. S. Clark, M. G. Tanner, R. H. Hadfield, S. N. Dorenbos, V. Zwiller, K. Ohira, N. Suzuki, H. Yoshida, N. Iizuka, M. Ezaki, J. L. O'Brien, and M. G. Thompson, "Photon pair generation in a silicon micro-ring resonator with reverse bias enhancement," *Opt. Express*, vol. 21, 2013.

[25] J. E. Heebner, V. Wong, A. Schweinsberg, R. W. Boyd, and D. J. Jackson, "Optical transmission characteristics of fiber ring resonators," *IEEE Journal of Quantum Electronics*, vol. 40 No. 6, 2004.

[26] C. Kittel, *Introduction to Solid State Physics*. John Wiley & Sons, 8th ed., 2004.

[27] L. Lu, J. Joannopoulos, and M. Soljačić, "Topological photonics," *Nature Photon*, vol. 8, pp. 821–829, 2014.

[28] L. Yuan, Q. Lin, M. Xiao, and S. Fan, "Synthetic dimensions in photonics," *Optica*, vol. 5, pp. 1396–1405, 2018.

[29] L. Yuan and S. Fan, "Bloch oscillation and unidirectional translation of frequency in a dynamically modulated ring resonator," *Optica*, vol. 3, pp. 1014–1018, 2016.

[30] G. Li, L. Wang, R. Ye, Y. Zheng, D.-W. Wang, X.-J. Liu, A. Dutt, L. Yuan, and X. Chen, "Direct extraction of topological zak phase with the synthetic dimension," *Light Sci Appl*, vol. 12, 2023.